Production of $W^{\pm}$ bosons in the semi-muonic channel at forward rapidity in ALICE

Author: Kgotlaesele Johnson Senosi

A thesis in partial fulfillment of the requirements for the degree of Master of Science in the Department of Physics, University of Cape Town.

Supervisor: Prof. J. Cleymans
University of Cape Town
Private Bag X3
Rondebosch 7701
South Africa

Co-supervisor: Dr Z. Buthelezi
Department of Nuclear Physics
iThemba LABS
P.O.Box 722
Somerset West 7129
South Africa

June, 2013

Declaration

I, Kgotlaesele Johnson Senosi know the meaning of Plagiarism declare that all of the work in the document, save for that which is properly acknowledged, is my own.

Signature:
Date: November 12, 2013

Supervisor: Em. Prof. J Cleymans
Co-Supervisor: Dr. E.Z Buthelezi

Contents

List of Figures

List of Tables

Abstract

Heavy-ion collisions are the unique tool available to investigate strongly interacting matter at high energy density where the formation of a new phase of matter −the quark gluon plasma is expected. The ALICE Muon Spectrometer is specifically designed to study this phase of matter using muonic decay channels in the acceptance region between $-4.0 \leq \eta \leq -2.5$ (forward rapidity). ALICE has the unique ability to track and identify particle in a wide rapidity range where in the central barrel ($\mid \eta \mid < 0.9$) the particles are tracked and identified from a transverse momentum (P_T) as low as P_T ∼100 MeV/c up to P_T ∼100 GeV/c with the P_T resolution of about 1% at 50 GeV/c and the impact parameter resolution of about 65 microns at 1 GeV/c. The Forward Muon Spectrometer is composed of 10 tracking chambers, 4 trigger chambers, absorbers as well as the 3 Tm dipole magnet. The P_T resolution of the Spectrometer is ∼1% at 20 GeV/c and ∼4% at 100 GeV/c and the muons are tracked from P_T as low as ∼500 MeV/c up to 100 GeV/c. This study focuses on the analysis of $W^{\pm} \rightarrow \mu^{\pm} + \nu_{\mu^+}(\bar{\nu}_{\mu^-})$ Monte-Carlo data generated using PYTHIA 6.4.21 in the AliROOT framework in proton-proton collisions at 8 TeV and proton-proton experimental data at 7 TeV at forward rapidity. In the analysis of the experimental data the efficiency of the Tracking Chambers is 81±0.5% and 95±0.5% for the Muon Trigger Chambers, while in the simulation the efficiency of the Muon Tracker is ∼80% for the realistic case based on the conditions of 2011 PbPb data taking period and between 95-100% for the ideal case. This study exploits this tracking attributes of ALICE to investigates the feasibility of extracting $W^{\pm}$ boson in its muonic decay channel at these energies.

Acknowledgements

I'd like to thank Zinhle Buthelezi for the patience and tireless input, unwavering encouragement and supervision, Jean Cleymans for agreeing to co-supervise me and for the comments and suggestion in this work, and Diego Stocco for the ever so prompt response regarding the analysis. Also many thanks to the MUON group at Ecole des Mines, SubaTech for the introduction to the ALICE physics and single muon analysis, the ALICE muon spectrometer experts for shift training and to the National Research Foundation and World Federation of Scientists for financial support. Gratitude goes out to the South Africa CERN group for supporting the trips. All thanks to the iThemba LABS ALICE group namely Zinhle Buthelezi, Deon Steyn and Siegfried Förtsch for the company during my zombie state after night shifts. To Pieter Du Toit and Francesco Bossú for the discussion during the hard times of writing. Thanks to the Director of iThemba LABS, Zeblon Vilakazi for taking my interest in particle physics to mind while I was looking to do my masters and sending a lot of e-mail.

It will be a huge mistake to forget my friend, god-father and former teacher Mogomotsi Joseph Molefi, if it was not for your encouragement I wouldn't be here. Also to my friends namely Kealeboga Khuduga, Keorapetse Kwalate, Willie Motsamai and Thabo Senna to name a few, ke a leboga bo-rra for the fun after a long year. And to my father and mother for understanding my choice of a tool of trade, and my siblings for the constant "when are you coming home?".

A humble apology to those I may have forgotten.

List of abbreviations

A-A	nucleus-nucleus
AuAu	nucleus-nucleus
ADCs	Analogue to Digital Converters
ALICE	A Large Ion Collider Experiment
AliEN	ALICE ENvironment
AliROOT	ALICE ROOT
AOD	Analysis Object Data
API	Application Programming Interface
Apt	All Transverse Momentum
ATLAS	A Toroidal LHC Apparatus
CMS	Compact Muon Spectrometer
CMUSH7-B-NOPF-MUON	Class of High-momentum Single MUons with Beams on both sides and NO Past Future protection
CPC	Cathode Plate Chambers
CROCUS	Cluster ReadOut Concentrator Unit System
CTEQ	The Coordinated Theoretical-Experimental Project on QCD
CTP	Central Trigger Processor
DCA	Distance of Closest Approach
DAQ	Data AcQuisition System
DATE	Data Acquisition and Test Environment
DCS	Detector Control System
ECR	Electron Cyclotron Resonator
ECS	Experiment Control System
ESD	Event Summary Data
FEEs	Front-end Electronics
FERO	Frontend Electronics and ReadOut
FSM	Final State Machine
HLT	High-Level Trigger
Hpt	High Transverse Momentum
HVPS	High Voltage Power Supplies
IP	Interaction Point
JDL	Job Description Language
L0	Level Zero trigger
L1	Level One trigger
L2	Level Two trigger
L3	Solenoid Magnet
LHC	Large Hadron Collider
LEIR	Low Energy Ion Ring
LHCb	A Large Hadron Collider Beauty Experiment

LO	Leading Order
LQCD	Lattice Quantum Chromodynamics
LVPS	Low Voltage Power Supplies
MANAS	Multiplexed ANAlogic Signal
MANU	MAnas NUmÃľrique
MB	Minimum Bias
MOOD	Monitoring Of Online Data
OCDB	Offline Conditions Database
PbPb	lead-lead
PDF	Parton Distribution Functions
PDG	Particle Data Group
pp	proton-proton
pQCD	Perturbative Quantum Chromodynamics
PSB	Proton Synchrotron Booster
PS	Proton Synchrotron
QA	Quality Assurance
QCD	Quantum Chromodynamics
QGP	Quark Gluon Plasma
RCT	Run Condition Table
RHIC	Relativistic Heavy Ion Collider
RPCs	Resistive Plate Chambers
SPD	Silicon Pixelated Detector
SPS	Super Proton Synchroton
SU(2)	Special Unitary group
U(1)	Unitary group
UA1	Underground Area 1
UA2	Underground Area 2
V-A	Vector and Axial-vector

Chapter 1

Introduction

1.1 Introduction

The charged mediators of weak interactions, also known as the electroweak bosons W^+ and W^- were first postulated in 1963. They were then discovered in 1983 at the CERN[1] Super Proton Synchrotron (SPS) lead by Simon van der Meer with the UA1 [Ast78] experiment [Pan84] which was led by Carlo Rubbia using the reaction below

$$p + \bar{p} \rightarrow W^+ + X^-, \qquad p + \bar{p} \rightarrow W^- + X^+ \tag{1.1}$$

where $X^{\pm}$ are hadronic states allowed by conservation laws. The proton and anti-proton were collided at the center of mass energy 540 GeV where two experiments UA1 [Ast78] and UA2 [Ban78] were mounted at the interaction points. The measurement of these particles in their leptonic decay channel was affected by the hadronic decays thus requiring considerable care in the treatment of the signal. This discovery led to Carlo Rubbia and Simon van der Meer sharing the 1984 Nobel Prize. The mass of the two charged massive electroweak bosons were measured to be

$$M_W = 80.6\,\mathrm{GeV/c^2} \tag{1.2}$$

in agreement with the Standard Model[2] prediction, with a life time of about $3\times10^{-25}s$, colorless, an electric charge ±1 and spin 1. These vector bosons are best known for beta decay which is a reaction (1.3) where the quark flavour is changed as shown in Figure 1.1.

$$n \rightarrow p + e^- + \bar{\nu_e} \tag{1.3}$$

An example of a leading order formation (LO) of $W^{\pm}$ is shown below 1.1 in which a quark and an anti-quark

$$q + \bar{q^{'}} \rightarrow W^{\pm} \tag{1.4}$$

annihilate, this a dominant process of $W^{\pm}$ production. Higher order processes of $W^{\pm}$ formation involve a quark and a photon or a gluon as initial or final state radiation, an example of such processes is a second order process shown below,

$$q + g \rightarrow W^{\pm} + q^{'} \qquad q + \bar{q^{'}} \rightarrow W^{\pm} + g. \tag{1.5}$$

[1]CERN is the European Organization for Nuclear Research.

[2]Standard Model is theory which describes particles and their interactions, it postulate the existence of six quarks and corresponding anti-quarks, six leptons and five field carriers.

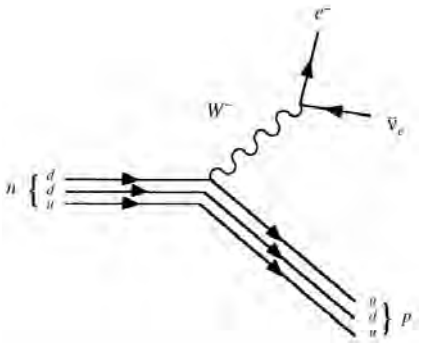

Figure 1.1: Representation of beta decay (weak interaction).

As previously outlined the dominant decay channel of $W^{\pm}$ lead to hadron jets, but these particles were measured in their leptonic decays

$$W^+ \to \ell^+ + \nu_l, \qquad W^- \to \ell^- + \bar{\nu}_l \tag{1.6}$$

where $\ell = \mu, e$ or τ. The different decay channels of $W^{\pm}$ are shown in the Table 1.1 below, where the dominant decay channel is hadronic with a branching ratio 67.60±0.27% [Ber12].

W^+ DECAY MODES

W^- modes are charge conjugates of the modes below.

Mode	Fraction (Γ_i/Γ)	Confidence level	p (MeV/c)
$\ell^+\nu$	$10.8 \pm 0.09\%$		-
$e^+\nu$	$10.75 \pm 0.13\%$		40192
$\mu^+\nu$	$10.57 \pm 0.15\%$		40192
$\tau^+\nu$	$11.25 \pm 0.20\%$		40173
hadrons	$67.60 \pm 0.27\%$		-
$\pi^+\gamma$	$< 8 \times 10^{-5}$	95%	40192
$D_s^+\gamma$	$< 1.3 \times 10^{-3}$	95%	40168
cX	$(33.4 \pm 2.6)\%$		-
$c\bar{s}$	$(31\ ^{+13}_{-11})\%$		-
invisible	$(1.4 \pm 2.9)\%$		-

Table 1.1: The different decay channels of $W^{\pm}$ [Ber12]. Invisible mode represents the width for the decay of the W boson into a charged particle with momentum below detectability, p < 200 MeV/c.

The formation time of $W^{\pm}$ is inversely proportional to its mass

$$t_f(q\bar{q} \to W^{\pm}) \sim \frac{1}{M_W} \sim 0.001\ fm/c \tag{1.7}$$

and its decay time is inversely proportional to its width,

$$t_d(W^{\pm} \to X) \sim \frac{1}{2.141\,\mathrm{GeV}} = 0.09\ fm/c. \tag{1.8}$$

Table 1.1 shows also the $W^{\pm}$ direct decay process to muons, $W^{\pm} \rightarrow \mu^{\pm} + \nu$ or $\bar{\nu}$ with branching ratio $10.57 \pm 0.15\%$ [Ber12] and the indirect processes $W^{\pm} \rightarrow cX/c\bar{s}/hadrons$. According to the law of conservation of momentum the $\mu^{\pm}$ and $\nu_{\mu^+}/\bar{\nu}_{\mu^-}$ from the direct decay of $W^{\pm}$ should each carry the transverse momentum P_T[3] half the mass of $W^{\pm}$ (M_W), thus the muonic decay channel of M_W will populate the $P_T = \frac{M_W}{2} \sim 40$ GeV/c of the single muon spectrum. It is this property which makes it possible to study $W^{\pm}$.

Hard probes like $W^{\pm}$ bosons, heavy flavour (charm and beauty quarks) and quarkonia (heavy quark bound states e.g. J/ψ and Υ) are massive particles thus they are formed during hard collisions of partons when the energy is high enough as it is at the Large Hadron Collider (LHC) [Bry08]. As seen in Figure 1.2 due to energy limitations electroweak bosons were not accessible at Relativistic Heavy Ion Collider (RHIC) whereas heavy flavours in their leptonic decay channel were seen but at lower rates.

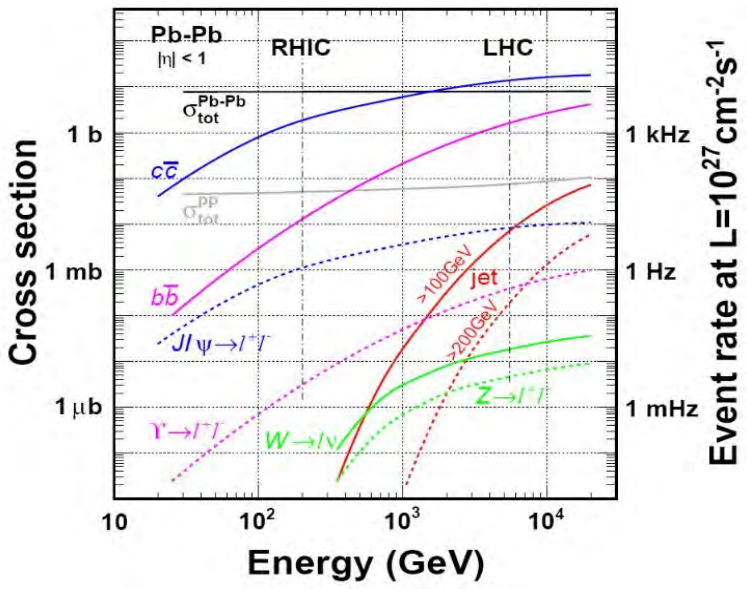

Figure 1.2: Cross section of different probes versus energy and event rate from RHIC to LHC [Car04].

The Large Hadron Collider (LHC) has four main experiments, namely A Toroidal LHC Apparatus (ATLAS) [Atl94], Compact Muon Spectrometer (CMS) [Cms94], A Large Hadron Collider Beauty Experiment (LHCb) [Lhc98] and A Large Ion Collider Experiment (ALICE) [Ali95]. ATLAS and CMS are dedicated to search for Higgs, extra-dimensions and supersymmetry while LHCb is dedicated to studying Charge and Parity violation. ALICE (described in Chapter 3) is dedicated to studying the strongly interacting matter described by Quantum Chromodynamics[4] (QCD) at extremely high energy density, where the formation of a new phase of matter –Quark Gluon Plasma (QGP) is expected to form. This transition of the hadronic matter to the a mixture of quarks and gluons (also called colored medium or strongly interacting medium) is expected to occur at temperature $T_c \sim 170$ MeV [Kar00] as predicted by Lattice

[3] $P_T = \sqrt{p_x^2 + p_y^2}$, where p_x and p_y are the component of momentum in the x-direction and y-direction respectively.

[4] Quantum Chromodynamics is the theory of strong interactions describing the interaction between quarks which are mediated by a self coupling particle (gluon) carrying a color charge.

Quantum Chromodynamics (lQCD) calculations. Ultra-relativistic heavy ion collisions are used as tools to facilitate this phase transition. The QCD phase diagram is shown in Figure 1.3 depicting the predicted crossover temperature.

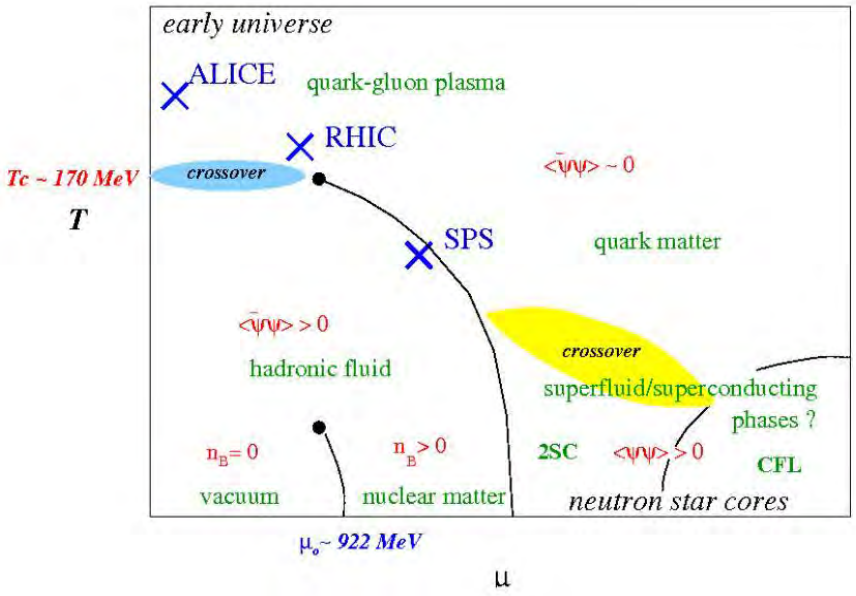

Figure 1.3: QCD phase diagram, where T is the temperature and μ is the baryochemical potential [Han01].

The QGP formation time after initial collisions is expected to be of the order of $\tau_{QGP} \sim 1$ fm/c and to last for about 10 fm/c for lead-lead collisions at the Large Hadron Collider with the center of mass energy 2.76 TeV. Comparing t_f and t_d to τ_{QGP} it is evident that $W^{\pm}$ bosons are formed and also decay before the system thermalizes into QGP thus its decay products will traverse the medium. In the leptonic decay channel of $W^{\pm}$ the decay products are expected not to be sensitive to the colored medium. The properties of this new phase of matter is inferred from the effects it has on the probes used to study it, for example the hard probes (heavy flavours). Since heavy quarks are abundantly produced at the LHC [Abe12b] as seen in Figure 1.2 they are being used to study and probe the QCD medium on other hand particles which are not affected by the medium are used as calibration or reference probes. This is where the production of $W^{\pm}$ come into play. When heavy quarks[5] traverse the medium they interact with it and thus loose energy. The importance of $W^{\pm}$ is to provide a medium blind reference for those probes which are affected by the medium. The energy loss of heavy quarks due to interaction with the medium might lead to suppression in the yield of their bound states [Abe12b]. The medium induced effects for energy loss are quantified by the nuclear modification[6] factor R_{AA} defined by

$$R_{AA} = \frac{1}{< N_{coll} >} \times \frac{(dN/dP_T)^{PbPb}}{(dN/dP_T)^{pp}}, \tag{1.9}$$

N_{coll} is the number of collisions in Pb-Pb, $(dN/dP_T)^{PbPb}$ is the yield in lead-lead and $(dN/dP_T)^{pp}$ is the yield in proton-proton collisions, which should be unity if there are no medium or initial state effects.

[5]Heavy quarks are massive quarks (heavy flavours) produced in initial hard collisions.

[6]Nuclear modification factor is the lead-lead or proton-lead to proton-proton yield ratio scaled by the average number of binary collisions (interacting nucleons) in lead-lead collisions.

In case of $W^{\pm}$ which is colorless the nuclear modification factor is close to unity in the region of P_T >30 GeV/c where it is dominant as seen in Figure 1.4 obtained from the Performance study [dVa07] based on the fast simulation(no reconstruction of tracks through the detector, just kinematics) with PYTHIA[7] [Sjo06] where the region of high $P_T > 30$ GeV/c is populated by muons from $W^{\pm}$.

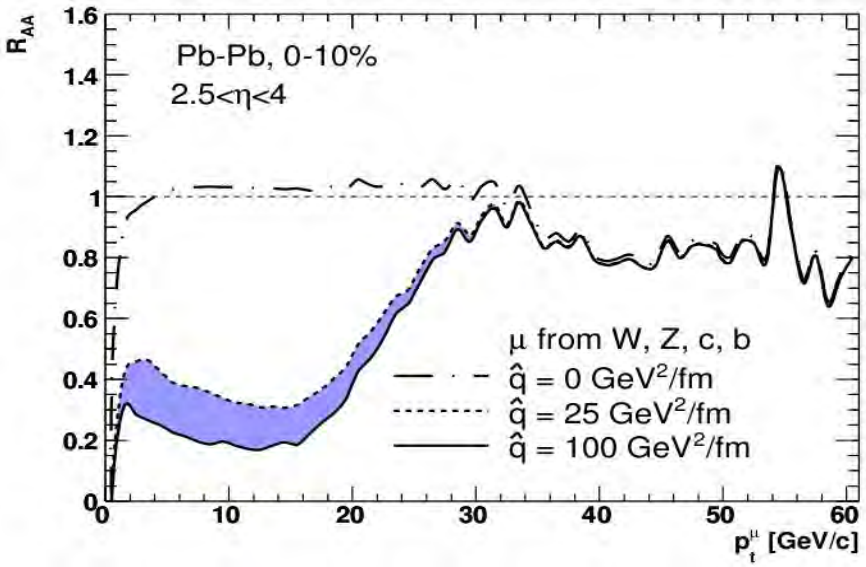

Figure 1.4: Single muon nuclear modification factor in lead-lead collisions from the Performance study [dVa07]. $\hat{q}$ is the energy loss due to binary collisions.

It is thus important to measure $W^{\pm}$ in proton-proton collisions in order to extract $W^{\pm}$ nuclear modification factor in lead-lead collisions and also in proton-lead collisions in order to investigate different nuclear matter effects (nuclear matter effects will be discussed in Chapter 2).

1.1.1 Physics motivation

Beside being used as a baseline for lead-lead and proton-lead collisions the measurement of $W^{\pm}$ in proton-proton collisions at LHC energies will provide relevant information discussed below:

- In proton-proton collisions, it will be sensitive to the quark Parton Distribution Functions[8] (PDFs) at high $Q^2(Q \sim M_{W/Z})$, Figure 1.5 shows the PDFs plotted against Bjorken-x, where x is the fraction of a beam particle momentum carried by a parton involved in hard scattering, it is given by $x_{i,j} = \frac{M_W}{\sqrt{s_{NN}}} e^{\pm y}$, where $\sqrt{s_{NN}}$ is the center of mass energy, $x_{i,j}$ is the x of two partons annihilating to form a particle of mass M_W (a W^+ or W^- boson) and y is the rapidity which will be discussed is Chapter 2. It is seen in Figure 1.5 that above $x \sim 0.8$ the valence quark PDF dominate.

- luminosity (number of particle collisions per second per unit cross-section) measurements since the $W^{\pm}$ cross section is well known, and to improve the evalu-

[7]PYTHIA is a Monte Carlo event generator discussed in detail in Chapter 4.

[8]Parton Distribution Functions describes the behavior of a parton inside a nucleon, they're dependent on the energy scaling variable Q and Bjorken-x.

ation of the detector performances [Tri05a]. Since high momentum muons from $W^{\pm}$ will pass through the chambers quicker, they will thus leave a weak signal hence a good detector response and tracking efficiency as well as large statistics is required for high momentum measurements. This why $W^{\pm}$ is used for detector performance testing.

- binary scaling cross-checks, where the yield in lead-lead is scaled by the number of inelastic collisions in proton-proton as seen below

$$\frac{dN^{W}_{PbPb}}{dP_T} =< N_{coll} > \times \frac{dN^{W}_{pp}}{dP_T} \tag{1.10}$$

where $\frac{dN^{W}_{PbPb}}{dP_T}$ is the yield in lead-lead collisions, $< N_{coll} >$ is the number of nucleon-nucleon binary collisions in lead-lead which is dependent on centrality of collision and $\frac{dN^{W}_{pp}}{dP_T}$ is the yield in proton-proton collisions. Centrality is the measure of whether the collision of ions is peripheral (few participating nucleons in the collision) or most central (more participating nucleons in the collision).

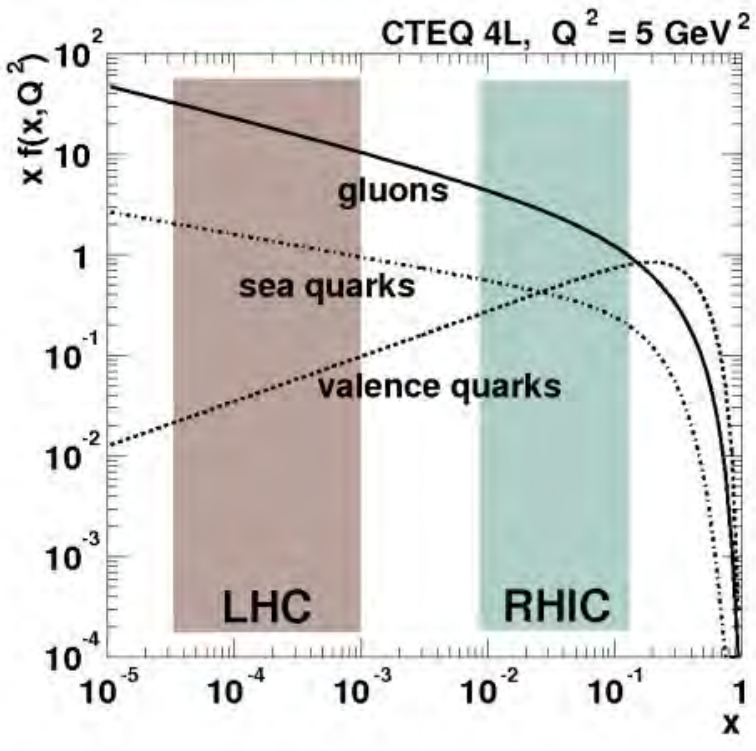

Figure 1.5: Accessible Bjorken-x range for heavy flavours and $W^{\pm}$ in Pb-Pb collisions at 5.5 TeV (left) and in pp collisions at 14 TeV (right) [Dai03].

1.2 Aim of the study

The ALICE detector (see Chapter 3) has the excellent capabilities to track and identify particles down to a transverse momentum close to zero ∼100 MeV/c and up to

$P_T \sim 100$ GeV/c. The central barrel and the muon spectrometer cover the pseudorapidity[9] region $\mid \eta \mid < 0.9$ and $-4.0 < \eta < -2.5$ respectively. The muon spectrometer also has the ability to resolve the low P_T and high P_T muons with a resolution of 1% and 4% respectively. In this thesis we exploit these capabilities with the interest of extracting $W^{\pm}$ bosons in its muonic decay channel using the ALICE muon spectrometer. The study is based on a pure signal of the $W^{\pm}$ bosons data produced with a Monte Carlo generator PYTHIA in p-p collisions at $\sqrt{s_{NN}} = 8$ TeV prompted by available experimental data of p-p at $\sqrt{s_{NN}} = 7$ TeV hinting at the possibility to measure $W^{\pm}$ bosons at this energy. This study investigate the feasibility of measuring $W^{\pm}$ bosons in the forward rapidity to be used as a reference for ongoing studies in heavy flavours production while at the same time it can be used to test the detector performance. Since the alignment of the detector plays an important role in single muon studies the simulations aim at investigating how the detector working conditions used in reconstruction can affect the single muon momentum distribution [DuT13]. The simulations aim also at predicting how much $W^{\pm}$ will be produced in proton-proton collisions at 8 TeV in 2012. Since the data was not available for muon analysis during this study it is not included in this work.

1.3 Thesis outline

Chapter 2 of this thesis gives an overview of the theoretical background and literature review. Chapter 3 describes the experimental setup with more focus on the ALICE Muon Spectrometer, Chapter 4 present the experimental results and Chapter 5 describes the simulation carried out. Chapter 6 present the conclusion and remarks.

[9] Acceptance variable η which is related to the polar angle by the equation $\eta = \frac{1}{2}\ln(\tan\frac{\theta}{2})$

Chapter 2

Theoretical Background

2.1 Standard Model and QCD

Standard Model

The standard model describes matter according to its elementary constituents namely, the quarks and gluons. The fermions are categorized in three families of leptons and quarks and their anti- particles. Their interactions are mediated by different force carriers, namely the photon (γ) for electromagnetic interactions, $W^{\pm}$ and Z^0 for weak interactions and the gluon (g) for strong interactions (see Figure 2.1). The strong interactions is described by the theory of QCD and weak interactions by the electroweak theory.

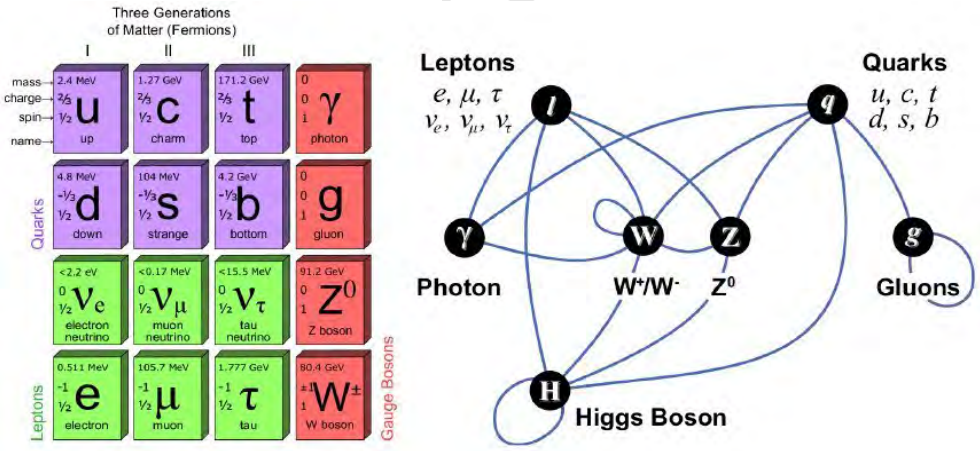

Figure 2.1: Elementary particles of the standard model (left) and the force carriers (right) [Zha12].

Quantum Chromodynamics

Quantum Chromodynamics (QCD) is a theory of strong interactions, responsible for binding protons and neutrons within the nucleus of radius of one fermi [Han01]. QCD treats nucleons as composite states not as fundamental particles. This is a picture of the parton model [Gre08] developed by Bjorken and Feynman which treats hadrons as a collection of quasi free particles. The model describes the cross section for high-energy scattering of hadrons with another particle as an incoherent sum of the cross

sections of the point–like partons in the hadron with the other particle [Gre08]. The prototype process for the parton model is $eN \rightarrow e'X$ where e and e' are the incident and scattered electron, N is the target nucleon, and X is the set of final state hadrons. The composites of these nucleons are described as quarks, held together by a strong force mediated by color charged field. Due to the nature of the strong interaction with coupling constant $\alpha_s(Q^2) \sim 1$, unlike the photon, the mediator of strong interactions gluons are charged and can couple to each other. As a result, the intensity of the strong interactions diminishes at short distances (high energies), as shown in Figure 2.2. Hence the interactions of quarks cannot be easily described by perturbation theory.

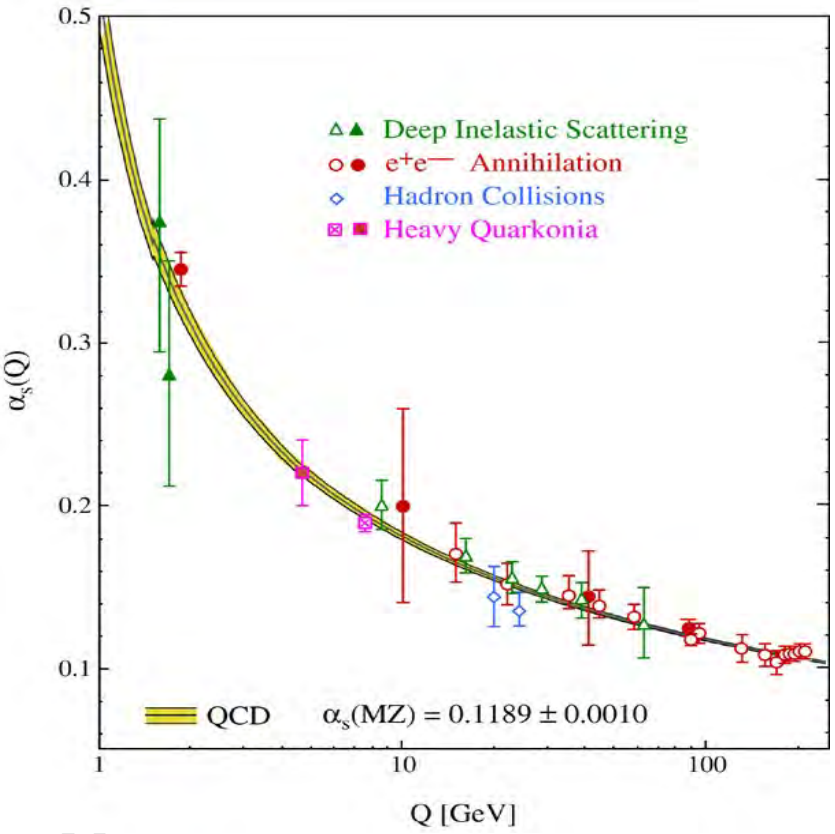

Figure 2.2: QCD coupling constant ($\alpha_s(Q) = \alpha_{QCD}(Q^2)$) as a function scaling variable Q [Bet07]. $\alpha_s(Q = M_Z)$ is shown, where M_Z is the mass of the Z^0 boson.

The strong coupling $\alpha_s(Q)$ in Figure 2.2 is given by the equation below,

$$\alpha_s(Q) = \frac{4\pi}{(11 - \frac{2}{3}n_f)\ln(\frac{Q^2}{\Lambda^2_{QCD}})} \tag{2.1}$$

which was confirmed by experiments, thus leading to David J. Gross, H. David Politzer and Frank Wilczek being awarded the 2004 Nobel Prize in Physics [Gro73]. In the equation Q^2 is the virtuality related to the momentum transfer in a given process, n_f is the number of light flavour quark $m_q << Q$ and Λ_{QCD} is the non-perturbative QCD scale corresponding to an α_s value where pQCD cannot be used.

2.1.1 Confinement

The interaction between quarks is based on their intrinsic color charge, just as that between electrons and protons or nuclei is determined by their electric charge. The form of the interaction is quite different from the Coulomb interaction where the potential can vanish for large separation distance so that electric charges can be separated and have an independent existence. In contrast the potential between quarks increases with separation, so that an infinite energy would be needed to isolate a quark. In other words, the quark constituents of a hadron are confined and not just bound [Mat86]. The interaction potential between two quarks is described by,

$$V(r) = -\frac{A(r)}{r} + kr \qquad k \sim 0.18 \text{ GeV}^2 \tag{2.2}$$

where r is the separation between the quarks, $A(r)$ is the coefficient which has the properties of the strong force coupling constant and k is the string tension which gives the strength of the quark "confinement". For small r the first term dominates, and describes an attractive Coulomb like interaction [Gro73, Mar06]. Studies show that α_s varies with effective quark masses [Raj06], thus it is no longer a constant but rather a slowly varying function with $\frac{1}{\ln(Q^2/m^2)}$, hence $A(r) \sim \frac{1}{\ln(r^{-1})}$ [Raj06, Gro73]. This variation of $A(r)$ implies that the interaction between quarks gets weaker with decreasing separation.

In the limit $r \to 0$ the quarks can be considered as weakly interacting, a property known as asymptotic freedom [Han01]. The potential between two quarks grows linearly with separation distance, described by the second term of the above equation. Hence quarks can be asymptotically freed by compression or heating as shown in Figure 2.3. Relativistic colliders provide a tool to study this phenomenon by colliding heavy ions.

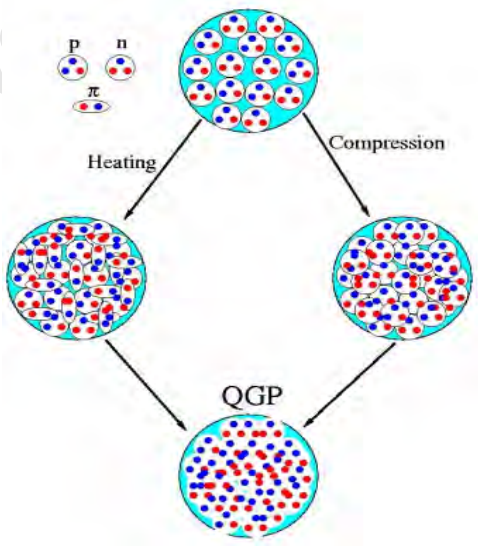

Figure 2.3: Schematic showing QGP formation according to the Bag Model [Cho74].

2.1.2 Formation of the Quark Gluon Plasma (QGP)

Relativistic nucleus-nucleus collisions are a unique tool to investigate the behavior of strongly interacting matter. Ultra–relativistic collisions of nucleons lead to compression and heating due to conversion of beam energy into internal excitation energy and thus thermalization of the deposited energy starts [Sin00]. Hydrodynamical models assume that local thermal equilibrium is maintained throughout the evolution of this state. These interactions produce different particles in different directions. Deep inelastic scattering provided a scope for this interaction. This led to parton model.

In these collisions a new phase of matter is formed when the initial center of mass

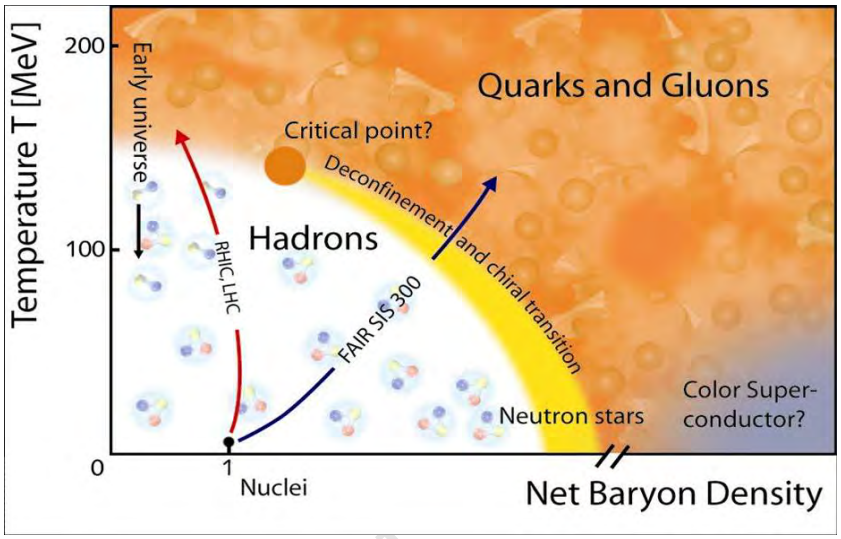

Figure 2.4: QCD phase diagram [Ric09].

energy of the colliding particles becomes sufficient to deposit high enough energy to accumulate the energy density ~ 1 GeV/fm^3 for a long enough time required to form a QCD phase of matter as shown in Figure 2.4. Lattice QCD (lQCD) predicts this cross-over to a new phase of matter at a temperature of ~ 170 MeV (see Figure 2.5) at vanishing or at small chemical potential μ_B [Han01].

Above this temperature lQCD predicts deconfinement of partons from neutral color states bound by a strong force (color confinement) with a coupling constant $\alpha_s(Q^2)$. At high energies the momentum transfer is large and the coupling constant α_s becomes small leading to quarks behaving as quasi-free particles. This is described by the "bag model", which stipulates that at these energies partons move freely yet are confined to the bag or droplet of radius R, which is the order of magnitude of the nucleon. Using the analogy of the bag model [Cho74] QGP can be formed by heating up matter or by compressing the nucleons in small space.

As the strong coupling constant approaches zero the chiral symmetry is restored, meaning that the right- handed and the left-handed quarks do not interact. Restoration of symmetry occurs at large energy where quarks are expected to acquire their QCD Lagrangian mass. It is this restoration of symmetry which suggests a phase transition of strongly interacting matter to QGP. The transition to the QGP is governed by the chiral symmetry QCD Lagrangian which requires the quark masses to vanish but in reality the quark masses at deconfinement do not vanish. So this is the assumed global symmetry. Since for heavy quarks the mass is not small enough to be assumed

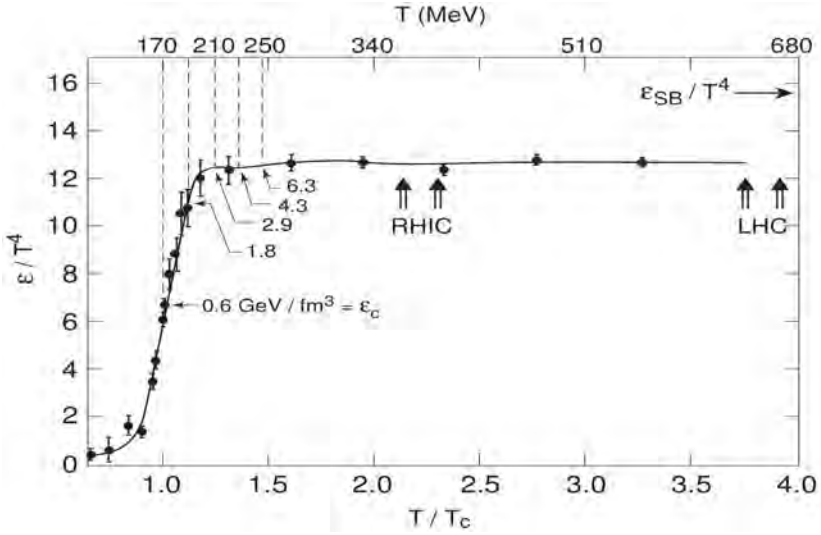

Figure 2.5: Energy density ε/T^4 vs T/T_c for QCD with 3 light quark flavors [Han01, Kar00].

to be zero they do not play a role in the phase transition thus making the 3 flavor QCD interesting [Car04].

2.1.3 Creation and evolution of the QGP

The dynamics of QGP are studied through indirect methods since it is created for a short period of time. This new phase of matter evolves from a sea of quarks and gluons into hadrons and mesons which are then measured in the detector. The observed particles are neutral (photons and neutrons) or charged (muons, electrons, etc). The time needed by partons produced during hard collisions to redistribute their energy through multiple scattering to form the plasma is $\tau_{strong} \sim 1\ fm/c$. This energy is redistributed in the center of mass to thermalize and create high temperature matter. Due to the high temperature, the system undergoes expansion due to radiation pressure; it then tends to cool down towards a hadronic phase. At low enough energy densities the system evolves to a state where particles can be produced, i.e. chemical freeze out. The evolution of this newly formed matter is shown in Figure 2.6. The properties of this QCD phase are studied through the kinematics of the produced particles using different experimental observables.

2.1.4 Observables

There are different observables used to infer the properties of the QGP during its evolution. They can be categorized in the following way:

Global observables provide the general information about the collision e.g.

- centrality – either the collision is head-on or peripheral,
- reaction plane – a plane described by the impact parameter and the beam axis,
- expansion velocity – the rate of expansion of the medium,

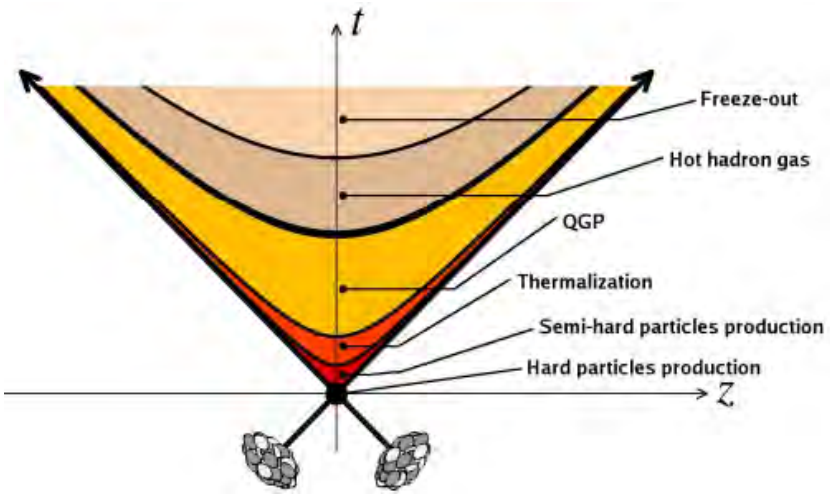

Figure 2.6: Light-cone diagram of a collision [Sto08].

- initial energy density – the minimum energy density attained to form the QGP.

These observables can be determined by measuring particle multiplicity, transverse energy (E_T), and hadron kinematics.

Initial state observables behave as scaling probes for the standard model, since they are not affected by the QGP. These probes which are high transverse momentum (p_T) photon and electroweak bosons are expected to behave the same in different collisions. They are formed after initial collisions when the energy is high enough and they do not interact strongly.

Final State observables provide information about the different phases: hadronic and QGP. These are for example:

- Azimuthal anisotropic flow – describes the collective movement of the QGP particles,
- hadron yield– number of particle produced,
- and transverse momentum distribution (p_T) of hadrons – yield of hadrons against transverse momentum

which are obtained from hadron yields and kinematic properties.

Heavy quarks and their bound states. Heavy quarks are partons created in the early stages of collisions mainly through gluon fusion ($gg \rightarrow Q\bar{Q}$) which is a dominant process at the LHC energies. Since they are created in the early stages of collisions they thus carry large energy and will loose their energy through traversing QGP via interactions with soft partons. Due to their large masses their production in hard process can be treated in the perturbative QCD framework. Their energy loss is theoretically treated in two frameworks namely, perturbative QCD (pQCD) which assumes a small strong coupling constant and the other which takes into account large strong coupling constant AdS/CFT [Mal98]. The sensitivity of hard probes to the QCD medium makes them a good tool for QGP tomography.

	SPS	RHIC	LHC
N($c\bar{c}$)	0.2	10	130
N($b\bar{b}$)	-	0.05	5

Table 2.1: Number of $c\bar{c}$ and $b\bar{b}$ produced in central heavy ion collisions at SPS (PbPb), RHIC (AuAu) and LHC (PbPb) energies [Cro05].

The properties of this new phase of matter are inferred by the effects it has on several probes. Heavy quarks (bottom and charm) and their bound states are expected to be abundantly produced at the LHC compared to SPS and RHIC as shown in Table 2.1 [Abe12b, Cro05], since they have large cross-sections at these energies they have been suggested as probes for QGP. Due to their large masses heavy quarks are expected to be produced in the initial collisions during hard scattering therefore they are used as probes of nuclear Parton Distribution Functions as well as nuclear matter effects in proton-lead collisions and in lead-lead collisions where they are expected to interact with the medium formed. Figure 1.5 shows the CTEQ4L PDFs with the corresponding variation with Bjorken-x, at fixed $Q^2 = 5\,\mathrm{GeV}^2$ which correspond to charm and anti-charm ($c\bar{c}$) pair production. The medium induced effects can be studied by comparing the production of heavy flavour in nucleus-nucleus and proton-proton collisions. And this is one of the reasons ALICE is undertaking a proton-proton program to understand and interpret heavy-ion data. In proton-proton collisions heavy quarks are produced via hard scattering at virtual energy transfer $Q = 2M_q$ (M_q is the mass of a heavy quark). In the absence of nuclear effects the hard processes are expected to scale as binary collisions, that is the nucleus-nucleus collisions can be treated as a superposition of independent nucleon-nucleon collisions. Then the heavy quarks differential yields in nucleus-nucleus will be proportional to the number of inelastic collisions in proton-proton collisions, this is

$$\frac{dN_{AA}^{H_Q}}{dP_T} = N_{coll} \times \frac{dN_{pp}^{H_Q}}{dP_T}. \tag{2.3}$$

a. Hot nuclear matter effects

Asymptotic freedom suggest that the running coupling between heavy quarks is small so perturbative QCD can be used to describe their bound states. Since heavy quark bound states are expected to be sensitive to the medium formed in lead-lead collisions they are used as probes for energy loss mechanisms. From QCD the energy loss of gluons is larger than that of heavy quarks which in turn suffer more energy loss than light quarks. This can be quantified by using the nuclear modification factor R_{AA},

$$R_{AA} = \frac{1}{< T_{AA} >} \times \frac{dN_{AA}/dP_T}{d\sigma_{pp}/dP_T} \tag{2.4}$$

where $< T_{AA} >$ is the average nuclear overlap function in a centrality class as defined in the framework of the Glauber model [Gla70], dN_{AA}/dP_T is the transverse momentum yield in nucleus-nucleus collisions and $d\sigma_{pp}/dP_T$ is the transverse momentum inclusive cross-section in proton-proton collisions. In the absence of nuclear modification the R_{AA} of heavy flavour is scaled to be unity. A deviation from unity will be

an evidence of whether there is suppression or enhancement of the yield. The energy loss of heavy quarks due to the medium effects can be due to radiative energy loss, collisional energy loss, thermal scattering and collisional dissociation.

Radiative energy loss is dependent on the mass of a parton (dead cone effect) which suggests different energy loss of light and heavy quarks in the medium due to small angle gluon bremsstrahlung from massive quarks at small angle [Bai01]. **Collisional energy loss** is due to energy transfer in collisions of heavy quarks with the partons in the medium. **Thermal scattering** is based on the Langevin model aimed at describing elastic scattering between heavy quarks and the medium [Moo05]. **Collisional dissociation** this energy loss mechanism focuses on the effect of collisions of heavy quark bound states with the medium which might lead to their dissociation as suggested in [Won05].

b. Cold nuclear matter effects

Heavy flavour production will be sensitive to the gluon PDF, in proton-lead collisions the gluon PDF will be modified due to the high parton density in the nuclei, i.e. PDFs in nuclei are different from the superposition of PDFs of their nucleons. This is quantified by the equation

$$R_i^A = \frac{f_i^A(x,Q^2)}{f_i^N(x,Q^2)}), \tag{2.5}$$

where $f_i^A(x,Q^2)$ and $f_i^N(x,Q^2)$ are the nuclear and nucleon PDF respectively for a parton i and x is the Bjorken-x.

Nuclear modification of the gluon PDF is shown in Figure 2.7. Since the gluon PDF is sensitive to initial conditions the heavy flavour production is expected to be sensitive to the initial cold nuclear matter effects in proton-lead collisions. The decrease in the ratio $R_g^A(x,Q^2)$ is called shadowing which will affect the production of the heavy quark pair at low Bjorken-x [Zha12, Mat10].

In the following section we describe one of the initial stage probes (W^+ and W^-) which are field carriers of weak interactions.

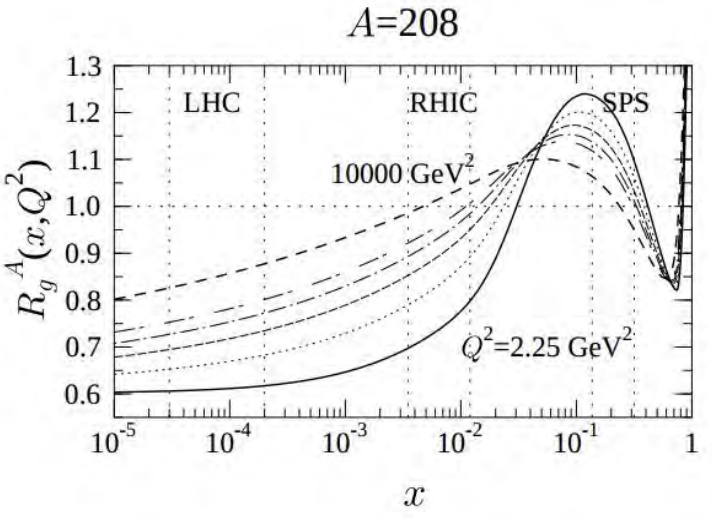

Figure 2.7: R_g^A of gluon vs. x at different scaling factor Q^2 in proton-lead collisions [Esk01].

2.2 Weak Interactions

The weak interactions (formalism is discussed in Appendix I) are not invariant under the parity[1] transformation $-\vec{P}$, they couple left–handed neutrinos and right-handed anti-neutrinos which violates parity. This violation of parity was first suggested by Lee and Yang in 1956 and experimentally [Wu$^+$57] proven by Wu soon after. In her experiment the electrons were emitted in the opposite direction to the Cobalt nuclear spin which was aligned by an external magnetic field. The anti-neutrino is right-handed hence it is emitted in the same direction. The vector and axial-vector (V-A) structure of electroweak theory means that the weak current couples only left-handed u and d quarks (or right-handed u and d). At high energies, this means only negative helicity[2] u and d quarks are coupled, or positive helicity u and d quarks [Hal86]. The weak interaction vertices do not mix the lepton generations but do connect the quark generations. The weak interactions are mediated by electroweak bosons i.e. the photon (γ), $W^{\pm}$ and Z^0. Glashow, Salam, and Weinberg shared the 1979 Nobel Prize in Physics for the unification of electromagnetic and weak interactions. In 1983, $W^{\pm}$ and Z^0 were discovered experimentally [Pan84] according to the masses predicted by the Standard Model. Massive electroweak boson properties are discussed below with a focus on the $W^{\pm}$ bosons.

2.2.1 Electroweak bosons – Initial State Observables

Weak interactions couple quarks and leptons of the same generation. The $W^{\pm}$ boson formation vertex couples a quark and an anti-quark of different family. In the lowest order approximation, $W^{\pm}$ bosons are produced by the quark (q) and anti-quark ($\bar{q}^{'}$) annihilation process (Figure 2.8).

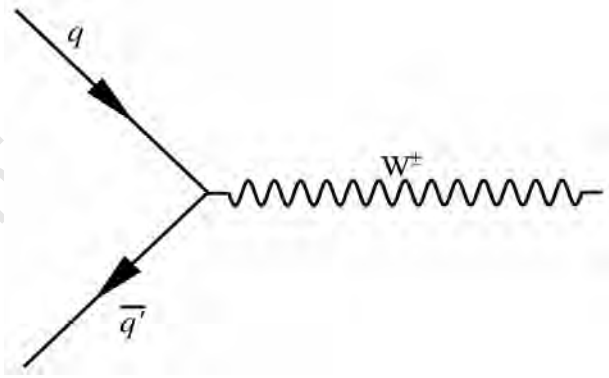

Figure 2.8: $W^{\pm}$ formation vertex at leading order.

At the $W^{\pm}$ vertex the electric charge, lepton number, quark number and quark colour are conserved whereas the quark flavour is not.

Figure 2.9 presents the flavour decomposition of $W^{\pm}$ production cross section at leading order which shows the isospin dependence of the colliding system. Considering

[1]Parity $\hat{P}$ is a symmetry operator of physical quantities or processes under spatial inversion, which has two eigenvalues ± 1.

[2]Helicity $\vec{h}$ is the projection of the spin $\vec{S}$ onto the direction of momentum, $\vec{p}$, $\vec{h} = \frac{\vec{S}.\vec{p}}{|\vec{p}|}$.

the valence quarks, this figure shows that more W^+ will be produced than W^-, from the isospin of a proton $\frac{N_{W^+}}{N_{W^-}} = \frac{N_{u-quark}}{N_{d-quark}}$ which is approximately $N_{W^+} \sim 2N_{W^-}$.

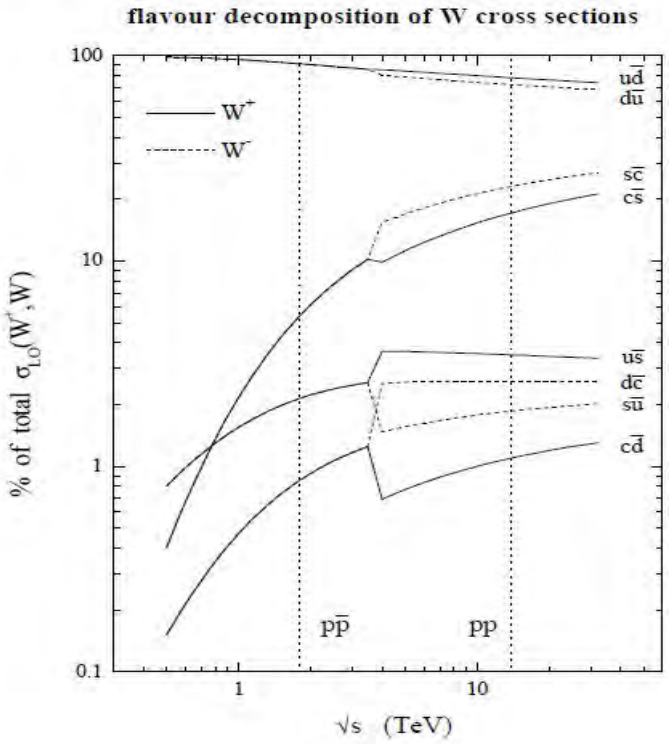

Figure 2.9: Parton decomposition of the W^+ (solid line) and W^- (dashed line) total cross sections in $p\bar{p}$ and pp collisions. Individual contributions are shown as a percentage of the total cross section in each case. In $p\bar{p}$ collisions the decomposition is the same for W^+ and W^- [Mar00].

These sub-processes are characterized by $Q^2 = M^2$ scaling and Bjorken-x which can be determined as [Tri05a]

$$x_{1,2} = \frac{M}{\sqrt{s}} e^{\pm y}, \tag{2.6}$$

where M is the mass of the weak boson, $\sqrt{s}$ is the center-of- mass energy of the nucleon-nucleon collision, and y is the rapidity

$$y = \frac{1}{2} \ln \frac{E + p_l}{E - p_l}, \tag{2.7}$$

where E is the energy and p_l is the longitudinal momentum [Tri05b]. According to Figure 2.10 shown below the LHC will allow for low-x physics according to the scaling above. $W^{\pm}$ will enable scaling around $x = 10^{-4}$ at forward rapidity. Figure 2.11 which explains scaling by Equation 2.6 shows that at forward rapidity $W^{\pm}$ will be formed by a parton with low and higher Bjorken-x, for example at y =3, we have $-y$ and $+y$ corresponding to $x = 5.016 \times 10^{-4}$ and $x = 0.2024$ respectively, these values are for pp collisions at the LHC at 14 TeV as seen in 2.11.

Partons with high Bjorken-x are most likely valence quarks, and the ones with small Bjorken-x are most likely sea quarks. Due to the isospin of a proton (two u quarks and one d quark) there is a high possibility of a u-quark interacting to form W^+ thus at forward rapidity more W^+ are seen than W^-.

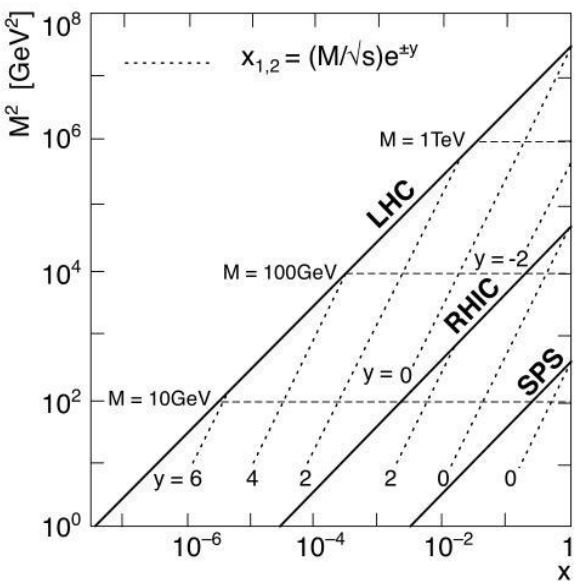

Figure 2.10: LHC parton kinematics [Tri05a] The range of Bjorken-x and M^2 relevant for particle production in A-A collisions at the top SPS, RHIC and LHC energies. Lines of constant rapidity are indicated.

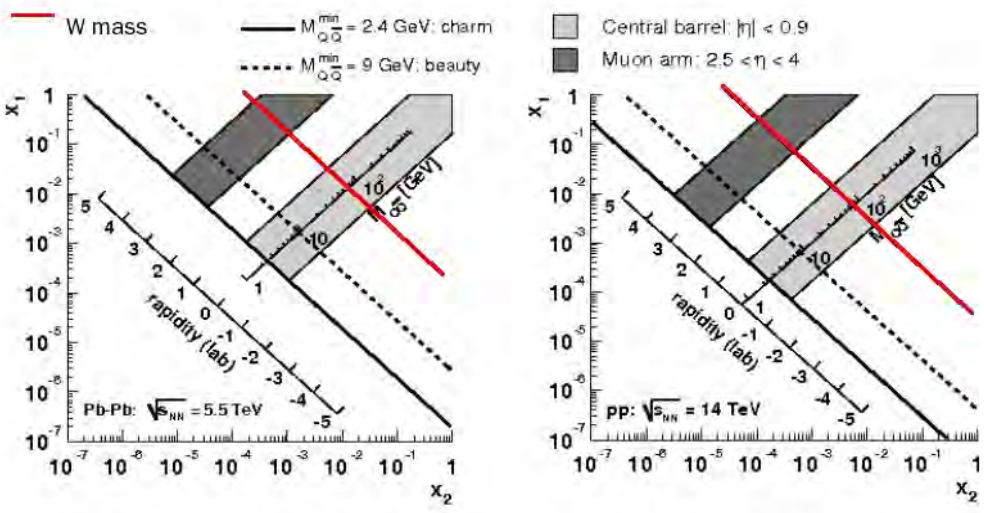

Figure 2.11: Accessible Bjorken-x range for heavy flavours and $W^{\pm}$ in Pb-Pb collisions at 5.5 TeV (left) and in pp collisions at 14 TeV (right) [Dai03]

The decay vertex of W^+ couples a right-handed anti-fermion and left-handed neutrino whereas W^- couples a left-handed fermion and right-handed anti–neutrino. Below is a semi-muonic decay schematic of $W^{\pm}$ in a rest frame. The V-A coupling of W^+ in Figure 2.12 shows that it will be polarized in the direction of the $\bar{d}_R$ whereas W^- will be polarized in the direction of the $\bar{u}_R$. Since the neutrino is left-handed it is emitted in the direction of u_L and the right-handed anti-fermion e_R^+ is emitted in the direction of the $\bar{u}_R$. Considering the PDFs, the valence quark has the high probability to carry larger fraction of the proton momentum than the sea quarks ($\bar{u}_R, \bar{d}_R$, etc.) as seen in Figure 1.5 in Chapter 1. The valence quarks will thus have large Bjorken-x. Then the rapidity of W^+ will be boosted in the direction of the u_L whereas the W^-

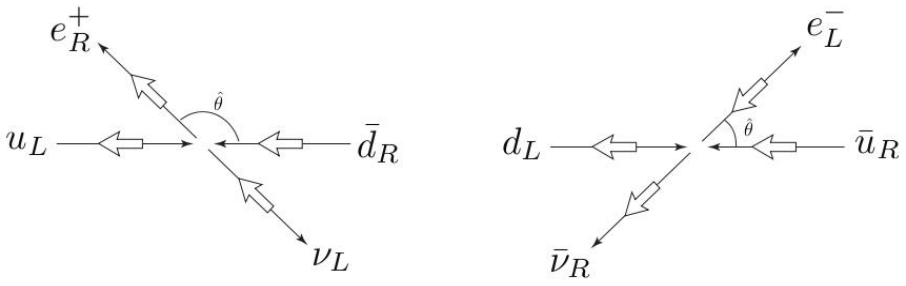

Figure 2.12: The formation (LO) and decay vertex of $W^{\pm}$, where $e^{\pm}_{RL}$ and $\nu_L/\bar{\nu}_R$ (neutrinos) represent the leptons [Oid12].

will be boosted in the d_L. From Figure 2.12 the angular momentum boost the e_R^+ whereas the e_L^- is boosted in the opposite direction.

A muon from W^- is expected to be boosted towards high rapidity whereas the W^+ tend to be produced at lower rapidity. This effect is shown in Figure 2.13 taken from the previous Performance Study [dVa07] which results in the distribution of μ^- shifting towards higher rapidity.

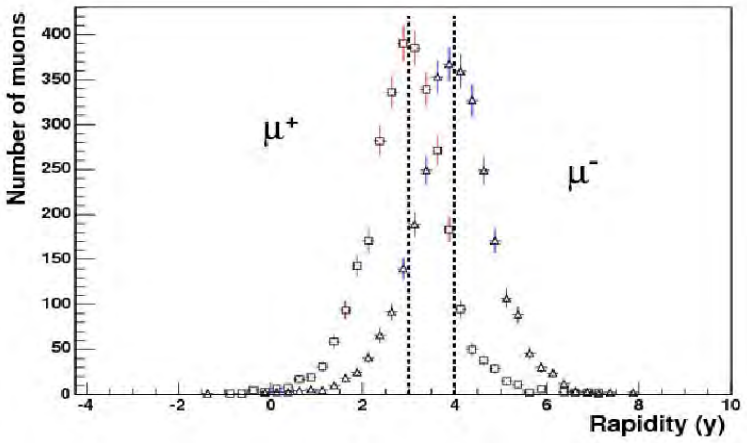

Figure 2.13: Shown in here is the number of entries versus rapidity. This Figure is taken from the performance study [dVa07].

Quark mixing and parity violation

Quark mixing in weak coupling was introduced by Cabibbo to explain weak interaction vertices which were forbidden in theory of weak interactions but seen in experiments, for example the decay $K^- \rightarrow \mu^- + \bar{\nu}_{\mu^-}$ which requires coupling of $s + \bar{u} \rightarrow W^-$. In the framework of quark mixing it thus became possible for quarks of different generation to couple, and thus incorporating vertices which were previously forbidden into the theory. Charge and parity violation could not be explained in the two generation quark mixing done by Cabbibo, observing this, Kobayashi and Maskawa generalized the Cabbibo matrix into the Cabibbo—Kobayashi—Maskawa matrix (or CKM matrix) which took into account the third generation [Hal86]. According to quark mixing the d, s and b participate in weak interactions through Cabbibo rotated states, so $W^{\pm}$ couples to $ud^{'}$ where $d^{'}$ is the Cabbibo rotated state,

$$d' = d\cos\theta_c + s\sin\theta_c \tag{2.8}$$

and θ_c is the Cabbibo angle which is related to the probability that quark of certain flavour decays to another flavour.

Chapter 3

Experimental Setup

3.1 The Large Hadron Collider

As mentioned in Chapter one the Large Hadron Collider (LHC) is a particle accelerator situated underground in a 27 km circumference tunnel at the CERN laboratories. The LHC shown in Figure 3.1 accelerate protons and heavy ions, lead (Pb) to relativistic energies and collide them at different experimental points, namely: ATLAS [Atl94], ALICE [Ali95], CMS [Cms94] and LHCb [Lhc98]. The particles are first pre–accelerated in a series of accelerators before being injected into the LHC where they are accelerated to nominal energies. The projected maximum energy for proton–proton collisions is $\sqrt{s_{NN}} = 14$ TeV and for lead–lead is $\sqrt{s_{NN}} = 5.5$ TeV.

The proton beam is initially produced in Linac 2 where the electron is stripped off a hydrogen atom, and then injected into the Proton Synchrotron Booster where it is boosted to an energy of 1.4 GeV before it is transferred to the Proton Synchrotron (PS) for further acceleration to 25 GeV in energy. The beams are then injected into the Super Proton Synchrotron (SPS) where they are accelerated to an energy of 450 GeV before being injected into the Large Hadron Collider, where at present are accelerated to the maximum energy of 4 TeV each before colliding at the above-mentioned interaction points of the LHC.

Each lead ion beam (Pb) is produced in the Electron Cyclotron Resonator (ECR) using heat, magnetic field and microwaves. Here the Pb^{+27} is produced by the ECR before being injected into Linac 3 where it is accelerated to the energy of 4.2 MeV before being passed through a carbon foil to strip of twenty-seven electrons thereby producing Pb^{+54}. The Pb^{+54} beam is then accelerated to an energy of 72 MeV/nucleon in the Low Energy Ion Ring (LEIR) before being sent to the PS, which accelerates it to 5.9 GeV/nucleon, passes it through a second foil (which fully strips it to Pb^{+82}) and transfers it to the SPS. Finally, the SPS accelerates the lead ions (Pb^{+82}) to an energy of 177 GeV/nucleon and injects them into the LHC, where they are currently being accelerated to 1.38 TeV/nucleon in energy. In the LHC particles are accelerated in vacuum tubes and kept in circular orbits with dipole magnets until the energy and luminosity of interest is attained then the particles are allowed to collide at different collision points shown in Figure 3.2. This report will focus on the study using the ALICE detector with emphasis on the Forward Muon Spectrometer discussed in details in the next sections.

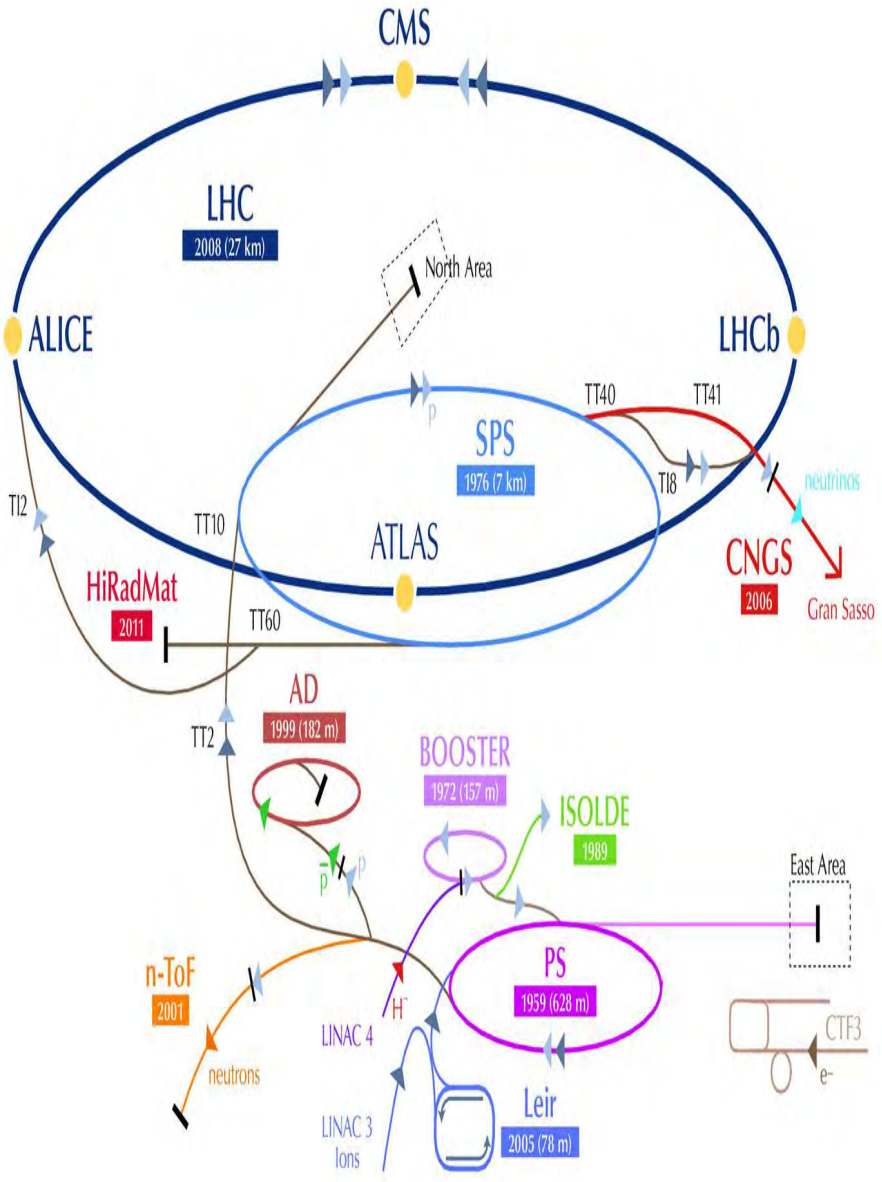

Figure 3.1: The Large Hadron Collider Accelerator Complex [Lpcb].

3.2 The ALICE Detector

The ALICE detector shown in Figure 3.3 is designed to study heavy ion collisions, with the main purpose of studying the physics of strongly interacting matter at extreme energy densities. The detector is optimized to handle particle multiplicity of $(\frac{dN}{d\eta})_{ch} = 4000$ (where N is the number of particles and η is the pseudorapidity or measure of polar angle) expected in lead-lead collisions. ALICE has an excellent tracking and particle identification performance of up to $(\frac{dN}{d\eta})_{ch} = 8000$.

The ALICE detector consists of 18 dedicated sub-detectors located in the central and forward region. The central barrel comprises of detectors to measure event by event hadrons (mainly pions and kaons), electrons and photons, while the Forward Muon Spectrometer focuses on muon detection. These series of detectors make it possible to perform tracking and particle identification in a wide transverse momentum (p_T)

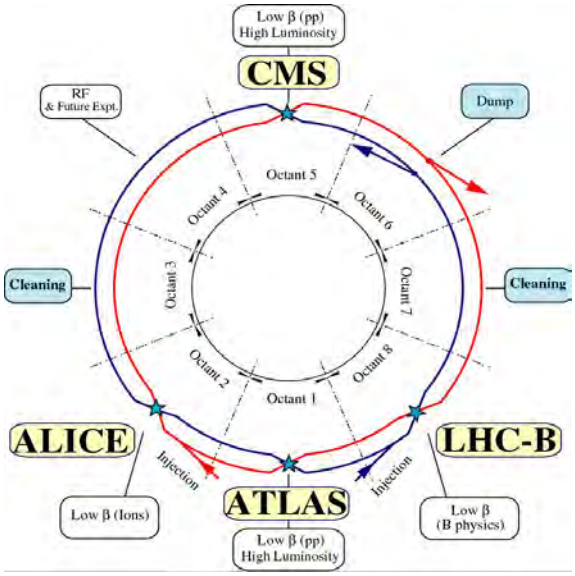

Figure 3.2: Interaction points of the LHC [Cph00].

range from as low as $p_T \sim 100$ MeV/c up to fairly high $p_T \sim 100$ GeV/c [Car04, dVa07, Tap08].

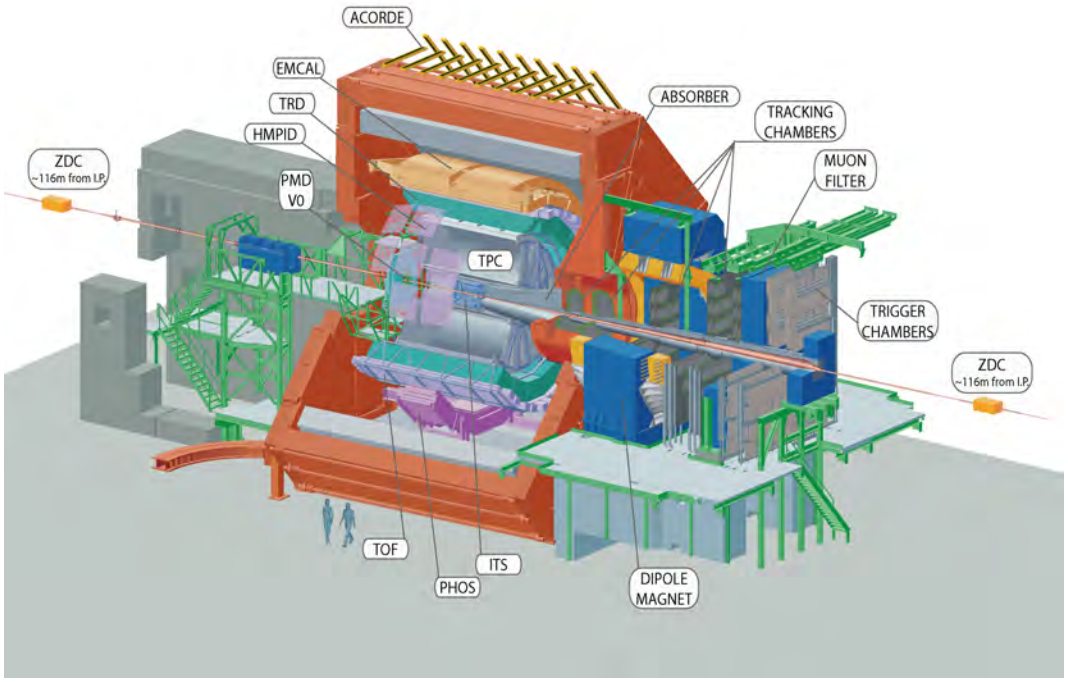

Figure 3.3: The ALICE detector [ALI00].

The central detectors cover the pseudorapidity range of $|\eta| = 0.9$ with the magnetic field of $B \leqslant 0.5\,T$ provided by the L3 Solenoid magnet. These detectors are used for tracking and identifying charged particles, neutral particles and photons.

The central barrel shown in Figure 3.4 include, from inside to outside:

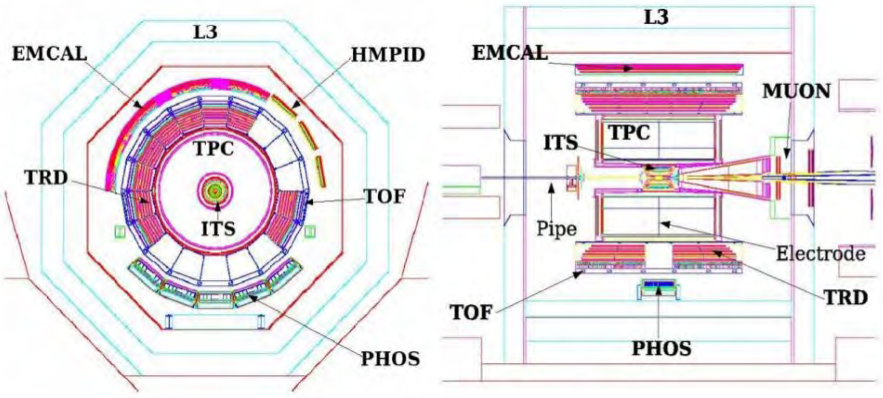

Figure 3.4: Longitudinal and transverse view of the central barrel including EMCal [Car04].

Inner Tracking System (ITS) – consists of six cylindrical layers of high resolution silicon detectors (with radius varying from 4 to 44 cm). These are pixelated, drift and strip detectors used in the inner-most to outer layers. This system of detectors is used for the primary vertex determination with a resolution better than 100 μm measurement especially the Silicon Pixelated Detector (SPD).

Time Projection Chamber (TPC) – is the main tracking system of the central barrel. It is designed to provide charged-particle momentum measurements up to transverse momentum p_T = 100 GeV/c with good particle identification and vertex determination in the high multiplicity environment expected in Pb-Pb collisions. It is 500 cm in length with an inner radius of 85 cm and the outer radius of about 250 cm. It covers a rapidity range $|\eta| \leq 0.9$.

Time Of Flight (TOF) – is a particle identification detector for intermediate momentum range (0.2 to 2.5 GeV/c) hadrons. It is 7.45 m in length with a radius of $3.5 < r < 3.99$ m.

Transition Radiation Detector (TRD) – is used for electron identification. It is situated between the TPC and TOF detectors with $2.9 < r < 3.7$ m with a length $|z| = 3.5$ m.

High Momentum Particle Identification (HMPID) – Ring Imaging Cherenkov detector is included to extend the transverse momenta coverage of particle identification. It is one of the outer detectors located at radius of 5 m, azimuthal and pseudo rapidity coverage $\triangle\varphi = 57.61°$ and $|\eta| \leq 0.6$.

Photon Spectrometer (PHOS) – to identify photons and neutral mesons. It has an azimuthal acceptance $\triangle\varphi = 100°$ and pseudorapidity acceptance $|\eta| \leq 0.12$.

ElectroMagnetic Calorimeter (EmCal)– is used for jet quenching measurements and triggering of high energy jets.

A COsmic Ray DEtector (ACORDE)– The central detectors are completed by an array of scintillators on top of the L3 magnet used to trigger cosmic rays.

The global detectors (detectors used to characterize the event) shown in Figure 3.5:

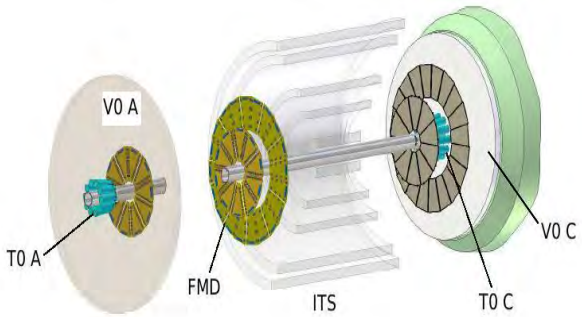

Figure 3.5: Schematic of global detectors relative to the ITS [Car04].

V0, T0, Photon Multiplicity Detector (PMD), Forward Multiplicity Detector (FMD) and Zero Degree Calorimeter (ZDC) are forward detectors used for global event characterization and triggering. The *V0* and *T0* are responsible for the measurements of particle multiplicity and beam luminosity (number of particle per unit area per unit time). Below is the equation for calculating luminosity $\mathcal{L}$,

$$\mathcal{L} = fn\frac{N_1 N_2}{A} \tag{3.1}$$

where f is the revolution frequency, n is the number of bunches in one beam in a storage ring, N_1 and N_2 are number of particles in each bunch and A is the cross section of the beam. The *ZDC* measures remnant beam particles [Car04, dVa07, Tap08].

3.2.1 The Forward Muon Spectrometer

The forward muon spectrometer (Figure 3.6) covers the pseudorapidity region $-4.0 \leq \eta \leq -2.5$ corresponding to a polar angle $171° < \theta < 178°$. It consists of:

Absorbers:

The front absorber shown in Figure 3.7 is 4 m in length which corresponds to 10 interaction length $\sim 10\lambda_{int}$ and located 90 cm from the interaction point before the tracking chambers. It is placed inside the L3 magnet as close as possible to the interaction point to reduce the forward flux of charged particles thus decreasing the background of muons from the decay of pions and kaons in the tracking chambers. It is made of carbon, concrete, tungsten, poly-ethylene and lead. The *Beam shield* is made of tungsten, lead and stainless steel to protect the tracking and trigger chambers from beam particle interactions.

The Muon filter is placed 15 m from the interaction point between the tracking and trigger chambers. It has dimensions of $5.6 \times 5.6 \times 1.3\, m^3$ and it is used to reduce background due to punch through hadrons.

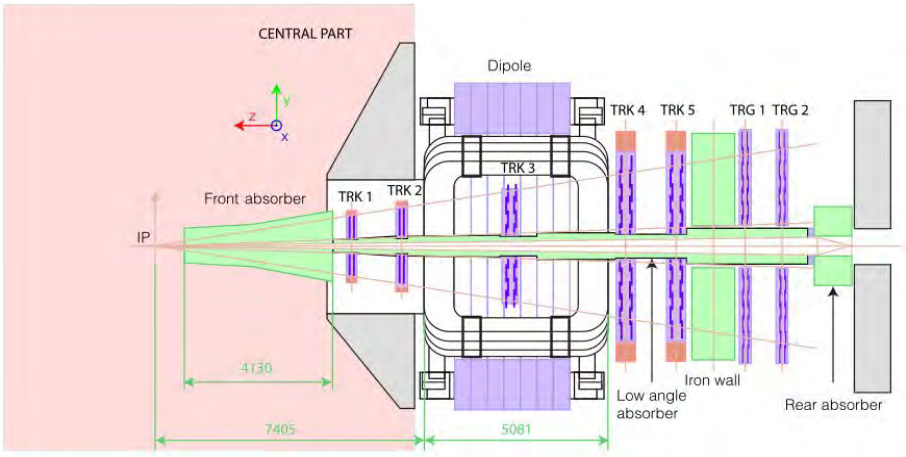

Figure 3.6: Longitudinal profile view of the ALICE muon spectrometer [Das13].

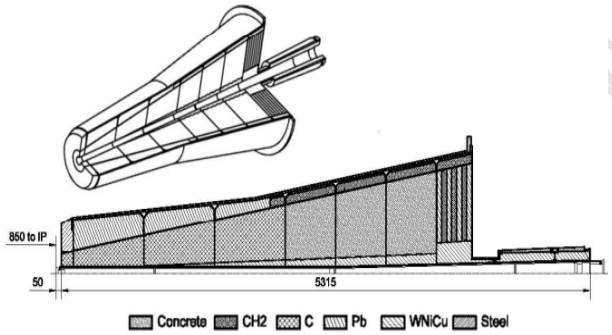

Figure 3.7: Front Absorber schematic [Car04].

Tracking Chambers:
The tracking chambers consist of five stations each with two planes of Cathode Plate Chambers (CPC) shown in Figure 3.8, with each plane separated by 5 mm with an intrinsic resolution of about a 100 μm.

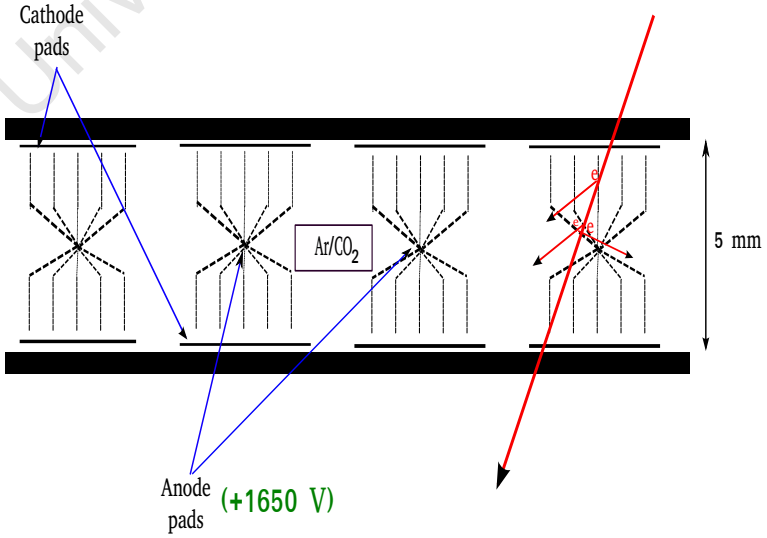

Figure 3.8: Geometry of the tracking chamber [Car04].

Each chamber in each station has a bending (plane parallel to the magnetic field)

and non-bending (plane perpendicular to the magnetic field) plane. Station 3 is placed inside the Dipole magnet with magnetic field of $B < 0.7\,T$ and maximum integrated B-field 3 Tm. The Dipole magnet is responsible for momentum determination. The separation between planes in station 3, 4 and 5 is filled with a mixture of $Ar/CO_2(80\%/20\%)$ so that a passing particle ionizes the gas creating an avalanche of electrons which then drift to the anode driven by the electric field created by a 1650 V potential difference between the cathode (planes) and the anode. The cathode pads have approximately $40\,\mu m$ position resolution. Station 3, 4 and 5 are of slats type since they do not suffer high particle flux whereas station 1 and 2 suffer a high particle flux thus requiring high granularity to handle position resolution [Car04, dVa07, Tap08], hence they are quadrant-shaped.

The readout electronics of the slats are installed on the side whereas for the quadrants they are placed over the surface. For all the stations the Front-end Electronics (FEEs) is based on a 16 channel chip called Multiplexed ANAlogic Signal (MANAS) which has the functionality of charge amplifying, filtering, shaping and track and hold. The channels of four of these chips are fed into a 12-bit Analogue to Digital Converters (ADCs) which are readout by the Muon Arm Readout Chip (MARC) which includes no suppression. The entire chain is mounted on a front-end board, MAnas NUmérique (MANU). 17 000 MANU cards are required to treat 1.08 million channels of the tracking system. The Cluster ReadOut Concentrator Unit System (CROCUS) crate is connected to the MANUs via bus patches (Protocol for the ALICE Tracking CHamber). Each chamber is readout by two CROCUS, which concentrate and format the data, transfer them to the DAQ[1] and dispatch the trigger signals coming from the Central Trigger Processor (CTP), control the FEEs and the calibration process.

Geometry Monitoring System Since the alignment plays an important role in the muon analysis, an understanding of the chamber position is needed. At the beginning of each data taking period, runs without magnetic field are recorded in order to align the ten tracking chambers with straight muon tracks, thus determining the initial geometry of the system. Switching on the magnets might have some effects on the position of the chambers with a resolution better than 40 μm. The need for better alignment is because some of the studied resonances have to be resolved to within 1%.

Triggering Chambers:
The muon trigger system which is dependent on the V0 detectors as a fast trigger to reduce background from beam interactions has two stations each with two planes of 18 Resistive Plate Chambers (RPCs) shown in Figure 3.9. The separation between the RPCs is filled with a mixture of $Ar/C_2H_2F_4/SF_2$/i-butane (49%/ 40%/ 7%/ 1%) which is specific for Pb-Pb. The trigger chambers like the tracking chambers have bending and non-bending planes. The gas mixture used in the RPCs is dependent on the experimental conditions, that is p-p, p-Pb/Pb-p and Pb-Pb. Trigger planes have a spatial resolution of about 1 cm, with a time resolution of the order of $1 - 2$ ns [Car04, dVa07, Tap08] with the efficiency that varies between 95±0.5%.

The following section describes the processes involved in preparing the ALICE muon spectrometer for data taking and the run conditions for the experiment.

[1]Data AcQuisition System described in Section 3.4

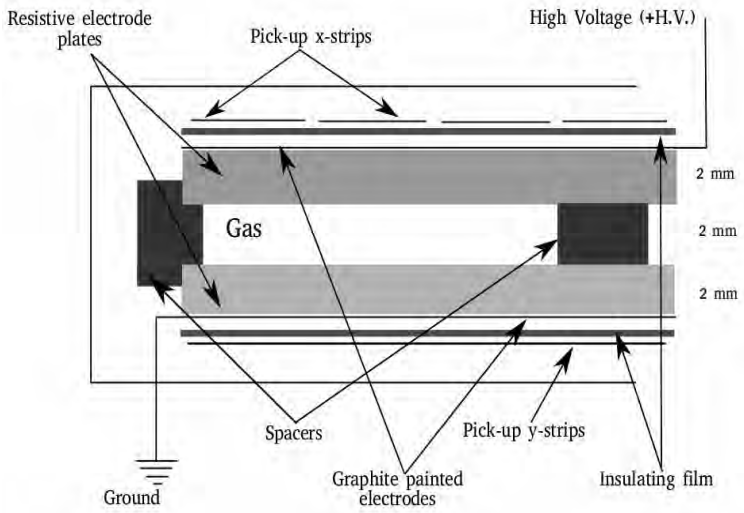

Figure 3.9: Schematic of the Resistive Plate Chambers [Car04].

3.3 Run Conditions and Data taking

3.3.1 The LHC filling scheme

The proton beams provided by LHC are according to specification by each experiment [Fer08]. The need for high luminosity by the experiments is the reason why LHC runs the proton-proton program with unprecedented number of bunches per beam. This quality is achieved by exploring the high degree of flexibility of the LHC bunch filling scheme which allows for optimization of different luminosity requirements for each experiment. In proton-proton collisions the bunch filling scheme has to take into consideration experimental boundary conditions to ensure that a maximum luminosity is delivered to IP1 and IP5 where ATLAS and CMS are respectively located, deliver the largest possible number of collisions at IP8 and finally, deliver to IP2 an average number of visible collisions per revolution around 1 ($\sim 10^{29} cm^{-29} s^{-1}$) or 20 ($2 \times 10^{30} cm^{-30} s^{-1}$). During this process the LHC has to ensure that conditions for ALICE and LHCb are implemented without or with minimal violations of conditions required for ATLAS and CMS. For the 2011 proton-proton data to be considered for this study the bunches were separated by 15 m in space and 50 ns in time (20 MHz), one orbit is equal to $\sim 89 \mu s$ and 1380 bunches in total. The ideal conditions is to have 25 ns time spacing (7.5 m) with 3564 bunches. A typical filling scheme contains information about the number of bunches in the LHC ring, their position in the orbit and number of bunches expected to collide at each interaction point, with a typical format [Fer08, Lpca]

$< \mathbf{spacing} > \_ < \mathbf{Nb} > \mathbf{b}\_ < \mathbf{IP1/5} > \_ < \mathbf{IP2} > \_ < \mathbf{IP8} > \_ < \mathbf{code} >$,

where

$< \mathbf{spacing} >$ = single, 2025 ns, 525 ns , 75 ns, 50 ns, 25 ns, etc. These refer to the bunch spacing in the main injector batches used for the filling scheme. Single means that single bunches are injected into the LHC.

$< \mathbf{Nb} >$ = the number of bunches per beam for a given filling scheme. If a probe bunch is kept (i.e. not over injected), it is not counted in the total number. The presence of a non-over injected probe bunch is encoded in the suffix $< \mathbf{code} >$.

< **IP1/5** > = expected number of colliding bunches at IP1 and IP5 for a given filling scheme.

< **IP2** > = expected number of colliding bunches at IP2 for a given filling scheme.

< **IP8** > = expected number of colliding bunches at IP8 for a given filling scheme.

< **code** > = a free suffix to encode variants in the filling scheme.

An example of a filling scheme during proton-proton collisions of in 2011 at the LHC was `50ns_1380b+1small_1318_39_1296_144bpi13inj` [ALIa, Bai03] where `50ns` is the bunch spacing, `1380b+1small` is the number of bunches in the LHC ring, `1318` is the number of bunches colliding in ATLAS and CMS, `39` is the number of colliding bunches at ALICE and `1296` is the number of colliding bunches at LHCb and `144bpi13inj` is the number of bunches per injection in 13 injections. Since ALICE suffers from pile up in proton-proton collisions less colliding bunches are delivered at the IP2 (ALICE) interaction point.

3.3.2 LHC modes and experimental Handshakes

The operational activities of the LHC are summarized and communicated to experiments through what is called LHC modes [Ale07]. Two modes are generally communicated to the experiments, namely **accelerator modes** which provides the general overview of the machine activities, e.g. proton physics, access, etc. and **beam modes** provides the state of the machine with respect to the machine cycle, e.g. injection, ramp, squeeze, etc. The Figure 3.10 shows different beam modes procedures to run the accelerator through the nominal cycle.

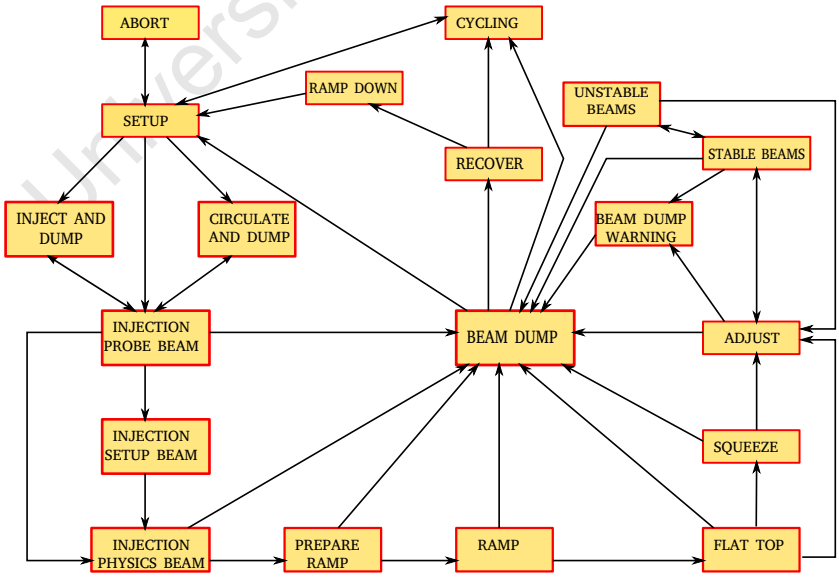

Figure 3.10: Different beam modes procedure to run the accelerator through the nominal cycle, shown are possible transition between modes [Ale07].

The LHC modes during the machine operation are communicated to the experiments through the LHC Data Interchange Protocol (DIP) [Ale07, Sal06] by different

handshakes. Handshakes [Ale11] involved during nominal sequence namely, INJECTION PROBE BEAM, INJECTION PHYSICS BEAM, PREPARE RAMP, RAMP, FLAT TOP, SQUEEZE, ADJUST and STABLE BEAMS are described below and shown in Figure 3.11.

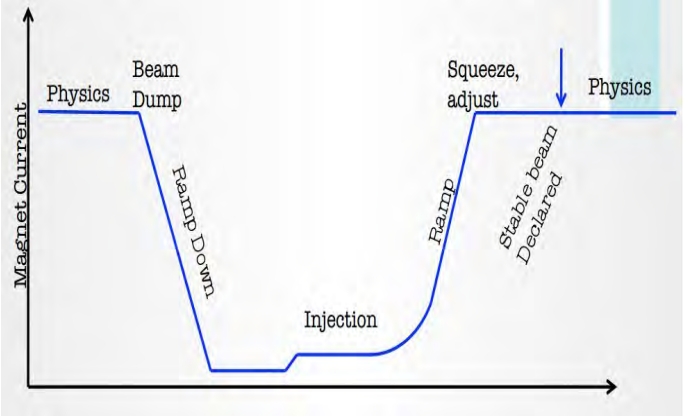

Figure 3.11: Different beam modes procedure to run the accelerator through the nominal cycle [Cam10].

INJECTION PROBE and PHYSICS BEAM during the INJECTION PROBE BEAM a single bunch is injected into the LHC ring to test beam counters and determine the background level. In the INJECTION PHYSICS BEAM the number of bunches specified by the filling scheme are injected into the LHC. In both case the proton beams from the SPS are at 450 GeV/c. During this handshake the experiments are in the safe mode.

PREPARE RAMP, RAMP and FLAT TOP during these handshakes the intensity and energy of both beams are brought to a desired value, in case of 2011 the maximum energy was 3.5 TeV per beam. The FLAT TOP is when the nominal values of intensity and energy are attained and maintained but the beams are not yet stable.

SQUEEZE and ADJUST BEAMS The SQUEEZE mode as the name suggest is when the beam transverse (emittance[2]) profile and cross-sectional (known as amplitude function, β[3]) of the beam is reduced thus increasing the likelihood of particle interaction. The ADJUST mode has to do with the point of interaction, the collision should occur in the certain region (diamond). The distance within which the cross section of the beam can be reduced from σ to 0.5σ is known as β^*, the β^* for ALICE is 10 m for p-p collisions and much less for Pb-Pb.

STABLE BEAMS The STABLE beams are declared when the collimators reach the physics settings, background and life time are under control and the beams are colliding.

The LHC communicates any critical action they intend to undertake to the experiments and require a response before taking any action, this are called permits. The Final State Machine of the LHC is broad-casted to the experiments so they can respond and condition themselves accordingly.

[2]emittance is the beam property related to the bunch preparation.

[3]Beta function is the beam optics quantity related to the accelerator magnet configuration, it is related to emittance by: $\beta = \pi\sigma^2/\varepsilon$, where ε is the emittance.

3.3.3 ALICE Run Conditions

The **handshakes** described are communicated to the experiment via the Detector Control System [Ali04, ALI07]. In the DCS the handshakes are handled through the Safety Matrix which is based on the ALICE Final State Machine (FSM) described in Figure 3.12. This FSM shows possible modes of ALICE detectors.

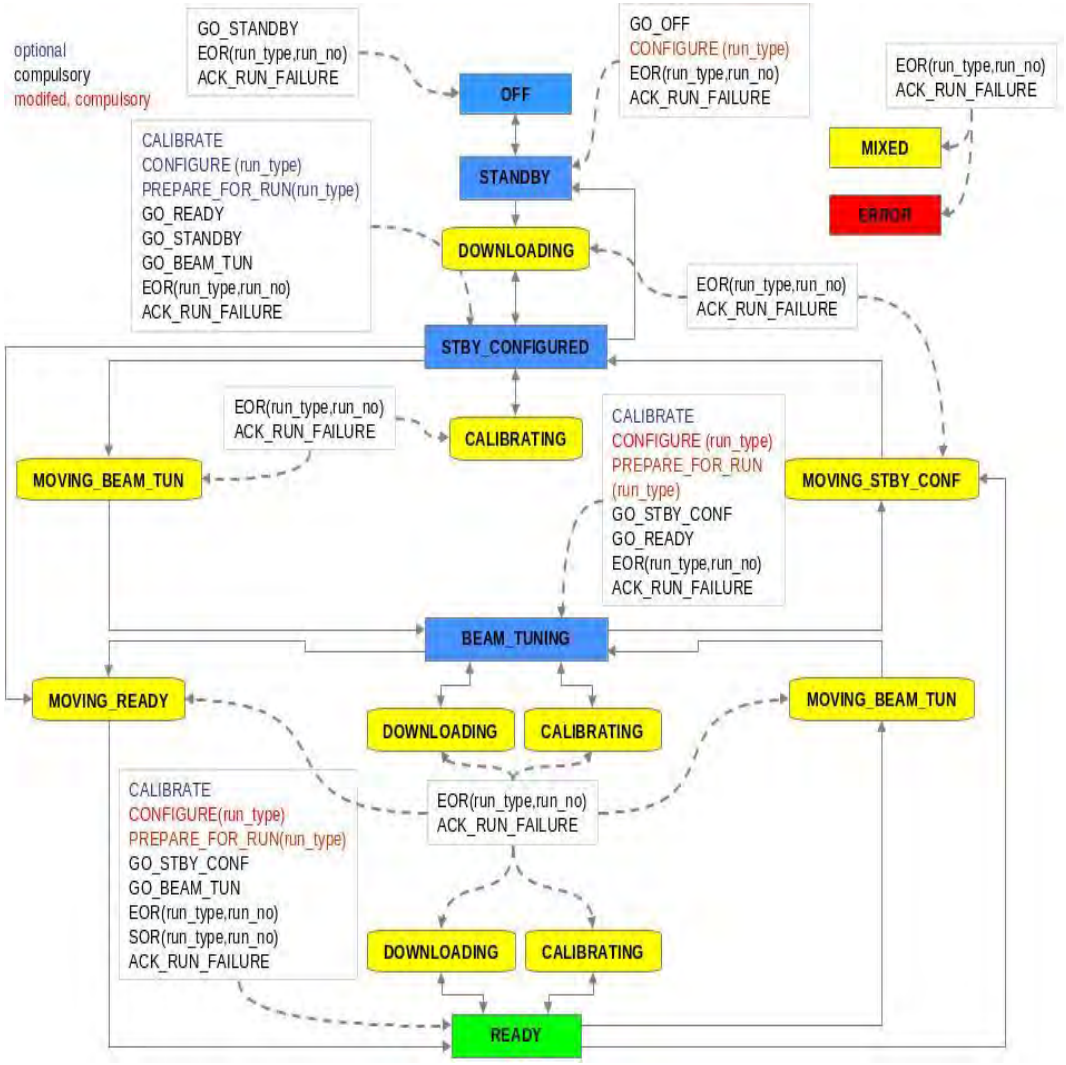

Figure 3.12: ALICE DCS Final State Machine diagram [ALI07].

The ALICE muon spectrometer has five possible FSM modes, namely, OFF, STANDBY, STANDBY CONFIG, BEAM TUNING and READY [ALI07]. In the OFF state all the devices (Low Voltage Power Supplies (LVPS), High Voltage Power Supplies (HVPS), CROCUS, channels, etc.) are OFF, at this stage the DCS operator can send a GO_STANDBY command to take it to STANDBY which switch on the CROCUS, LVPS and HVPS. In STANDBY the devices are configured with the power-on defaults and no external data can be loaded. In STANDBY_CONFIGURED the external data can be loaded (e.g. tracking softwares, etc.) the LVPS, HVPS and CROCUS are ON but the HVPS are set to minimum possible value (∼600 V) not to exceed the beam safe thresholds. BEAM_TUNING is the next state which is compatible with the LHC INJECTION/RAMP DOWN and ADJUST handshake and tests this is the SAFE state of the MUON TRACKER (Chamber) where the Low Voltage Power Sup-

plies (LVPS) are ON and the High Voltage Power Supplies (HVPS) are at 1200 V voltage. In BEAM_TUNING a pedestal run can be taken to determine the electronic noise and also a calibration run which should be done at least every few hours. In the READY state when the detector is ready for data taking the LPVS and HVPS (1650 V) are at their nominal voltage and the Frontend Electronics and ReadOut are ON and configured.

3.4 ALICE Online and Offline

The analysis framework is comprised of the Online System which perform analysis during data taking in a form of triggers and an Offline system which perform event reconstruction and enables data analysis [Ali04]. Shown in Figure 3.13 below is the data flow from the Online to the Offline system for event reconstruction interfaced with Data AcQuisition System (DAQ).

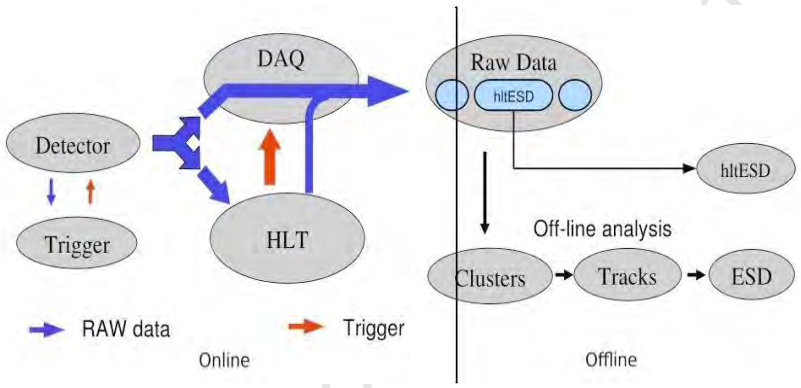

Figure 3.13: Raw data flow scheme showing the relationship between Online and Offline [Ric09].

3.4.1 Online Framework

The Online framework is a system of triggers and monitoring systems used during data taking. It is used for online events characterization, triggering and monitoring the data taking conditions. The data taking conditions are then saved to the Offline Conditions Database (OCDB) to be used in reconstruction. The Online framework comprises of 5 systems namely: Data Acquisition System (DAQ), Experiment Control System (ECS), High-Level Trigger (HLT), Detector Control System (DCS) and Trigger, the collection of these controls constitutes the ALICE control system [Ali04]. These systems are interfaced with each other through ECS shown in Figure 3.14. The role of the DCS which entails detector control was described in the previous section, in addition it is also used to interface the ALICE control system with the LHC and the environment monitoring systems as seen in Figure 3.15.

The ECS role is to determine the state of the detector and relay the information through the FSM. The ECS decides whether or not the non-operational part of the experiment is beyond the critical state to take data or pause until the sub-detectors are recovered, also it is used for partitioning of the experiment, whereby sub-detector can be operated independently and/or concurrently. This can be done to create clusters for different physics. The Muon Tracker cluster for the 2011 proton-proton period

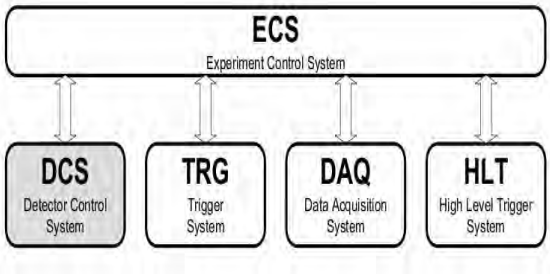

Figure 3.14: Schematic of the Online framework. ECS controls all operation and interplay, while DCS handles the communication between systems [Ali04].

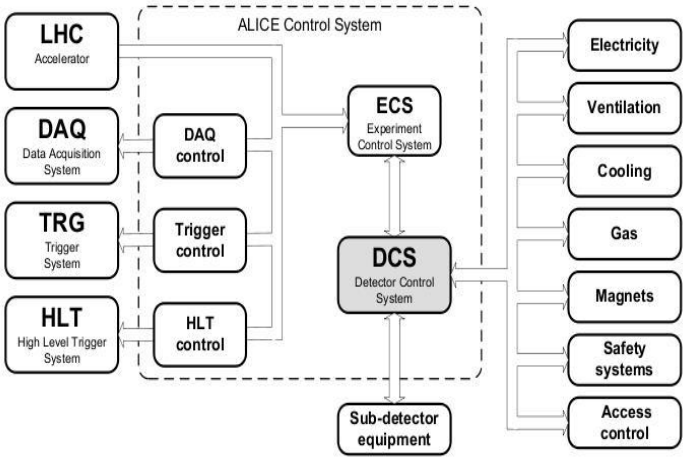

Figure 3.15: The ALICE control system [Ali04].

consisted of (MUON_TRK, SPD, V0, T0, TRIGGER, etc) as read-out detectors and (MUON_TRG, V0, etc) for triggering.

The trigger signals from detectors are sent to the Central Trigger Processor (CTP) [Eva05] as trigger input where they are combined to form different triggers (minimum bias, dimuon event, etc). The CTP in addition synchronizes the ALICE clock with the LHC clock cycle, adds pile-up protection and selects events with different features and provides scaling down of event rates to fit the DAQ bandwidth with data flow. The output trigger signal is then sent to the Local Trigger Units of each sub- detector to be further processed and sent back to the Front End Electronics (FEEs). The trigger is divided into three levels (L0, L1 and L2) to take care of different process time of sub-detectors. The faster trigger signal L0 is sent by faster detectors (SPD, V0, T0 and muon trigger) to the CTP within $1.2\,\mu s$, the L1 trigger cluster is sent within $6.5\,\mu s$ and the slower trigger are dependent on the TPC drift-time of $88\,\mu s$. The muon trigger contributes to the L0 cluster. To reduce the flow of data to DAQ the triggers are divided into rare and common. When the DAQ data flow reaches a certain high threshold the common triggers are switched off to record only rare events. After trigger signal processing the data is sent to DAQ. Figure 3.16 shows the architecture of the ALICE DAQ.

The ALICE Data AcQuisition System has been designed to deal with extreme data taking conditions. In proton-proton collisions it deals with high rates although with small event size 100 MB/s and in lead-lead collisions it deals with lower rates and large

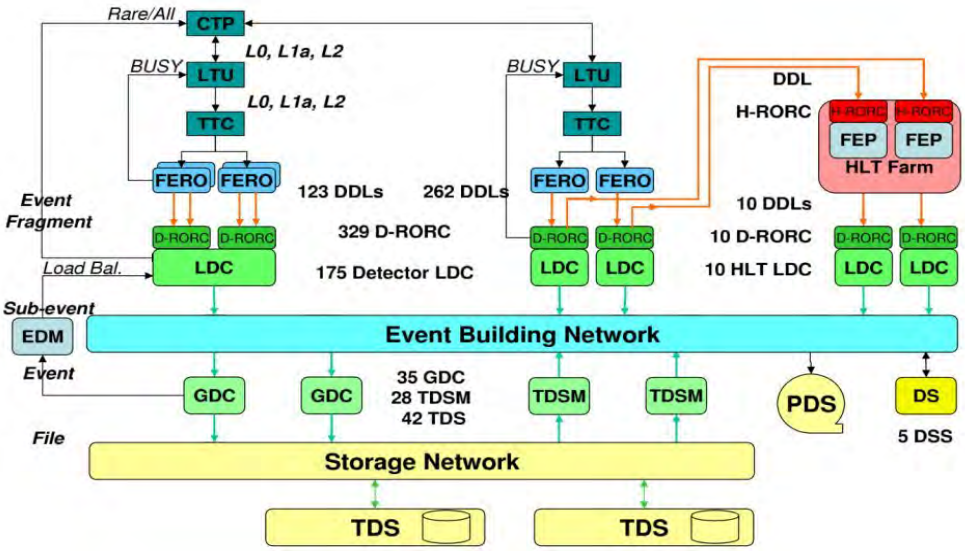

Figure 3.16: The architecture of the ALICE DAQ and the interface to the HLT system [Ali04, Zha12].

event size 1.25 GB/s. When the CTP has processed the trigger and made a decision for example on the muon trigger event, the signal is sent to the muon trigger FERO then to Local Data Concentrators which are responsible for sub-event building. The role of the HLT is to select the most relevant data and thus reduce the data volume an order of magnitude while preserving the physics information and accept and reject the events based on detailed online analysis. The sub-events from LDCs and HLT are combined by Global Data Collectors to build the whole event then send it to the Permanent Data Storage [Ali95, Car04].

The data quality monitoring is done through the DAQ software framework (Data Acquisition and Test Environment (DATE)) which controls the DAQ hardware elements, and synchronizes the processes running in the LDCs and GDCs. The DATE performance is addressed by the DAQ performance monitoring software (AFFAIR) package. Data Quality Monitoring includes also online monitoring using Monitoring Of Online Data (MOOD) and environment monitoring using Automatic MOnitoRing Environment (AMORE), which are used to handle the detector status, online and offline data stream, etc. These programs monitor the physics data during physics run and accumulate plots that can be inspected to check the DAQ performance [Ali95, Car04, Zha12].

3.4.2 Offline Framework

The ALICE analysis framework AliROOT [ALI13] has been developed since 1998 by the offline core team and collaborators. It is based on Object Oriented programming (C++) on a ROOT [Bru95] platform. It provides an environment for the development of software packages for event generation, detector simulation, event reconstruction and data acquisition and analysis. The objectives of the AliROOT framework are:

- simulate primary hadronic collisions and the resulting detector response.
- reconstruction of physics data coming from real events and simulated events.

- analysis of reconstructed data.

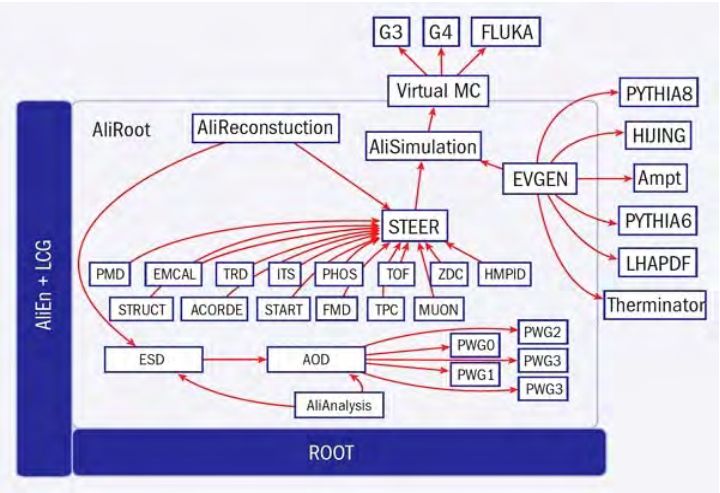

Figure 3.17: Schematic view of the AliRoot framework [Car04].

AliROOT was designed with a basic principle of re-usability and modularity, which minimizes the amount of user code unused or rewritten and ensure that a change in part of the system does not impact other parts [Car04]. The AliROOT framework is schematically shown in Figure 3.17. The STEER module provides steering, run management, interface classes and base classes. Each detector has independent codes for simulation and reconstruction (modularity) and the analysis code is continuously developed and added. A detailed description of the detection conditions, shape, alignment and structures are updated on a run-to-run basis and stored in the Offline Calibrations Database as part of the framework. This framework can interface with different Monte Carlo modules for event generation (PYTHIA, PHOJET, etc) and detector simulation (GEANT3 [Apo94], FLUKA [Fer05], etc). The role of the offline framework (AliROOT) is shown in Figure 3.18.

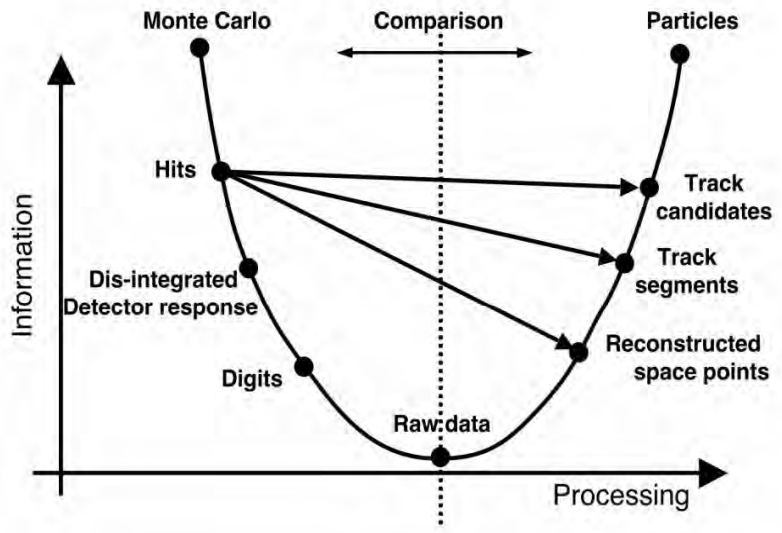

Figure 3.18: Schematic view of the AliRoot framework [Car04].

ALICE Distributed Computing Grid

At the rate of 1.25 GB/s data flow in Pb-Pb ALICE faces a challenge in data storage and due to international collaboration the computing resources are distributed. The computing resources are distributed in a hierarchy of centers called Tiers, where Tier-0 is at CERN, Tier-1 are major computing centers, Tier-2 are smaller computing centers, Tier-3 are university computing centers and Tier-4 is the user work station. Raw data storage and reconstruction is done at CERN where a Tier-1 for each experiment is housed, Tier-2 is responsible for Monte Carlo production and analysis. This model of distributed computing is called the Monarc model [Smi00] shown in Figure 3.19. To offer a transparent access to computing resources and data ALICE developed a platform AliEN [Sai03] (ALIce ENvironment) which is distributed worldwide. The main components of AliEN are authentication and authorization[4], job management [5], file catalogues[6] and Application Programming Interface[7].

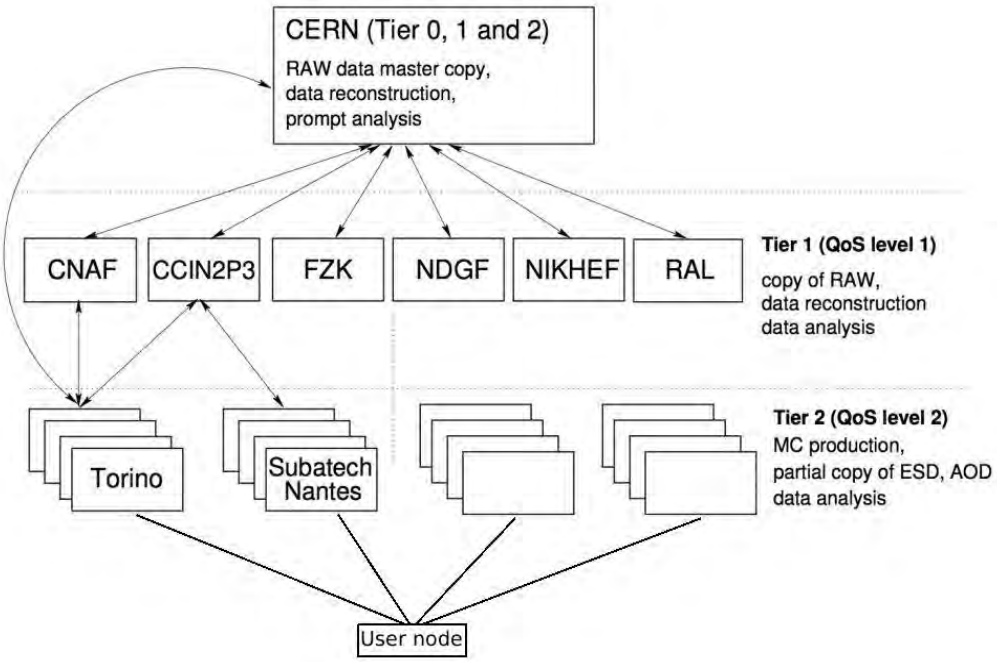

Figure 3.19: Schematic view of the Tier structure with the added user node [Zha12].

The results of the analysis of experimental data are presented in Chapter 4 while the simulation and the simulation signal are described in the AliROOT framework in Chapter 5 using the Grid.

[4]Authentication and authorization allows for the user to access the Grid and Data.

[5]Job management validate and submit jobs according to the created Job Management Language, monitor CPU time, etc.

[6]"File catalogues input and output associated with any job is registered in the AliEn File Catalogue controlled by the Data management" Zhang et al. PhD Thesis (2012).

[7]Application Programming Interface services to provide an AliEn interface in ROOT.

Chapter 4

Experimental Results

The analysis is based on the Analysis Object Data (AOD) produced by filtering Event Summary Data (ESD), this is where the physics selection is applied. The physics selection task selects collision candidates (physics events) from data, performs an offline validation of online triggers and rejects background (beam gas) based on the content of the Event Summary Data (ESD). The ALICE Run Condition Table (RCT) [ALIb] was used to obtained the runs satisfying the global quality assurance and the muon quality assurance [MuoQA]. The data quality assurance rejects the bad runs which are not suitable for the physics analysis, e.g. runs in which a large part of detector elements and/or electronics are missing or not working properly during data taking or runs with high pile-up, since the pile-up correction of these events is not available during data taking/online. The analyzed runs are shown in the Appendix III part III.

4.1 Data taking conditions in proton-proton collisions at $\sqrt{s_{NN}} = 7$ TeV

The LHC delivers different beam luminosity to experiments according to their requirements and specific run conditions which are based on the physics of interest. Unlike other LHC experiments ALICE is designed for heavy ion collisions. Although ALICE is studying proton-proton collisions it is for the purpose of comparison with lead-lead collisions and proton-lead/lead-proton collisions because in proton- proton ALICE has to keep the probability of collision pile up per triggered events below 2.5%. The variation of the delivered integrated luminosity by the LHC to the experiments is shown in Figure 4.1 below.

The data sample collected in the 2011 proton-proton collisions at 7 TeV center of mass energy corresponds to an integrated luminosity of $16.5\,nb^{-1}$. This data consist of muon triggered events which require that in addition to minimum bias trigger a muon above a certain transverse momentum reaches the Muon Trigger system. The minimum bias (MB) trigger requires a signal coincidence in the two beam counters, a hit in the SPD and a hit in one of the V0 scintillators. In addition to MB trigger the Muon Trigger requires a hit in at least three of the four triggering planes of a muon above a certain transverse momentum threshold [Abe12a]. The muon low transverse momentum threshold in this data taking period was set to 1.0 GeV/c. To maintain the luminosity ($\sim 2 \times 10^{30} cm^{-2} s^{-1}$) within the range required by ALICE the beams are displaced in the transverse plane (e.g. Figure 4.2 below) by 3.8 times the root mean square of their transverse profile, this allows to keep the probability of MB multiple

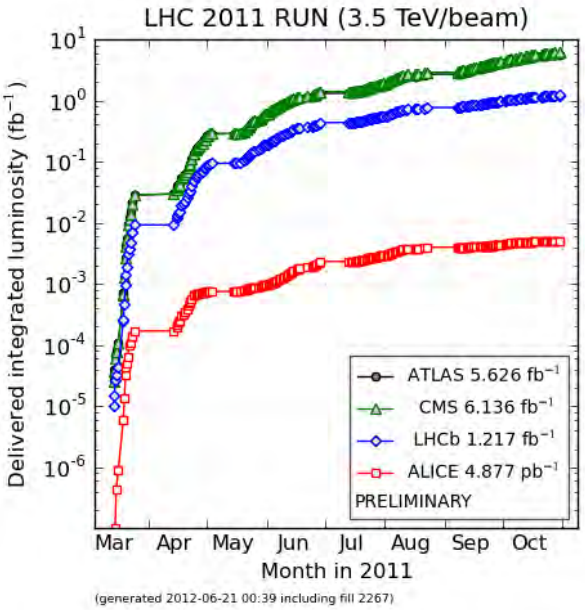

Figure 4.1: Integrated luminosity delivered by the LHC in 2011 data taking period in proton-proton collisions [Lpcc].

interactions per bunch crossing below 2.5%. This delivered luminosity corresponds to a single Muon Trigger rate of about 500 Hz [Bos12].

Figure 4.2: Schematic showing how luminosity can be adjusted by displacing the beam in the plane perpendicular to the beam axis.

4.2 Data Sample and Quality Assurance for Muon Analysis

The quality assurance was mentioned briefly in the introduction to this Chapter, in this section a further elaboration is given. The Quality Assurance (QA) has two parts, the global QA and Muon Spectrometer QA. Let us look first at global QA which identifies and rejects bad runs according to the following conditions:

- for a given data taking period different runs are recorded according to different requirements namely, detector calibration, luminosity measurement, pedestal runs,

etc. And the runs for physics analysis are stored in the "PHYSICS"partition. This selection is the first step of the QA (information available in the log-book).

- a run should be at least be 10 minutes long with at least 5000 sub-events.
- the beam status and energy is also checked, at $\sqrt{s_{NN}}$ =7 TeV in proton-proton collisions; the beam energy should be 3.5 TeV for each beam. If not the status for the beam is not stable and the run is discarded.
- also the DAQ system should be checked to see if data is correctly recorded in the GDCs and finally the L3 and the dipole are checked for the correct current value, correct polarity in case of the dipole magnet and stability.

In the case of the MUON QA the conditions are as follows:

- the Muon Trigger as mentioned before is required and the readout detectors should include both the MUON Trigger and Tracker stations as well as the V0 and SPD.
- the detector configuration is checked, if the average number of clusters per track per chamber is above 0.75 the run is accepted for physics analysis. The nominal value if there are no problems is 0.9 [Zha12].

The runs used in this analysis were taken from the QA page [MuoQA] which redirects to the selected good runs in the RCT, these are the runs that have passed the conditions for global QA and MUON QA described above. During data taking the MUON Tracker and Trigger system record data independently and in the QA analysis the tracks in both system have to be matched. The example of a QA plot is shown in Figure 4.3(a). In this period the average momentum resolution ($\Delta p/p$) was $\sim$ 3% at 100 GeV/c and the momentum resolution of the chambers was 200 microns in the bending plane whereas in the non-bending plane it was 600 microns on average [Pil13] and the efficiency was about 81.43±0.01% [Pil12] seen in Figure 4.3(b) [Bos12]. The Muon Trigger efficiency seen in Figure 4.3(c) is almost always constant around 95±0.5%. The track and event selection for our analysis is described in the next section.

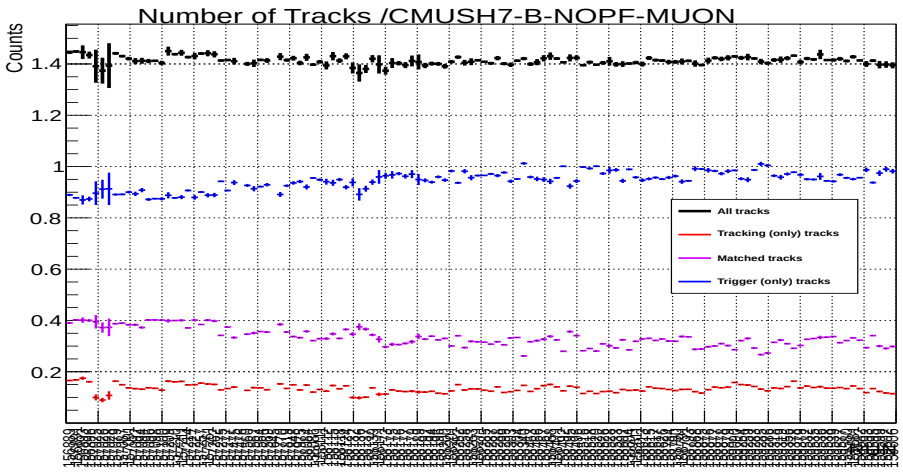

(a)

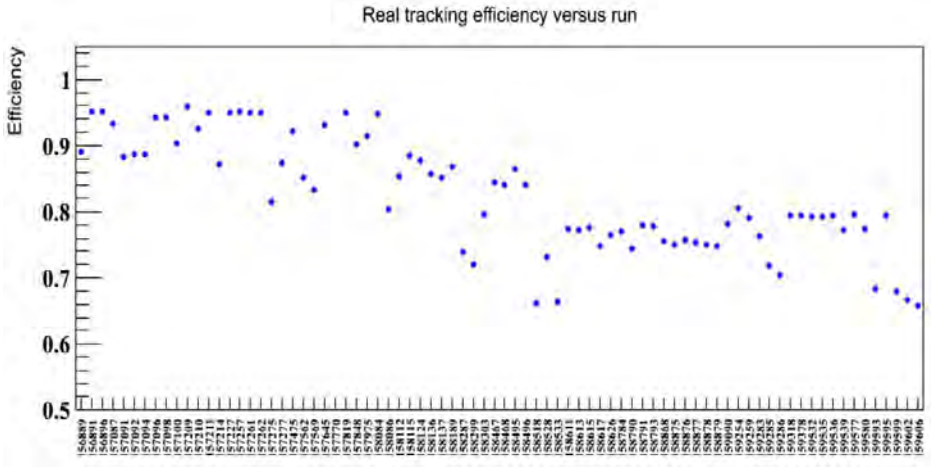

(b)

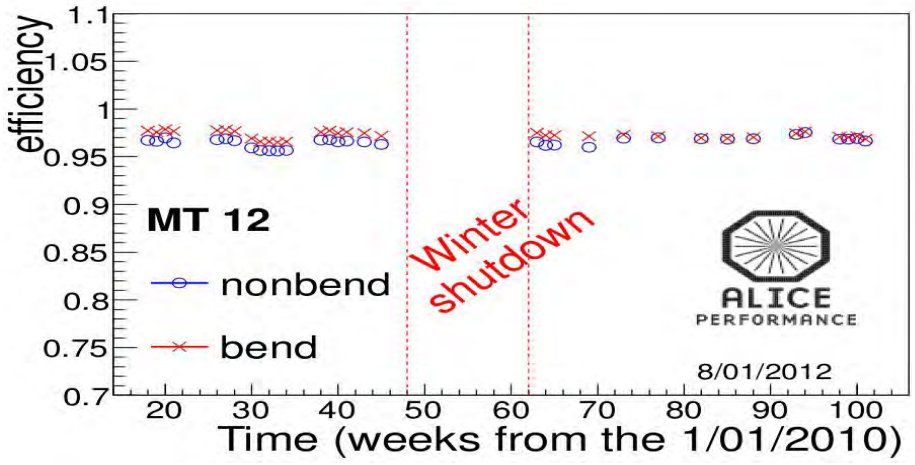

(c)

Figure 4.3: (a) Plot of a QA plot from LHC11d period showing tracker tracks, trigger tracks, matched tracks and all tracks for `CMUSH7` trigger [MuoQA], (b) is the Muon Tracker efficiency per run from LHC11d [Pil12] and (c) Muon Trigger efficiency from beginning of 2010 to the end of 2011 data taking [Bos12]. In (a) and (b) on the x-axis are the run numbers for the LHC11d period.

4.3 Track and event selection

The tracks corresponding to events which passed the physics selection are reconstructed in the Muon Spectrometer acceptance with pseudorapidity $\eta\ \epsilon(-4.0, -2.5)$ and $171° < \theta_{abs} < 178°$, where θ_{abs} is the track polar angle measured at the end of the absorber. Then, these tracks measured in the tracking chamber are required to match the corresponding tracks in the trigger chamber. The trigger distinguishes tracks with different transverse momentum. In this case the hardware trigger was set to 4.2 GeV/c for high momentum muons and the same is asked of the software gate in the offline. The p×DCA is used to reduce the beam induced background whose p×DCA distribution does not follow the Gaussian distribution expected from tracks pointing to the interaction vertex. p×DCA is the correlation between the momentum (p) and the Distance of Closest Approach (DCA), where DCA is the distance between the extrapolated muon track and the interaction vertex in the plane perpendicular to the beam axis containing the vertex. The p×DCA is set at 6σ where σ is the width of the p×DCA Gaussian distribution at half the maximum value. These four conditions are used in the analysis and are implemented through the `AliMuonTrackCuts`[1] class. Only tracks with a reconstructed primary vertex were considered from the events. In addition, the tracks are required to correspond to certain event triggers where in proton-proton collisions events were selected using the trigger class for the high momentum muon tracks ($\mathbf{H_{P_T}}$) `CMUSH7-B-NOPF-MUON`[2] and also required to have a reconstructed primary vertex shown in Figure 4.4 which takes care of pile-up correction due to the absence of past and future protection during data taking.

Cuts	Events	Tracks
H_{P_T} (Online)	✓	✓
Vertex Point	✓	✓
Geometrical cuts (η and θ)	×	✓
p×DCA)	×	✓
H_{P_T} (Offline)	×	✓

Table 4.1: The table showing cuts applicable to either an event or track, the tick is a representation that the cut is applied and the check indicate that the cut is not applied.

[1] `AliMuonTrackCuts` is the class which takes care of implementing the standard geometrical cuts, p×DCA and different offline momentum cut.

[2] `CMUSH7-B-NOPF- MUON` is the high momentum trigger, Class of High-momentum Single MUons (CMUSH), B - shows that there is beam trigger on the A and C sides and NOPF - no past future protection.

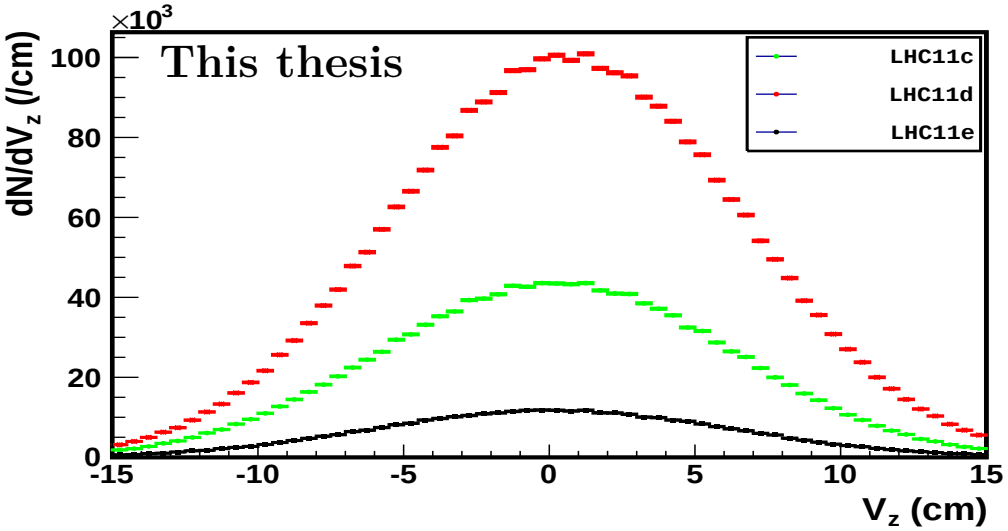

Figure 4.4: Vertex distribution of muon tracks matching $\mathbf{H_{P_T}}$**=4.2 GeV/c** trigger for the three periods LHC11c, LHC11d and LHC11e obtained from 2011 pp at 7 TeV is analyzed in this work.

4.4 Results

The results are presented in three sections, the first section shows the P_T distribution obtained from all muon track in pp collisions at 7 TeV for three periods of 2011 data taking period, namely LHC11c, LHC11d and LHC11e, the second section presents the η and P_T distributions of positive and negative muons and the third section presents the ratio of positive to negative muon distributions.

4.4.1 P_T distributions for all muon tracks obtained in pp collisions at 7 TeV

In Figure 4.5 we show the yield ($\frac{dN}{dP_T}$) plotted against the transverse momentum (P_T) of muon tracks obtained from 2011 pp collisions at 7 TeV for periods LHC11c (green), LHC11d (red) and LHC11e (black) shown in Figure 4.5(a) and Figure 4.5(b). Figure 4.5(c) taken from the existing Performance Study by [dVa07] shows the differential cross section of different muon contributions. Figure 4.5(a) shows the results of the three periods where no cuts are applied (without cuts) whereas Figure 4.5(b) show the distribution of tracks passing all the selections mentioned Section 4.3 without specifying the track charge. The predominance of the yield for the LHC11d period in Figure 4.5(a) can be attributed to the increase in luminosity shown in Figure 4.1, although there was an increase in luminosity in LHC11e the low yield is due to fact that not all runs were reconstructed due to pile-up problem and large beam gas interaction. From Figure 4.5(b) it is clear that applying track and event selection change the distributions especially in high momentum region $P_T > 20$ GeV/c. The high momentum tracks discarded by the cuts and the event selection might have been due to beam gas interactions, that is particles with large $\mathbf{p} \times \mathbf{DCA}$ which are most likely beam particles. Table 4.2 shows the effect of the cuts on the number of entries. After applying the track and event selection the results obtained from the three periods show a consistent

inverse decrease of entries per bin with increasing transverse momentum below $P_T \lesssim$ 20 GeV/c. The three periods exhibits a similar trend below $P_T = 20$ GeV/c, whereas above this P_T the lack of statistics is pronounced. Above $P_T = 40$ GeV/c the distribution of LHC11c and LHC11d drops to a plateau, thereby creating a small "bump" in the P_T region 30 - 50 GeV/c although with large error bars. The error bars at P_T >40 GeV/c are small for the period with more entries, in this case LHC11d (shown in red asterisk) and larger for LHC11e. This is because of the availability of statistics thus reducing the uncertainty in measurement. However the average uncertainties (error bars) based on the Root Mean Squares (RMS) for the three periods are 1.855 c/GeV, 1.862 c/GeV and 1.887 c/GeV for LHC11c (shown in green), LHC11d (shown in red) and LHC11e (shown in black) respectively. Table 4.3 shows the number of muons in the 30 - 50 GeV/c P_T region of interest where $W^{\pm}$ is expected to be dominant.

Shown in Figure 4.5(c) are distributions of all single muon contributions ($W^{\pm}$, charm, beauty as well as Z^0) and shown in black is the sum of all contributions. A qualitative comparison is made between three P_T distributions in 4.5(b) and the black distribution in 4.5(c) taken from the Performance Study by [dVa07] which is a differential cross section ($\frac{d\sigma}{dP_T}$) versus P_T. It should be noted that the comparison is only qualitative since in the Performance Study [dVa07] the pp collisions were simulated without realistic nor ideal detector configuration, that is fast simulation (kinematics only), and in addition also the center of mass energy was different (14 TeV) and as well a different PDF (CTEQ4L) was used. As shown in Figure 4.5(c) in the P_T region 30 - 50 GeV/c region we expect muons from $W^{\pm}$ ($W^{\pm} \rightarrow \mu^{\pm} + \nu_{\mu^+}(\bar{\nu}_{\mu^-})$) to dominate the single muon P_T distribution, whereas the P_T region below $P_T < 28$ GeV/c is expected to be dominated by heavy quarks (charm and beauty quarks), with a cross over at 28 GeV/c. However due to low statistics for all three periods in pp collisions at 7 TeV in 2011, especially in this region of interest, $30 \lesssim P_T \lesssim 50$ GeV/c, one cannot make any conclusive remarks but only to demonstrate and point out that the distributions from the current 2011 experimental data especially LHC11d shows a similar shape as the one exhibited by the black line (all single muon contributions) from [dVa07] shown in Figure 4.5(c). This comparison is done to show the expected bump.

	N_{tracks} (LHC11c)	N_{tracks} (LHC11d)	N_{tracks} (LHC11e)
No Cuts	2 940 756	6 549 659	924 664
Cuts	1 313 493	2 992 360	360 727
% of tracks passing cuts	44.67	45.69	39.01

Table 4.2: Number of entries of muon tracks in LHC11c, LHC11d and LHC11e with and without cuts.

	$N_{\mu^{\pm} \leftarrow \text{All}}$		
P_T	LHC11c	LHC11d	LHC11e
(30,50)	193	427	48

Table 4.3: Number of muons in the region of interest P_T = 30 - 50 GeV/c.

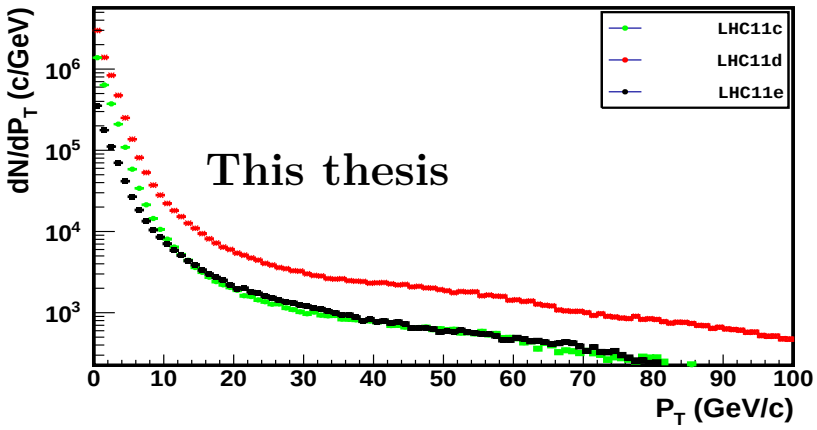

(a)

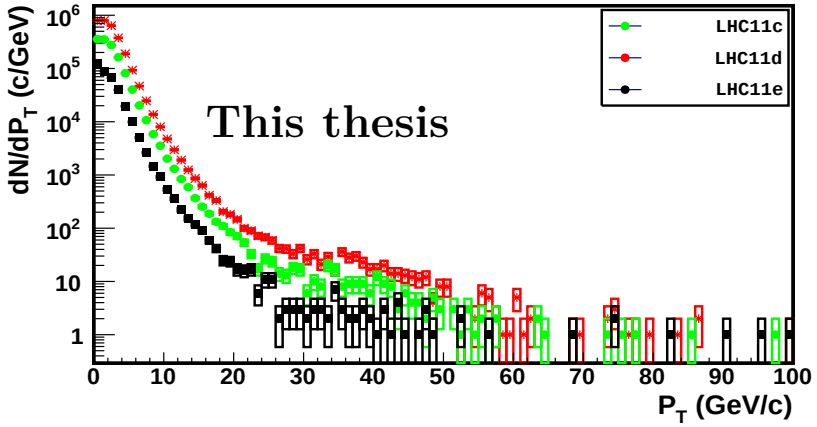

(b)

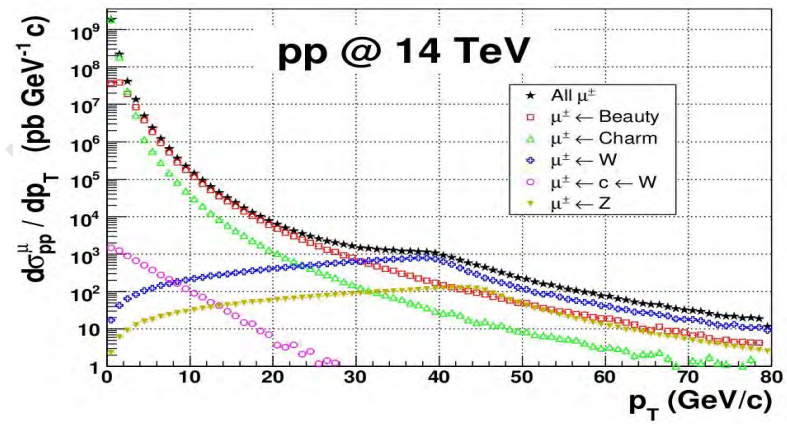

(c)

Figure 4.5: P_T distribution of muon tracks obtained from pp collisions at 7 TeV for periods LHC11c, LHC11d and LHC11e, (a) without cuts and (b) passing standards cuts and the high momentum trigger threshold. Shown in (c) is the cross-section against P_T muon from different sources in a pp fast simulation at 14 TeV in 4π from the Performance Study by [dVa07]. The boxes (rectangles) represent the statistical error.

4.4.2 Eta (η) and P_T distributions of positive (μ^+) and negative (μ^-) muons obtained in pp collisions.

Figures 4.6(a) and 4.6(b) show the yield of positive (red points) and negative (black points) muons as function of pseudorapidity (η) and transverse momentum (P_T) in the Muon Spectrometer acceptance $-4.0 < \eta < -2.5$ respectively for LHC11c period. The distributions in Figure 4.6(a) exhibit a different trend (shape) where the yield of negative muons is higher than that of positive muons by a factor ~ 1.2 on average. In the region between $-3.8 < \eta < -2.8$ the yield of negative muons steadily decrease from $dN/d\eta \sim 10\,000$ to $dN/d\eta \sim 8500$ and then slightly increase between $-2.8 < \eta < -2.6$. In contrast, the shape of the η distribution of positive muons does not exhibit any significant change in shape and that the yield is almost constant at $dN/d\eta < 8000$ for bin $-3.85 < \eta < -3.2$ with a slight decrease in $-3.2 < \eta < -2.85$. Both distributions show a drop of yields in the bins $\eta \sim -2.95$ and $\eta \sim -3.95$, this drop in the $\eta = -3.95$ bin might be attributed to the muons which were initially out of acceptance scattering back into the detector. The difference in the number of entries between positive and negative muons is due to charge asymmetry in track reconstruction. More negative muon tracks were reconstructed [MuoQA], see Figure 4.6(c) where the difference in the number of positive and negative muon tracks per run is plotted. The transverse momentum distribution in Figure 4.6(b) shows an inverse dependence of the yield with increasing P_T. The yield shows a sharp decrease from $\sim 10^5$ c/GeV to about 10 c/GeV in the region $1.0\,\text{GeV/c} < P_T < 20\,\text{GeV/c}$ followed by the flattening of the yield at $P_T > 20$ GeV/c due to lack of statistics. This lack of statistics leads to large error bars in this high momentum region. Figures 4.7(a) and 4.7(b) show the yield of positive (red points) and negative (black points) muons as function of pseudorapidity (η) and transverse momentum (P_T) in the Muon Spectrometer acceptance $-4.0 < \eta < -2.5$ respectively for LHC11d period. Similarly, the η and P_T distributions shows the same behavior as those shown in Figure 4.6, where we observe that due to charge asymmetry in the reconstruction seen in the MUON QA [MuoQA] for the period LHC11d in Figure 4.7(c) the number of reconstructed negative muon tracks is much higher than that of positive muons. In addition, the shape of positive muon is also not showing any significant change. However, it must be noted that a number of tracks for both positive and negative muons obtained in the LHC11d period is significantly larger (the number of entries of LHC11c is 44.89% those of LHC11d) than that obtained in LHC11c period due to increased luminosity from $\sim 1.975\,\text{pb}^{-1}$ to $\sim 2.975\,\text{pb}^{-1}$ as already discussed in Section 4.4.1. The decrease in both yields ($dN/d\eta$) for positive and negative muons in the bins $\eta \sim -3.95$ as well as $\eta \sim -2.95$ is also observed in this period. The P_T distribution shown in Figure 4.7(b) exhibit the same shape as the one in Figure 4.6(b), however in this case the distribution of positive muons hint to a formation of a "bump" at $P_T = 35$ - 46 GeV/c which was not seen in Figure 4.6(b). Above $P_T = 46$ GeV/c the yield flattens due to lack of statistics in this region. It is evident that the statistical fluctuation increases with increasing transverse momentum. Unlike the two cases discussed above in Figures 4.6 and 4.7, in Figures 4.8(a) and 4.8(b) we observe that although the yield of positive muons is higher than that of negative muons due to the charge asymmetry in reconstruction as obtained from the MUON QA shown in Figure 4.8(c) for LHC11e period, however the η distribution shows a similar trend. It is important to note that there is a similar drop of the yield ($dN/d\eta$) in the bin $\eta \sim -3.95$ as well as $\eta \sim -2.95$ attributed to the detector acceptance. In the LHC11e

period the dipole magnet current was inverted from negative to positive, which shows the dependence on the polarity of the magnet in the number of reconstructed muon tracks.

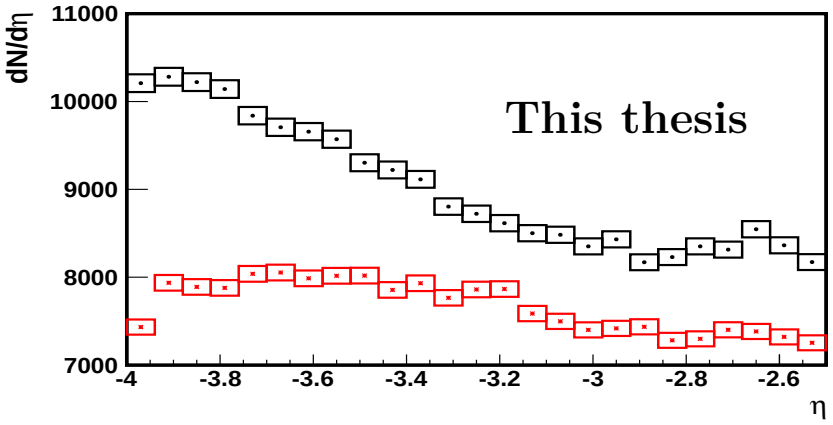

(a)

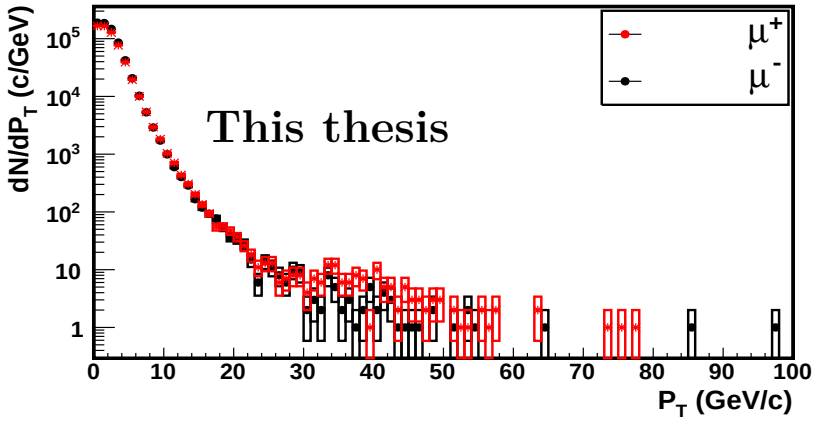

(b)

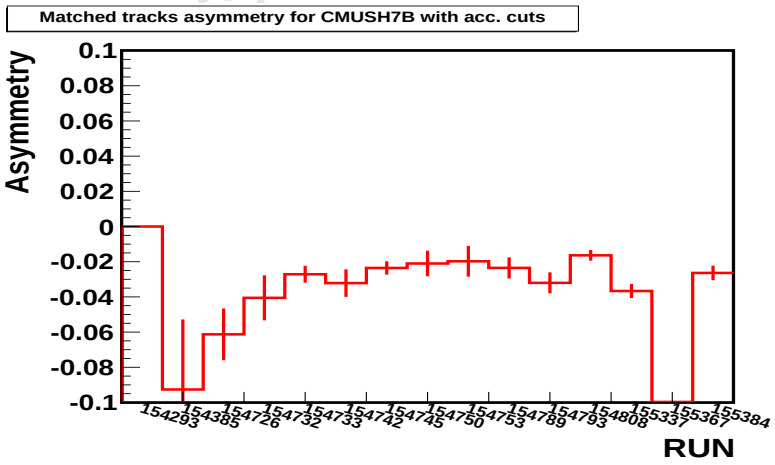

(c)

Figure 4.6: (a) η and (b) P_T distribution of positive and negative muon tracks passing standards cuts and the high momentum trigger threshold obtained from pp collisions at 7 TeV for period LHC11c and (c) is the charge asymmetry in the track reconstruction per run taken from the Muon QA [MuoQA] in this period. The boxes (rectangles) represent the statistical error.

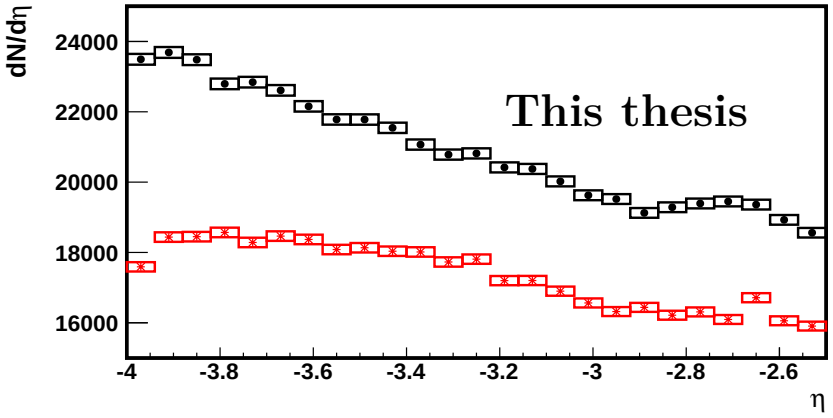

(a)

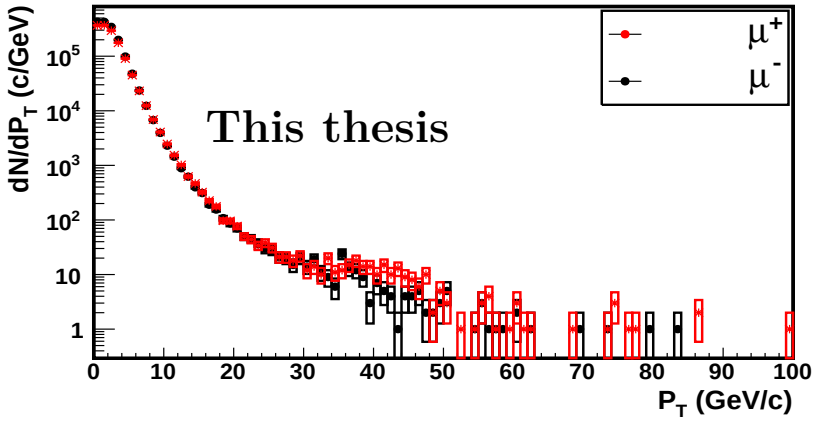

(b)

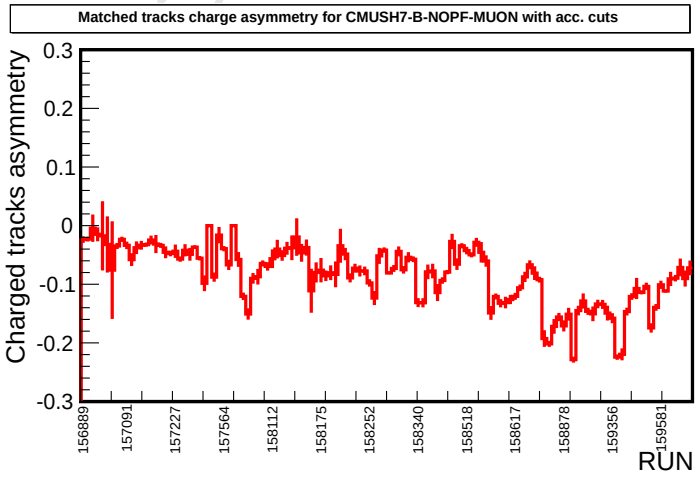

(c)

Figure 4.7: (a) η and (b) P_T distribution of positive and negative muon tracks passing standards cuts and the high momentum trigger threshold obtained from pp collisions at 7 TeV for period LHC11d and (c) is the charge asymmetry in the track reconstruction per run taken from the Muon QA [MuoQA] in this period. The boxes (rectangles) represent the statistical error.

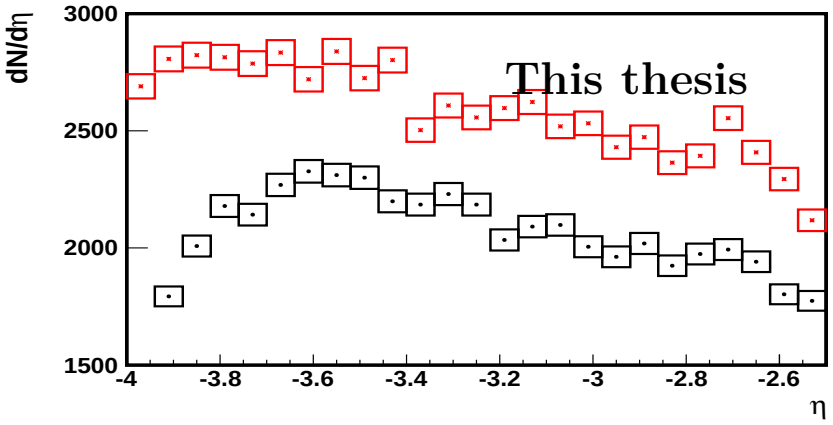

(a)

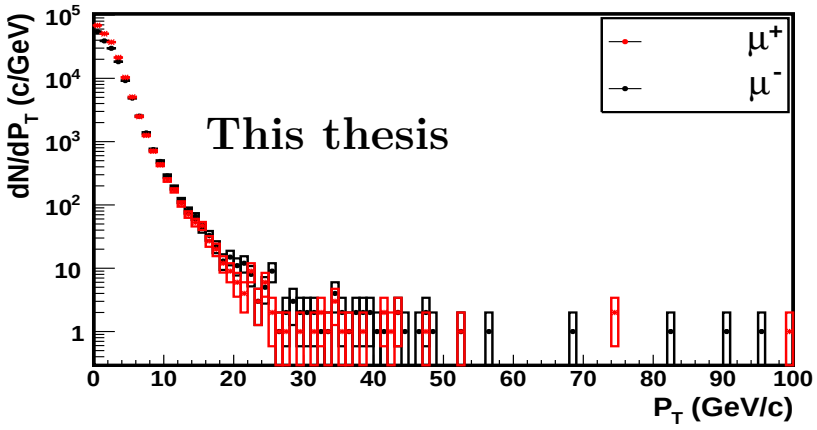

(b)

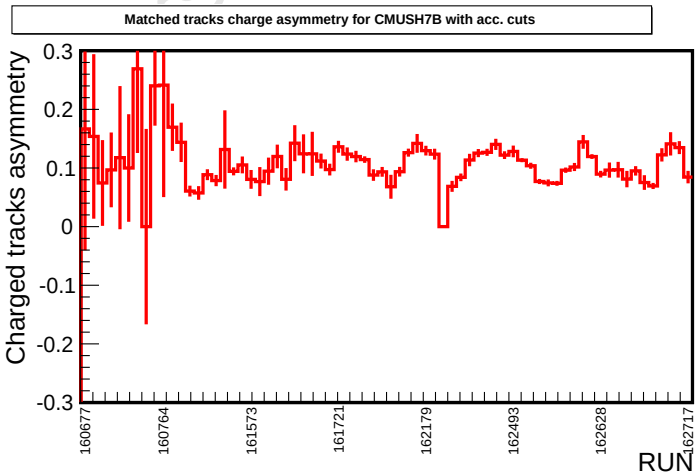

(c)

Figure 4.8: (a) η and (b) P_T distribution of positive and negative muon tracks passing standards cuts and the high momentum trigger threshold obtained from pp collisions at 7 TeV for period LHC11e and (c) is the charge asymmetry in the track reconstruction per run taken from the Muon QA [MuoQA] in this period. The boxes (rectangles) represent the statistical error.

4.4.3 Ratio of positive and negative muons ($\frac{\mu^+}{\mu^-}$)

In order to investigate the charge asymmetry in the production of high momentum muons the ratio of positive to negative muon yield against transverse momentum is computed and plotted in Figure 4.9 below. In Figure 4.9(a) is the ratio of positive to negative muons, and in Figure 4.9(b) is the zoomed in area (magnified region) between $P_T \sim 0$ - 40 GeV/c of Figure 4.9(a) whereas in Figure 4.9(c) is ratio of positive to negative muons from the fast simulation of single muon sources obtained from the Performance Study [dVa07]. In the P_T region (P_T <6 GeV/c) the ratio of LHC11c and LHC11d increases from 0.875 to unity whereas the ratio for LHC11e is above unity (1.25 to 1.30) in the P_T bin 0.5 GeV to 2.0 GeV/c but then decreases to unity from P_T =2 GeV/c to P_T =6 GeV/c as seen in Figure 4.9(b). In the region $6 < P_T < 15$ GeV/c the ratio of LHC11c and LHC11d goes above unity (averaged at ∼1.05) whereas for LHC11e the ratio drops below unity (averaged at ∼0.9) in this region. Beyond P_T =15 GeV/c (P_T >15 GeV/c) the consistent trend between LHC11c and LHC11d is not seen because of the large statistical fluctuations for all the three periods thus no conclusions can be drawn about the charge asymmetry in this region. Comparing the ratios in Figure 4.9(b) with the one from the Performance Study [dVa07] in Figure 4.9(c) it is evident that only the distribution of LHC11e is qualitatively in agreement with the ratio from the Performance Study [dVa07] in the region $P_T < 15$ GeV/c. The increase in the ratio above unity seen in Figure 4.9(c) in the region above P_T =20 GeV/c is not seen in all the three periods. The difference between the distributions in Figure 4.9(b) and 4.9(c) might be attributed to the difference in center of mass energy of proton-proton collisions.

The ratios in Figure 4.9 do not provide enough evidence to make conclusive statements about charge asymmetry due to limited statistics in the region above $P_T = 30$ GeV/c . The small bump seen between 30 GeV/c< P_T <50 GeV/c in the 2011 proton-proton experimental data presented above led to the simulation of the pure $W^{\pm}$ signal at 8 TeV to investigate the feasibility of measuring $W^{\pm}$, and to estimate how many $W^{\pm} \rightarrow \mu^{\pm} + \nu_{\mu^+}(\bar{\nu}_{\mu^-})$ events can be achieved in this P_T region of interest given the LHC luminosity at the ALICE interaction point in 2012 pp data taking period at 8 TeV.

In the next Chapter an introduction to event generation is presented, and then the focus is shifted to the event generator used in producing the $W^{\pm}$ boson pure signal. Then the signal extraction is presented in two cases, namely the ideal case and the realistic case to make a qualitative estimate of what the distribution of muons from $W^{\pm}$ would look like.

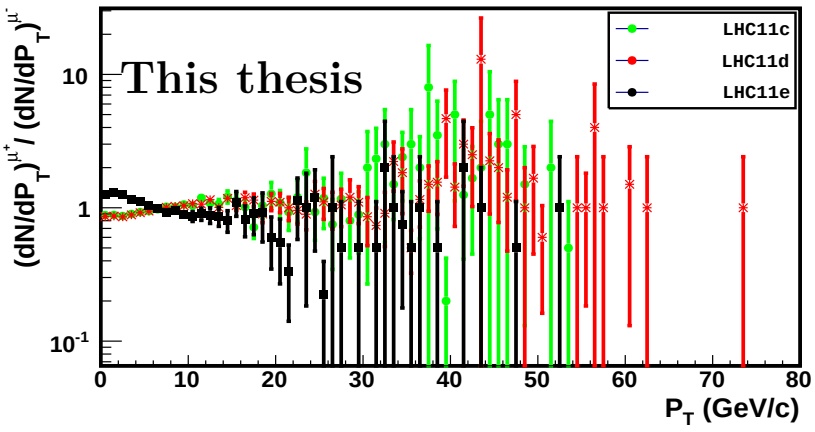

(a)

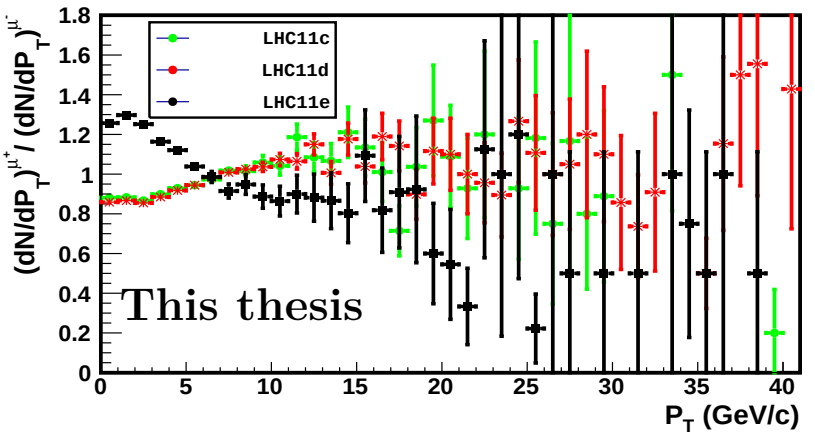

(b)

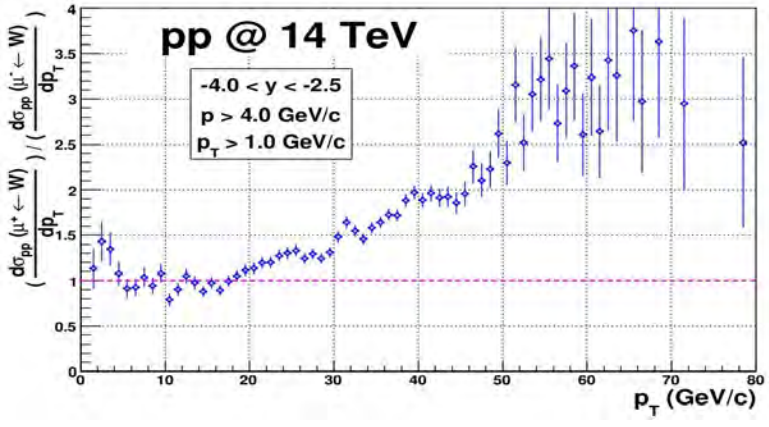

(c)

Figure 4.9: The ratio of positive to negative muon yield (a) for the three periods LHC11c, LHC11d and LHC11e, (b) is the zoomed in plot of (a) between 0 - 40 GeV/c and (c) from the Performance Study [dVa07] where a fast simulation of pp collisions at 14 TeV was done and single muon contributions were extracted.

Chapter 5

Simulation

In this Chapter we describe the simulation of $W^{\pm}$, reconstruction and extraction of the signal using the ALICE offline framework. The first sections describe the general event generation and reconstruction and the others focus on the pure signal generation of $W^{\pm}$.

5.1 Event Generation

Monte Carlo event generators exploit the probabilistic property of quantum mechanics to predict multiple particle event configuration of high energy physics. Pseudo–random number generators (using algorithms) are used to generate events and calculate cross-sections. Monte Carlo generators use numerical methods for estimating integrals based on "random" evaluations of the integrand. Integral over probability functions used are converted to simulation of a physical process.

In high energy physics collisions of particles produce an avalanche of particles in the final state leading to complexity in analyzing and sometimes disentangling events. For example a charm quark can directly decay into a muon ($c \rightarrow \mu + X$) however a bottom quark can indirectly decay into a muon via a charm decay ($b \rightarrow c + X \rightarrow \mu + \grave{X}$) resulting in difficulty in disentangling the two in analysis of the experimental data. Different generators − global (HERWIG, PYTHIA, etc.) and specialized (DPMJET, etc.) exist [Hri00]. The aim of an event generator is to provide an accurate as possible a representation of the event properties in a wide range of reactions, within and beyond the Standard Model, with emphasis on those where strong interactions play a role directly or indirectly, and therefore multi–hadronic final states are produced [Sjo06]. The programs of event generators are based on analytical results and models to mimic actual experiments. So events generation is tuned according to results from previous experiments. The LHC Monte Carlo generators are parameterized to Collider Detector at Fermilab (CDF) data [Mre09, Car04] to avoid model dependency. To mimic the reaction of the colliding system the internal structure of interacting particles must be understood. Parton distribution functions (PDF) are used to describe the structure and the interaction of the colliding particles. A PDF, $f_i(x, Q^2)$, gives the probability of finding a parton with a fraction x of the momentum of the beam particle when probed at Q^2 (Q is the momentum transfer) [Nav10]. So the interaction of the colliding particle is dependent on the momentum of the exchange particle (a photon, pomeron, etc).

Interactions can be classified as elastic and inelastic scattering, these processes are further subdivided. Elastic scattering is characterized by an exchange of glueball-like Pomeron (a postulated field carrier in Regge theory) between two interacting color singlets which leaves the incoming and the out-going particle intact whereas inelastic scattering is characterized by diffraction that is the final state is not the same as the initial state. In single diffraction only one of the incoming particle disintegrate, whereas in double diffraction both incoming particle disintegrate. In central diffraction two exchanged Pomerons interact leading to a particle shower and in non-diffraction exchange of color charges leads to a particle avalanche. All these interactions are included in the PYTHIA [Sjo06] program together with Bose-Einstein interaction and other processes.

5.1.1 PYTHIA event generator

PYTHIA 6.4.21 [Sjo06] (Perugia-0 tune [Ska10]) physics includes processes such as hard sub-processes, initial- and final-state parton showers, underlying events and beam remnants, fragmentation/hadronization, Beyond the Standard Model physics, Deep Inelastic Scattering and photon physics and decays, and other topics. The hard–processes which is our interest in PYTHIA include over 300 different hard–processes ($2 \rightarrow 1$ *e.g.* $f_i\bar{f}_j \rightarrow W^+, 2 \rightarrow 2$ and $2 \rightarrow 3$). It uses perturbative quantum chromodynamics for both low and high p_T regions and the Regge theory to calculate the total cross–section. PYTHIA uses the CTEQ5L [Cte96] (one of the recent PDFs) as a default PDF [Sjo06, Gui04, Nav10].

The total cross–section for proton-proton collision σ_{tot}^{pp} is calculated using the Regge theory according to the sum of powers [Gui04].

The cross section for a process, e.g. a $2 \rightarrow 1$ ($f_i\bar{f}_j \rightarrow W^+W^-$) process ($ij \rightarrow k$) is given by:

$$\sigma_{ij} = \int dx_1 \int dx_2 f_i^1(x_1, Q^2) f_j^2(x_2, Q^2) \hat{\sigma}_{ij\rightarrow k} \tag{5.1}$$

where $\hat{\sigma}_{ij\rightarrow k}$ is the cross section of the hard partonic process and $f_i^a(x_a)$ denotes parton distribution functions which describe the probability that a parton i inside a beam particle a carries a fraction of momentum x. Parton distribution functions also depend on the momentum transfer Q^2 of the hard process. Different PDFs are included in AliROOT [ALI13]. External event generators and detector simulation codes are interfaced with AliROOT using the `AliSimulation` class [Hri00]. All these processes are described in this `AliSimulation` class to produce particles which are to be transported through the detector materials to mimic tracks from real events. The particle transport is described in the following section.

5.1.2 Particle Transport

Event generators are used to produce or mimic real physics interactions, but the final state particles have to be transported through a detector to produce signals. The detector geometry and efficiency is then simulated with transport codes, e.g. GEANT3 [Apo94] or FLUKA [Fer05]. The transport codes include the precise description of the detector geometry and the material properties. ALICE detector geometry is described using the GEANT3 [Apo94] which is interfaced to AliROOT using a `TGeant3` class. An event simulation starts with an event generation followed by particle transportation. The particle traversing this simulated detector produces hits (energy deposition)

which correspond to track candidates, track segments and reconstructed space points in a real event. In Monte Carlo this is followed by summable digits (response), digits and data. After creation of digits, the reconstruction and analysis chain can be activated to evaluate the software and detector performance and to study some particular signatures [Hri00]. Creation of tracks from digits is called reconstruction.

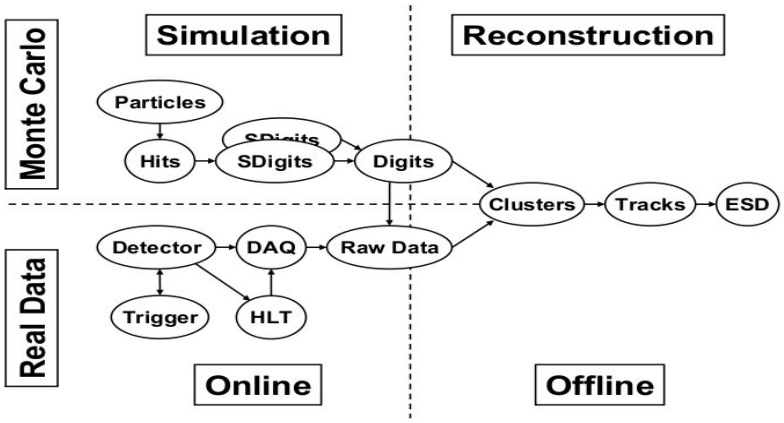

Figure 5.1: Reconstruction framework [Hri00].

Track Reconstruction

In Pb–Pb collisions at the LHC the charged particle multiplicity may vary from 1400 to 8000 particles in the central unit of rapidity at the nominal 2.76 TeV/nucleon. In 2010 PbPb data taking period at 2.76 TeV center of mass energy ALICE measured the charged-particle at mid-rapidity to be 1584±4(statistical error)±76(systematic error) [Aam10]. This poses a great challenge on reconstruction and analysis algorithms thus requiring predictive and precise simulation of the detector response. The particles traversing the detector produce hits which are looped over for each event to create summable digits then digits which are inputs to the reconstruction framework to create clusters. Then the vertex and tracks are reconstructed and particles are identified. The output of track reconstruction is the Event Summary Data (ESD) [Hri00]. This process of reconstruction is shown in Figure 5.1.

The ALICE reconstruction software uses the Kalman filter for local track finding which uses statistical estimations and predictions. Track recognition and fitting is done simultaneously and there is the possibility to reject space points on the fly and to extrapolate a track from one detector to another. In ALICE a good track–finding efficiency and reconstruction for tracks down to $p_T = 100\,\mathrm{MeV/c}$ is required [Hri00] for particle identification studies.

In simulations the reconstruction can be done with an ideal detector and/or by utilizing realistic detector working conditions. In an ideal case we assume a perfect detector i.e. no dead channels or misaligned detector modules. A realistic detector is exposed to working conditions thus effects of alignment and dead channels are common. Dead channels are electronic channels which are not working or not recording data. The effects of misalignment in the detector may affect the momentum resolution

of the detector thus leading to the effects like mis-assignment of momentum. The misalignment of the detector may come as effect of the magnet field, so a previously aligned detector may change when the field is turn on. So this in addition to the dead channels, polarity of the dipole, and other factors goes into the configuration files which are saved and later can be used in the Monte Carlo to reconstruct tracks per run in order to make a comparison with the data (in that period).

5.2 Pure $W^{\pm}$ boson signal simulation with PYTHIA in the ALICE muon spectrometer

A pure $W^{\pm}$ boson signal was generated with the PYTHIA 6.4.21 (Perugia-0 tune [Ska10]) [Sjo06] event generator for each minimum bias event in the AliROOT (version 5.4.16-AN) framework. A pure signal meaning only events involving a $W^{\pm}$ boson (kPyW process) was generated using protons as colliding particles at center of mass energy $\sqrt{s} = 8\,\text{TeV}$ and also taking into account *CTEQ5L* [Cte96, Lai00] parton distribution function. For the decay process $W^{\pm}$ was forced to decay directly to a muon using kWToMuon ($W^{\pm} \rightarrow \mu^{\pm} + \nu_{\mu^+}(\bar{\nu}_{\mu^-})$). In this case only muons were reconstructed in the spectrometer acceptance which takes into account the following geometrical cuts (standard cuts):

- eta cut $-4.0 \leq \eta \leq -2.5$, where $\eta = -\ln[\tan\frac{\theta}{2}]$ which is dependent on the azimuthal angle $\theta\ \epsilon\ (171°, 178°)$.
- phi which covers a range $\phi\ \epsilon\ (0°, 360°)$.

Below is an example of a configuration file used in the simulation the complete file is in Appendix II.

```
#include "PYTHIA6/AliDecayerPythia.h"
#include "PYTHIA6/AliGenPythia.h"
 //

void Config(){

    //
    AliGenPythia *gener = new AliGenPythia(1);
     gener.SetProcess(kPyW);
     gener.SetStrucFunc(kCTEQ5L);
     gener.SetEnergyCMS(8000.);
     //
     gener.SetForceDecay(kWToMuon);
    //


}
```

For this case hits were created only for the muon spectrometer using the macro given below. The number of events is set to $5000 \times (500 files)$ to satisfy the required integrated luminosity which can be calculated from the cross-section according to the equation below from [Fri04]:

$$\sigma^{W}_{exp} = \frac{1}{BR(W \rightarrow \mu\nu)} \frac{1}{A \times \epsilon} \frac{N_{events}}{\int \mathcal{L} dt}, \tag{5.2}$$

where σ^{W}_{exp} is the $W^{\pm}$ formation cross- section, $BR(W \rightarrow \mu\nu)$ is the $W^{\pm}$ branching ratio, A is the acceptance of the spectrometer, ϵ is the efficiency of the spectrometer, $\int \mathcal{L} dt$ is the integrated luminosity and N_{events} is the number of events. $A \times \epsilon$ is computed by the ratio of reconstructed tracks over generated tracks.

```
   void sim(Int_t nev=5000){

      AliSimulation simulator;
      simulator.SetTriggerConfig("MUON");
      simulator.SetMakeSDigits("MUON");
      simulator.SetMakeDigits("MUON");
      simulator.SetMakeDigitsFromHits("");
      simulator.SetRunQA("MUON:ALL");
           //
      simulator.Run(nev);

}
```

Hits created by the above macro (full macro in Appendix II) were then used as an input to the reconstruction framework to create muon tracks. This reconstruction of tracks was done using different detector conditions: the ideal conditions where the detector is at optimal efficiency (100%) and the realistic conditions where conditions of 2011 Pb-Pb data taking period (run number: 170309) were considered. The efficiency in this run was about 80%. Below is a sample of the macro used in reconstruction, the complete one is in Appendix II.

```
   void rec(){

       AliReconstruction reco;
       //
       reco.SetRunLocalReconstruction("MUON");
       reco.SetRunTracking("MUON");
       //
       reco.Run();

}
```

The signal was extracted after applying geometrical cuts ($-4.0 < \eta < -2.5$ and track polar angle at the end of the absorber, $171° < \theta_{abs} < 178°$) as well as by considering the correlation between the momentum (p) and the Distance of Closest

Approach (DCA) where DCA is the distance between the extrapolated muon track and the interaction vertex in the plane perpendicular to the beam axis containing the vertex, known as $\mathbf{p \times DCA}$. The $\mathbf{p \times DCA}$ reduces beam induced background whose $\mathbf{p \times DCA}$ distribution does not follow a Gaussian distribution. In addition, in order to select (trigger) all muon track the $\mathbf{A_{P_T}}$ cut ($P_T \geq 0.5\,\mathrm{GeV/c}$) is applied while high transverse momentum muons ($P_T \geq 4.0\,\mathrm{GeV/c}$) are triggered by applying the $\mathbf{H_{P_T}}$.

The following section shows the results obtained from simulation from the two detector cases after applying the above mentioned cuts.

5.3 Results

The results are presented in two sections, the first section presents the results of the ideal case and the second section presents the results of the realistic case. In each the P_T distributions and charge asymmetry are shown.

5.3.1 Ideal Case

P_T distributions

This analysis is based on the ESD data, which contains all information about particle kinematics. The ESD contains the information of the kinematic information (momentum, charge, mass, etc) and the PDG code which are codes used to identify particles produced in simulation. The transverse momentum distribution plots for this work are plotted in terms of a differential yield versus transverse momentum whereas the transverse momentum distribution plot from the Performance Study [dVa07] with which a comparison is made are in terms of the differential cross-section. Figure 5.2(a) shows the distributions of reconstructed positive and negative muon tracks from the ESD Tree with no cuts implemented. These reconstructed tracks are then subjected to standard geometrical, $\mathbf{p \times DCA}$ and the $\mathbf{A_{P_T}}$ cuts, and then required to come from the decay of W^+ and W^- into muons as shown in Figure 5.2(b). In Figure 5.3(a) the tracks from Figure 5.2(a) are required to pass the standard cuts, $\mathbf{p \times DCA}$ and the $\mathbf{H_{P_T}}$ as well to have come from the decay of W^+ and W^- to muons. W^+ and W^- are selected from the Monte Carlo tree by their corresponding PDG code, which is +24 and -24, respectively.

The shape or trend of the distributions are not altered in the region above the transverse momentum cuts, for both cases where $\mathbf{A_{P_T}}$ cut and $\mathbf{H_{P_T}}$ is applied as shown in Figures 5.2(b) and 5.3(a) respectively. The only effect is on the number of entries which are reduced after applying the cuts as seen in Table 5.1. It is evident that in the peak region, that is at $P_T \sim 40$ the shape of the distributions is not affected when the muon tracks are required to pass the cuts and correspond to a Monte Carlo particle ($W^{\pm}$). In all cases the number of entries of positive muons is larger than that of the negative muons as expected from the net proton-proton isospin which favors the production of W^+ as seen in Chapter 2, Figure 2.9.

In the case where the $\mathbf{A_{P_T}}$ cut is applied to tracks from the ESD Tree shown in Figure 5.2(b) in the P_T region below 2 GeV/c the number of entries is reduced compared to the case without cuts Figure 5.2(a). In the case where the tracks in Figure 5.2(a) are imposed to the $\mathbf{H_{P_T}}$ cut, that is in addition to the standard cuts and the $\mathbf{p \times DCA}$ cut almost all the entries in the region of P_T <2 GeV/c are removed. In

the $6 < P_T < 30$ GeV/c region the negative muon tracks dominate. This unexpected behavior seen in Figures 5.2(b) and 5.3(a) where the negative muons yield is larger than that of positive muons might be attributed to the detector configuration used in reconstruction. In both cases ($\mathbf{A_{P_T}}$ and $\mathbf{H_{P_T}}$), the yield of positive muons dominates that of negative muons in the region $P_T \gtrsim 30$ GeV/c.

In the indirect decay the first decay products will carry almost half the mass of $W^{\pm}$ as momentum (shown in Chapter 1 Table 1.1) and if these decay products further decay into muons they will most likely be emitted with $P_T \sim M_W/4$ and thus populate the 0 - 30 GeV/c P_T region. As expected the distributions are peaked at $P_T \sim 0.5 M_W = 40.$GeV/c. Comparing the positive and negative muon distributions in Figure 5.2(b) and 5.3(a) with the blue distribution in Figure 5.4(b) from the Performance Study [dVa07] it is evident that even at lower energy (8 TeV) it is possible to extract $W^{\pm}$. The distributions of muons from $W^{\pm}$ obtained from the Performance Study [dVa07] in Figure 5.5(b) is compared with Figure 5.3(a) plotted in linear scale shown in Figure 5.5(a). It should be noted that the comparison with the plots from the Performance Study [dVa07] is only qualitative since in this case the energy was different (14 TeV) and also the PDF (CTEQ4L) used in describing the proton, whereas for this study the energy is 8 TeV and the PDF is CTEQ5L [Cte96, Lai00]. The difference in the P_T region $6 < P_T < 30$ GeV/c in Figures 5.5(a) and 5.5(b) might be attributed to the reasons discussed above, and also the fact that in the Performance Study [dVa07] a fast simulation was performed (only just kinematics were generated, that is reconstruction of tracks through the detector was not performed), whereas in a simulation used in 5.5(a) the track reconstruction through the detector was performed. In order to make a reasonable comparison with the distribution of muons from $W^{\pm}$ shown in Figure 5.4(b) the combined distribution of both positive and negative muons from $W^{\pm}$ is also shown in Figure 5.4(a). A comparison between the two blue distributions in Figures 5.4(a) and 5.4(b) exhibit a qualitative similarity in the shape. A prominent bump is visible about the mean transverse momentum ($P_T(\mathrm{M_W}/2) = 40.0$ GeV/c) of primary decay muons from $W^{\pm}$. Shown in Figure 5.6 are distributions of muons per charge obtained by applying different momentum cuts. Figure 5.6(a) shows distributions of negative muons from the ESD Tree with no cuts (Blue), muons from W^- with $\mathbf{A_{P_T}}$ (Green) and muons from W^- with $\mathbf{H_{P_T}}$ (Red) applied whereas Figure 5.6(b) shows the same for the conjugate charge.

		Number of entries	
		ESD Tree (No Cuts)	**MC particle** ($W^{\pm} \to \mu^{\pm} + \nu_{\mu^+}(\bar{\nu}_{\mu^-})$)
$\mathbf{A_{P_T}}$	μ^+	180057	130133
	μ^-	134992	109845
$\mathbf{H_{P_T}}$	μ^+	180057	130059
	μ^-	134992	109653

Table 5.1: A table showing number of entries of positive and negative particle tracks from the ESD Tree before cuts, and whilst the tracks which pass the cuts are required to be muons from a Monte Carlo particle ($W^{\pm} \to \mu^{\pm} + \nu_{\mu^+}(\bar{\nu}_{\mu^-})$).

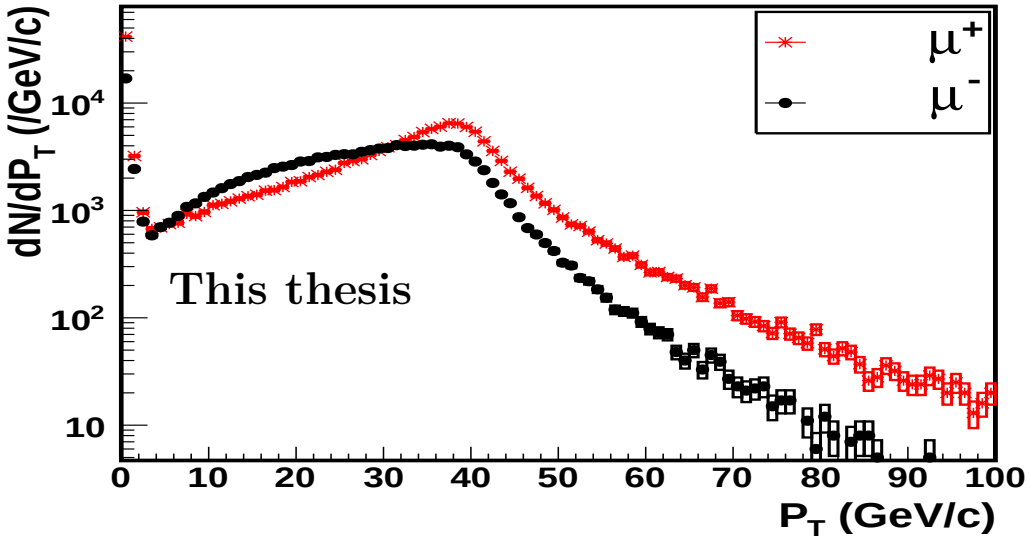

(a)

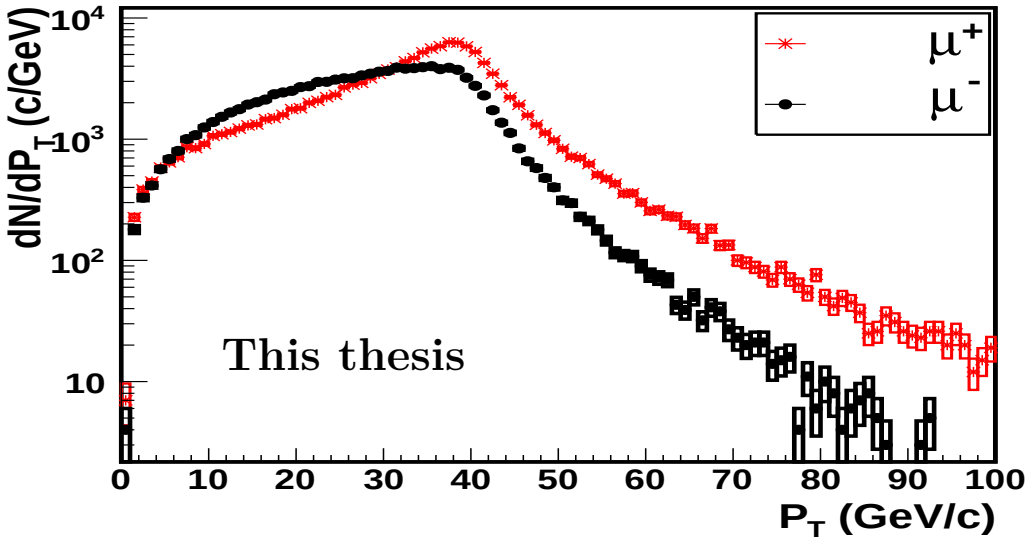

(b)

Figure 5.2: Transverse momentum distributions of (a) all reconstructed particle tracks from the ESD Tree with no cuts applied and (b) muon tracks from a Monte Carlo particle $W^{\pm} \rightarrow \mu^{\pm} + \nu_{\mu^+}(\bar{\nu}_{\mu^-})$ respectively with standard, $\mathbf{p \times DCA}$ and $\mathbf{A_{P_T}}$ matching trigger applied.

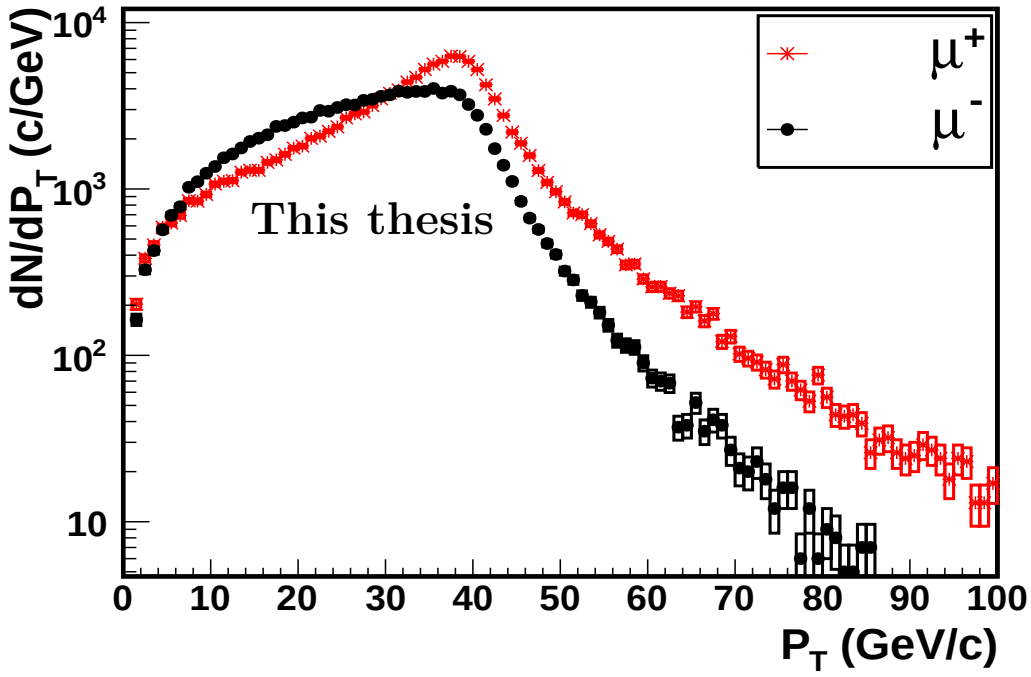

(a)

Figure 5.3: Transverse momentum distributions of (a) muon tracks from a Monte Carlo particle ($W^{\pm} \rightarrow \mu^{\pm} + \nu_{\mu^+}(\bar{\nu}_{\mu^-})$) with $\mathbf{H_{P_T}}$ cut applied in addition to standard cuts and $\mathbf{p \times DCA}$.

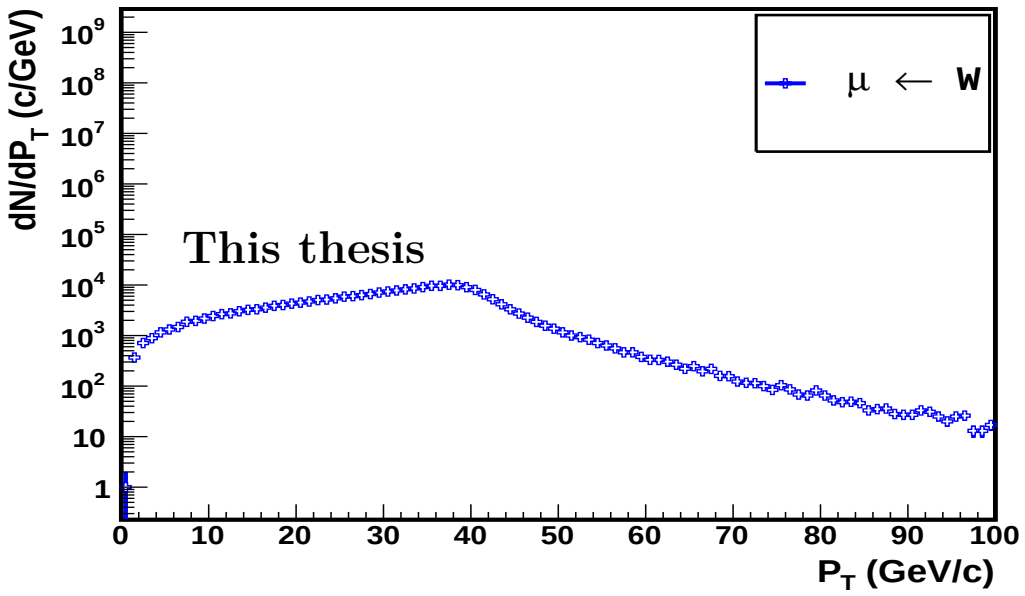

(a)

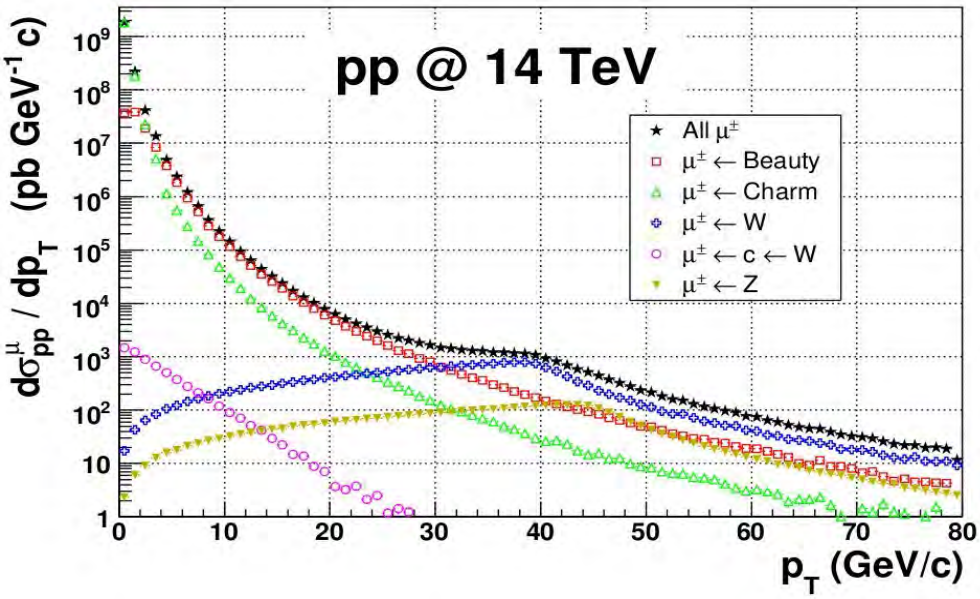

(b)

Figure 5.4: Shown in (a) is the combined spectrum of positive and negative muons from W^+ and W^- with the $\mathbf{H_{P_T}}$ cut applied in addition to standard cuts and the $p \times DCA$ cut. In (b) are transverse momentum distributions of muon tracks from all single muon contributions obtained from the Performance Study [dVa07] plotted as cross-section against P_T.

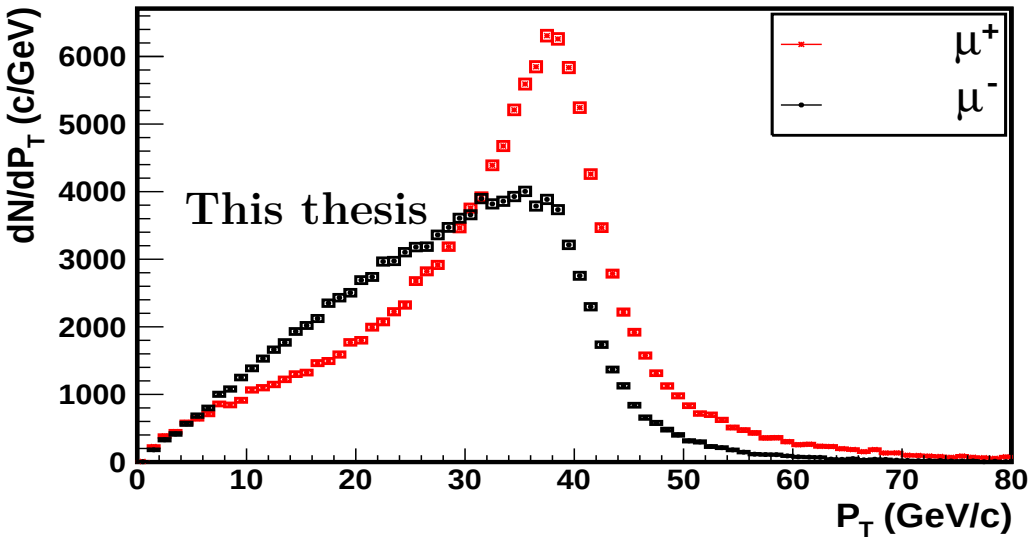

(a)

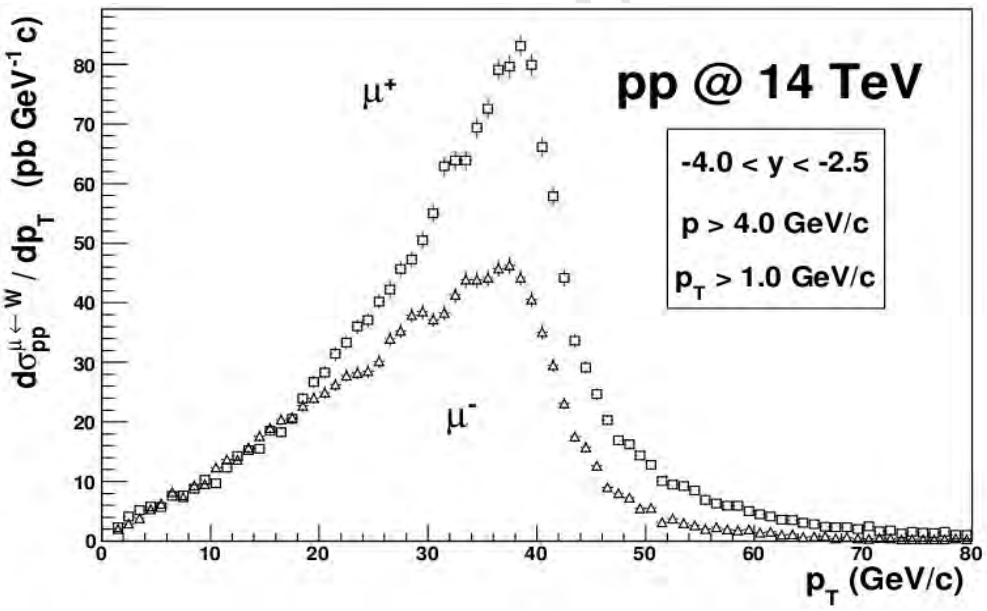

(b)

Figure 5.5: Shown in (a) are transverse momentum distributions from Figure 5.2(b) plotted in linear scale compared with (b) the production cross-section W^+ and W^- versus P_T at 14 TeV from the Performance Study [dVa07], the proton is described with CTEQ4L [Lai00] PDF. In (a) the generated tracks were reconstructed in the detector whereas in (b) only the kinematics were generated (this is no track reconstruction through the detector).

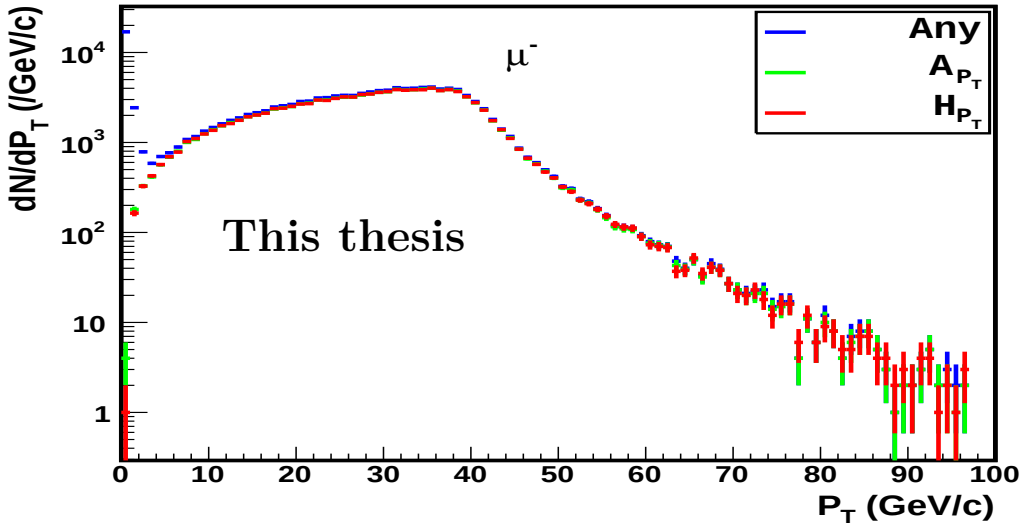

(a)

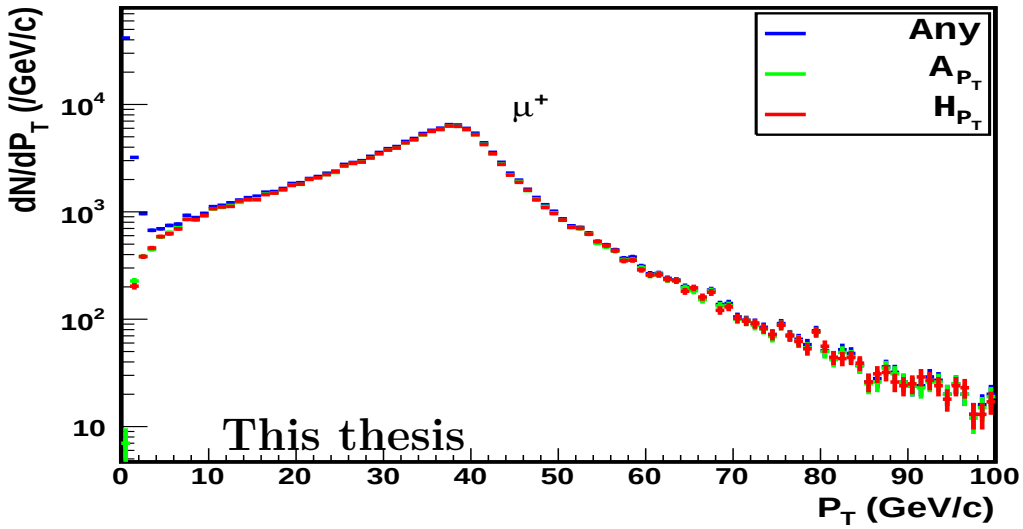

(b)

Figure 5.6: Effect of different transverse momentum cuts on the positive and negative muons. The blue distributions are of muon tracks from the ESD Tree with no cuts applied, in green are distributions of muons from $W^{\pm}$ with the $\mathbf{A_{P_T}}$ and in red are distributions of muons from $W^{\pm}$ with $\mathbf{H_{P_T}}$ applied.

Ratio of positive to negative muons (Charge asymmetry)

Unlike in other old experiments were electron-positron and proton-anti-proton collision were used for W boson study, the some of the recent experiments uses (also in this study) proton-proton collisions. The net charge of the colliding system in this case is not zero therefore the charge asymmetry in the formation of $W^{\pm}$ can be investigated. Figure 5.7(a) and Figure 5.7(b) show the ratio of positive to negative muon yield for the $\mathbf{A_{P_T}}$ and $\mathbf{H_{P_T}}$ cases obtained from the distributions in Figures 5.2(b) and 5.3(a). In the P_T region $4.0 \lesssim P_T \lesssim 30$ GeV/c the ratio is less than unity, and in the region ($P_T \gtrsim 30$ GeV/c) where the direct decay of $W^{\pm}$ is dominant the expected asymmetry is seen where the ratio goes above unity. Comparing the distributions in Figures 5.7(a) and 5.7(b) with the one in Figure 5.7(c) from the Performance Study [dVa07] it is evident that at low transverse momentum region P_T <4 GeV/c the distributions show a similar trend, whereas in the region $4 < P_T < 20$ GeV/c they are different, the distribution in Figure 5.7(c) is almost constant around unity and the ones in Figures 5.7(a) and 5.7(b) form a trough (dip) with a minimum at 0.6. Above $P_T = 20$ GeV/c the distribution in Figure 5.7(c) goes above unity exhibiting the charge asymmetry as expected, whereas in Figures 5.7(a) and 5.7(b) this happens at $P_T = 30$ GeV/c. From $P_T = 30$ GeV/c the ratio steadily increases with small uncertainty until $P_T = 60$ GeV/c and then the uncertainties increases in both Figure 5.7(a) and Figure 5.7(b), for Figure 5.7(c) this happens above $P_T = 50$ GeV/c. These differences between Figures 5.7(a) and 5.7(b) and the ratio from the Performance Study [dVa07] in Figure 5.7(c) can be due to the detector configuration.

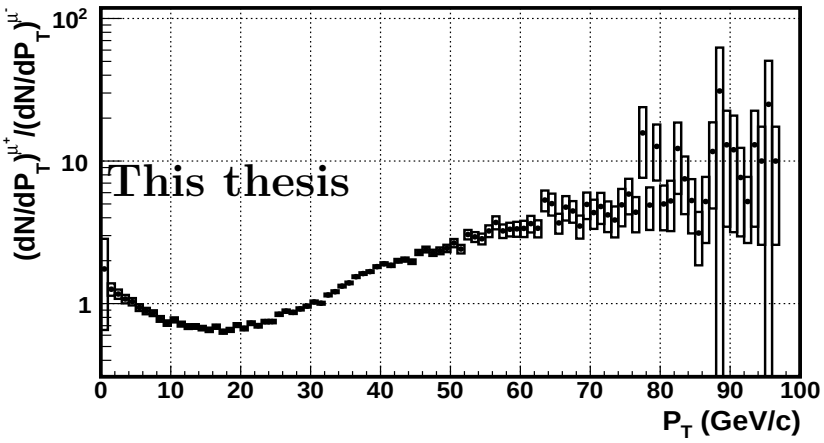

(a)

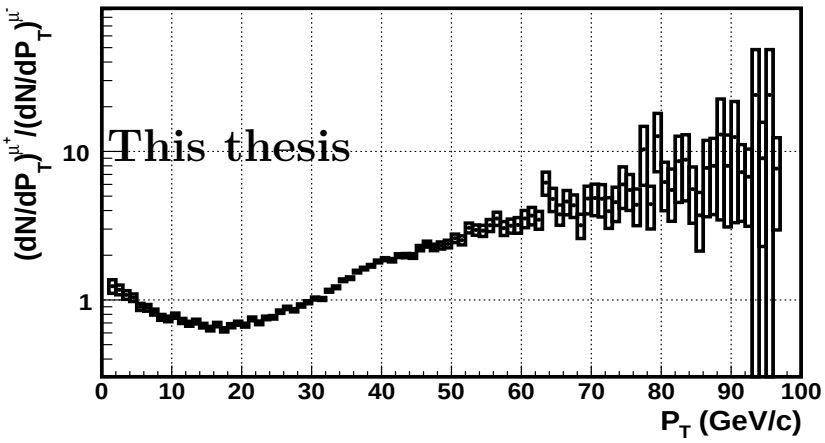

(b)

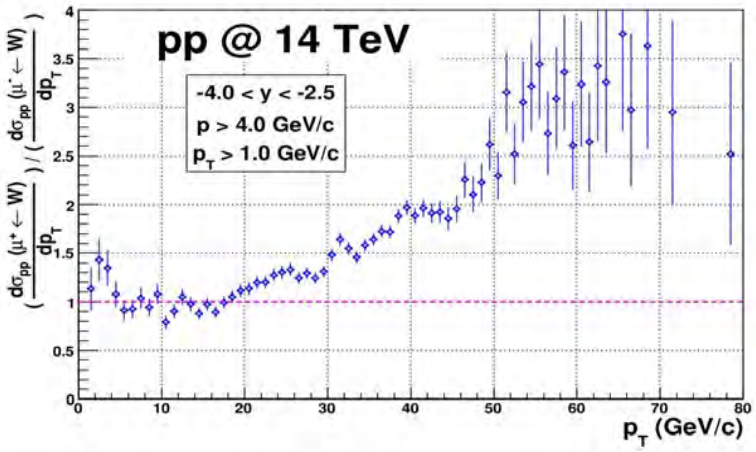

(c)

Figure 5.7: The ratio of positive to negative muon yields (a) with $\mathbf{A_{P_T}}$ and (b) $\mathbf{H_{P_T}}$ compared with the (c) ratio from the Performance Study [dVa07] in the Muon Spectrometer acceptance.

5.3.2 Realistic Case

P_T distributions

In this section we present the results obtained in the case of reconstruction with a realistic detector conditions of 2011 Pb-Pb data taking period from the OCDB. The analysis is based on the ESD data and the same strategy is followed as in the ideal case. Shown in Figure 5.8(a) is the distribution of all reconstructed negative and positive muon tracks from the ESD Tree with no cuts. In Figure 5.8(b) is the distribution obtained when tracks from the ESD Tree are required to pass standard cuts, $\mathbf{p \times DCA}$, the $\mathbf{A_{P_T}}$ transverse momentum cut and also correspond to muons to from the decay of W^+ and W^-, whereas in Figure 5.9(a) the $\mathbf{H_{P_T}}$ is applied in addition to the three cuts instead of the $\mathbf{A_{P_T}}$. The selection of $W^{\pm}$ and $\mu^{\pm}$ is done using their PDG code, mentioned in the ideal case. In order to make a reasonable comparison with the P_T distribution from the Performance Study [dVa07] a combined distribution of positive and negative muons is shown in Figure 5.10(a). Figure 5.10(b) from the Performance Study [dVa07] shows the different contributions to the single muon P_T distribution (black distribution), the blue distribution corresponds to the $W^{\pm}$ contribution. Figures 5.11(a) and 5.11(b) are the zoomed regions between 0 - 25 GeV/c and 38 - 52 GeV/c respectively. Also shown in this Section in Figure 5.12 are transverse momentum distributions of positive and negative muons with different P_T cut applied.

As in the ideal case, for this work the P_T distributions are shown in terms of the differential yield (dN/dP_T) against transverse momentum whereas in Figure 5.10(b) the yield is in terms of the differential cross-section. Table 5.2 shows the number entries of positive and negative muon tracks at different reconstruction level with different momentum cuts applied. The distributions of muon tracks (positive and negative) from ESD Tree in Figure 5.8(a) display a broader shape compared to those from the ideal case (see Figure 5.2(a)). Below $P_T \lesssim 6.0$ GeV/c the number of positive muon entries is larger than that of negative muons. In the transverse momentum region $6 \lesssim P_T \lesssim 20$ GeV/c and $P_T \gtrsim 44$ GeV/c the negative muons dominates as shown in the zoomed-in region between 0 - 25 GeV/c of Figure 5.9(a), which are shown in Figure 5.11(c) ($\mathbf{A_{P_T}}$) and Figure 5.11(d) ($\mathbf{H_{P_T}}$). The light gray shaded areas in Figures 5.11(c) and 5.11(d) shows the region where positive muon tracks are dominant.

This widened distribution in Figure 5.8(a) compared to the ideal case (Figure 5.2(a)) might be attributed to several issues with the detector, for example, dead channels and detector alignment. The effect of alignment was studied in more details in parallel analysis by Du Toit in his Master Thesis [DuT13]. Besides cutting or reducing the entries, the $\mathbf{A_{P_T}}$ and $\mathbf{H_{P_T}}$ cuts do not change the shape of the distribution of muon tracks from the Monte Carlo kinematic tree above this transverse momentum threshold as seen Figures 5.8(b) and 5.9(a). Shown in Figure 5.10(a) is the distribution of muons from $W^{\pm}$ with an $\mathbf{H_{P_T}}$ and $\mathbf{p \times DCA}$ cuts applied to the muon tracks in addition to the geometrical cuts. The broadening of the transverse momentum distribution is evident in Figure 5.10(a) compared to the distribution Figure 5.4(a), and also there is a prominent shift of the peak to the low transverse momentum part of the spectrum (around 32 GeV/c). This momentum shift suggests that there is a transverse momentum mis-assignment to the muon tracks, this is muon tracks with transverse momentum around $P_T = 40$ GeV/c are reconstructed as either low or high transverse momentum tracks. This mis-assignment of transverse momentum

		Number of entries	
		ESD Tree (No Cuts)	**MC particle** ($W^{\pm} \rightarrow \mu^{\pm} + \nu_{\mu^+}(\bar{\nu}_{\mu^-})$)
$\mathbf{A_{P_T}}$	μ^+	96989	91533
	μ^-	84048	78951
$\mathbf{H_{P_T}}$	μ^+	96989	85193
	μ^-	84048	72232

Table 5.2: A table showing number of entries of positive and negative particle tracks from the ESD Tree before cuts, and whilst the particle tracks are required to pass the cuts and be muons from a Monte Carlo particle($W^{\pm} \rightarrow \mu^{\pm} + \nu_{\mu^+}(\bar{\nu}_{\mu^-})$).

	Ideal Case	Realistic Case
N_{tracks} ($\mathbf{A_{P_T}}$)	239 978	170 484
N_{tracks} ($\mathbf{H_{P_T}}$)	239 712	157 425
% of $\mathbf{A_{P_T}}$ tracks rejected by $\mathbf{H_{P_T}}$cuts	0.0942	7.66

Table 5.3: Number of entries of muon tracks from $W^{\pm}$ with standard, $\mathbf{p} \times \mathbf{DCA}$ and $\mathbf{A_{P_T}}$ or $\mathbf{H_{P_T}}$ cuts applied for both ideal and realistic case. The percentage of the number of tracks rejected by cuts is also shown.

leads to a broadening of the transverse momentum distributions, this effect is more pronounced in P_T distribution of negative muons. Figures 5.8(b) and 5.9(a) plotted in a linear scale shown in Figures 5.11(c) and 5.11(d) respectively exhibit clearly this effect as well as the shift of the peak. There is a significant change in the behavior of the P_T distribution for the realistic case (Figures 5.11(c) and 5.11(d)) compared to the ideal case (see Figure 5.5(a)). This broadening of distributions shows the effect of the working detector configuration (detector conditions during data taking) in track reconstruction. This thus make the study of high transverse momentum single muons important in testing the detector performance. The distributions of transverse momentum for each muon charge are plotted in Figures 5.12(a) and 5.12(b) showing the effect of each transverse momentum cut on the distribution of the muon tracks. As illustrated by the red points in Figure 5.12 it is evident that the high transverse momentum cut ($\mathbf{H_{P_T}}$) does reduce the low transverse momentum tracks which dominates the single muon transverse momentum spectrum in experimental data (see Chapter 4).

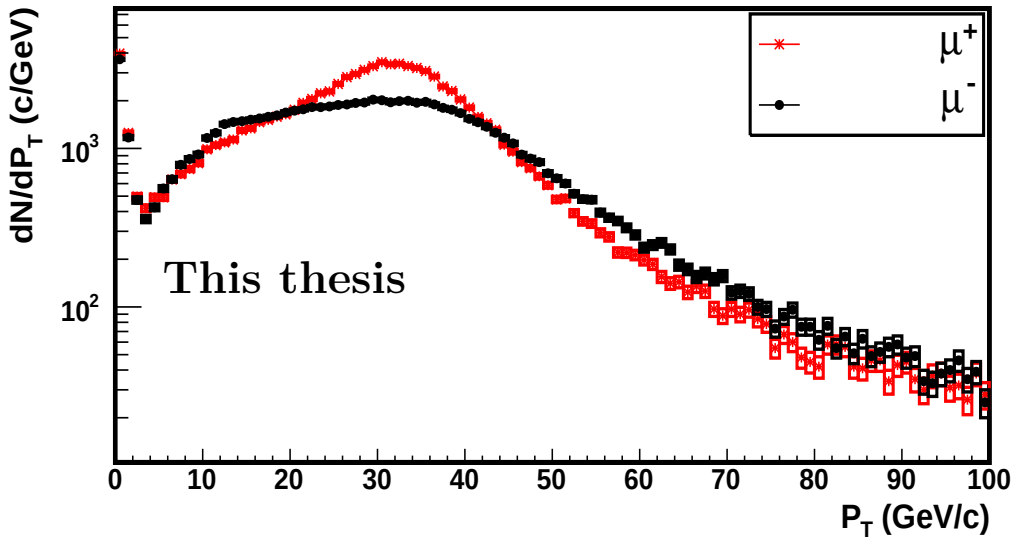

(a)

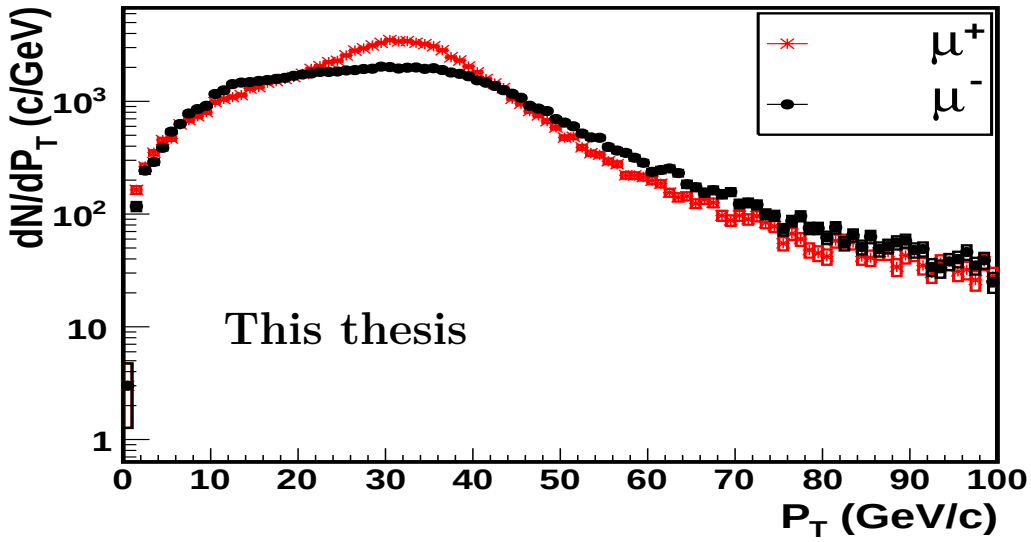

(b)

Figure 5.8: Transverse momentum distributions of (a) all reconstructed tracks with no cuts applied from the ESD Tree and (b) muon track distributions from a Monte Carlo particle ($W^{\pm} \rightarrow \mu^{\pm} + \nu_{\mu^+}(\bar{\nu}_{\mu^-})$) respectively with standard, $\mathbf{p \times DCA}$ and $\mathbf{A_{P_T}}$ matching trigger applied.

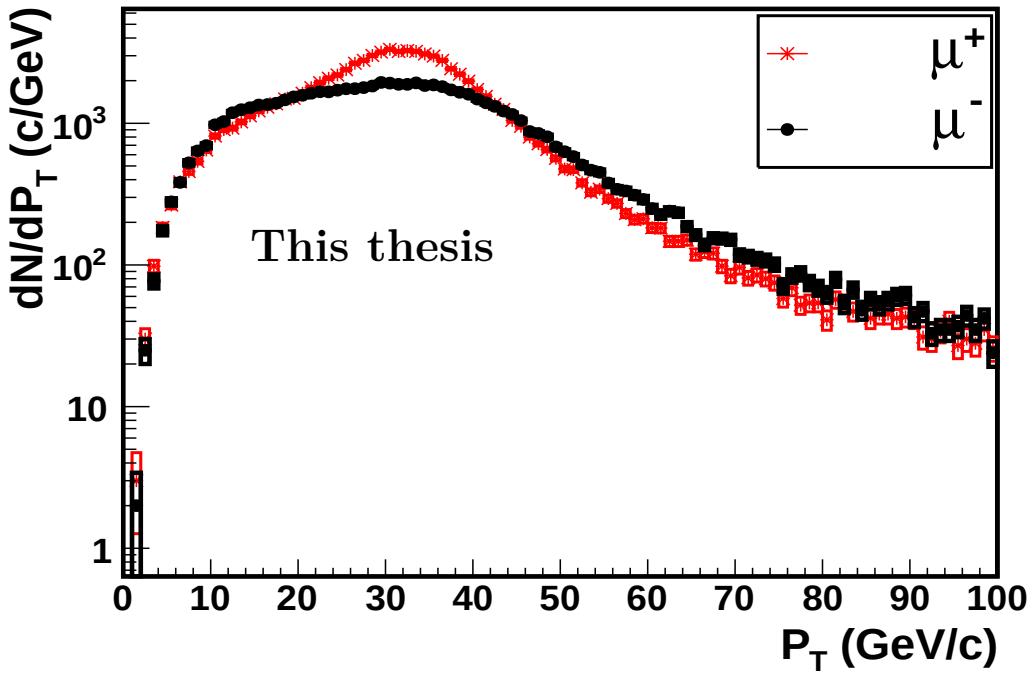

(a)

Figure 5.9: Transverse momentum distribution of (a) muon tracks from a Monte Carlo particle ($W^{\pm} \rightarrow \mu^{\pm} + \nu_{\mu^+}(\bar{\nu}_{\mu^-})$) with $\mathbf{H_{P_T}}$ cut applied in addition to standard cuts and $\mathbf{p} \times \mathbf{DCA}$.

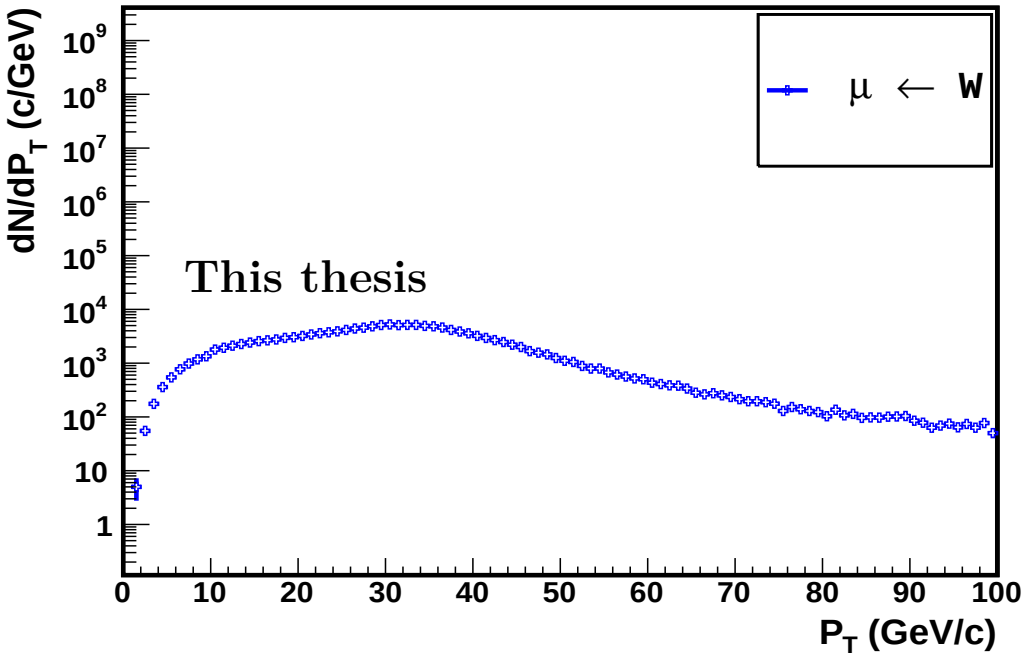

(a)

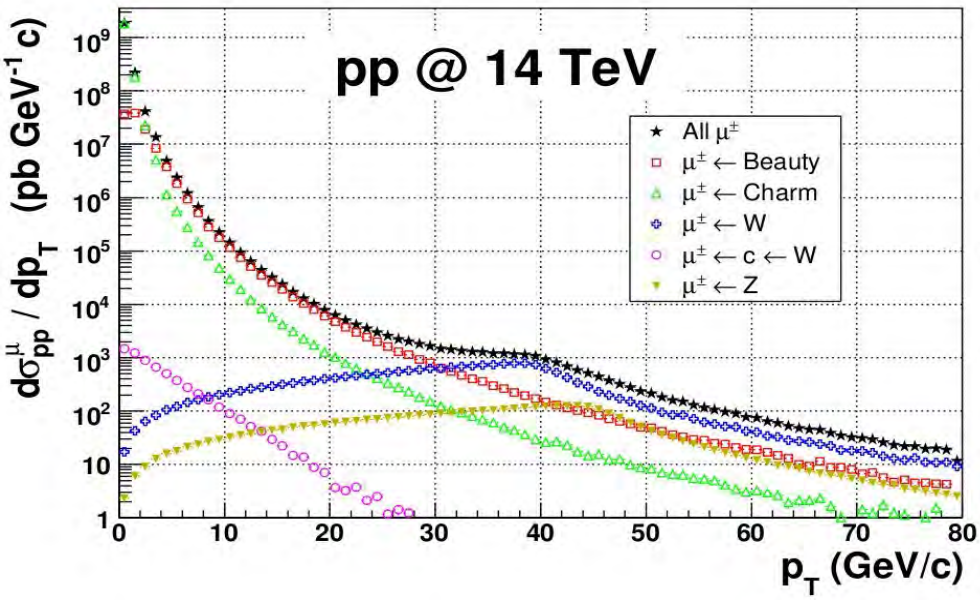

(b)

Figure 5.10: The plot in (a) show a combined momentum distribution of both positive and negative muons from W^+ and W^- with the $\mathbf{H_{P_T}}$ cut applied in addition to standard cuts and $\mathbf{p \times DCA}$ whereas in (b) are transverse momentum distributions of muon tracks from all single muon contributions obtained from the Performance Study [dVa07] plotted as differential cross-section against P_T.

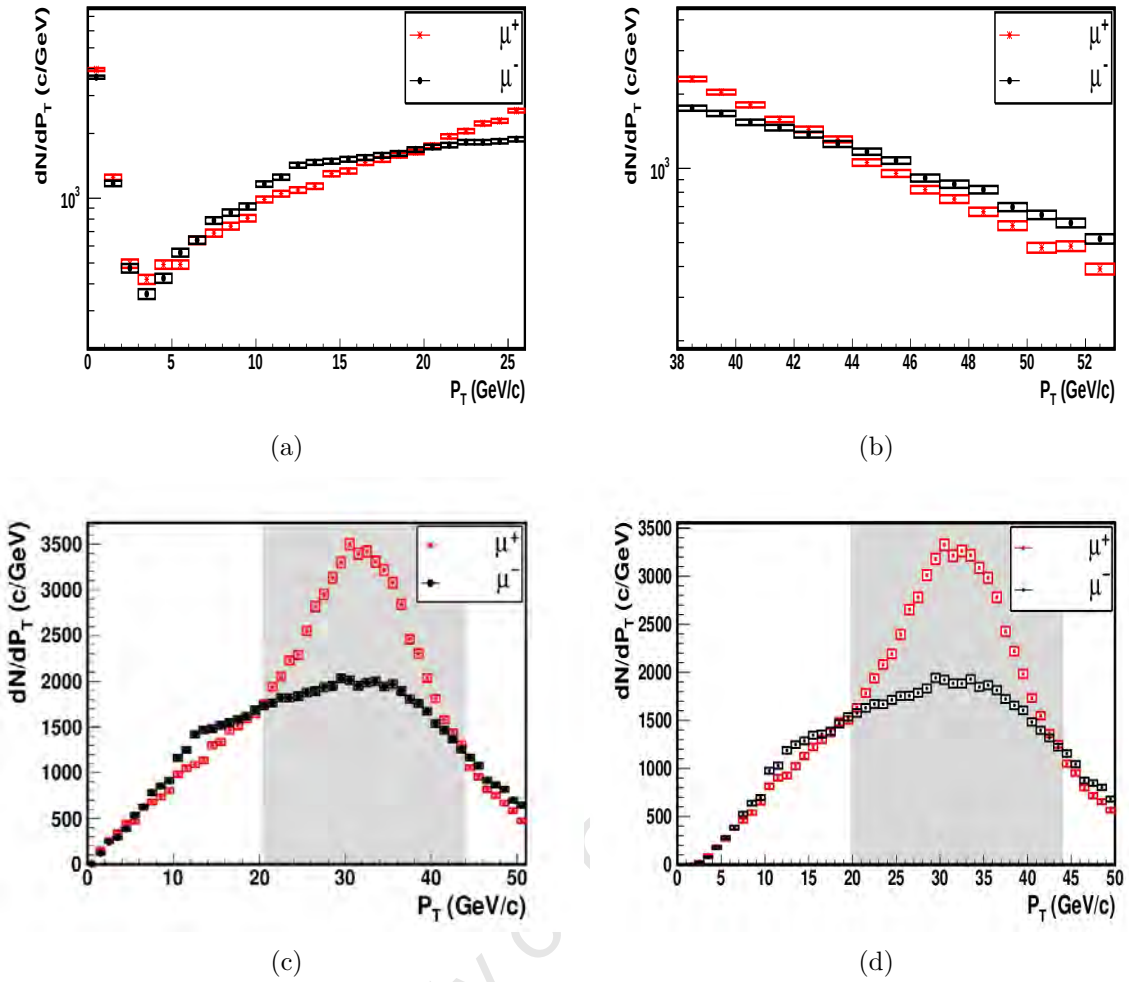

Figure 5.11: Transverse momentum distribution of all reconstructed tracks with no cuts applied, in this case the 0 - 25 GeV/c (a) and 38 - 52 GeV/c (b) is zoomed in. Transverse momentum distribution of reconstructed tracks from $W^{\pm}$ with (c) $\mathbf{A_{P_T}}$ and (d) $\mathbf{H_{P_T}}$ cut applied, in both cases the 0 - 50 GeV/c region is zoomed.

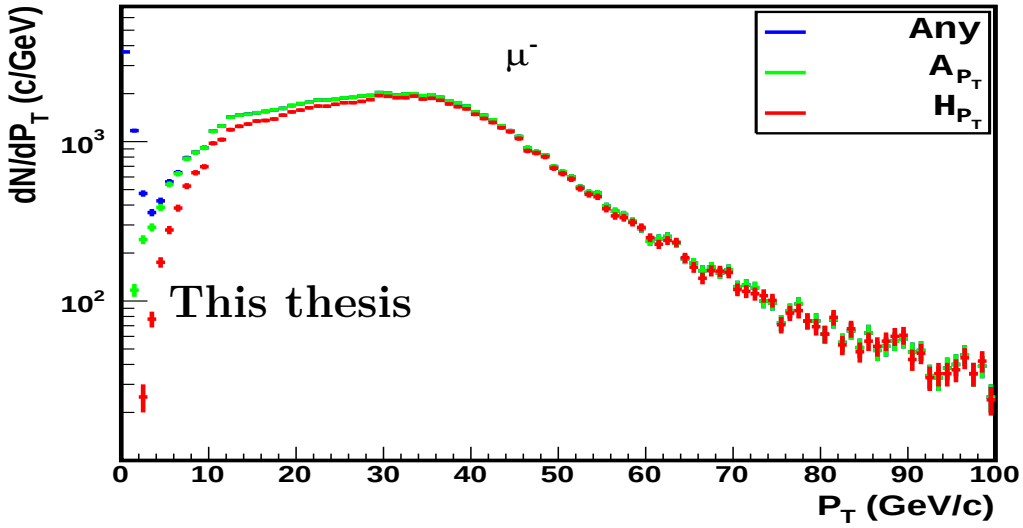

(a)

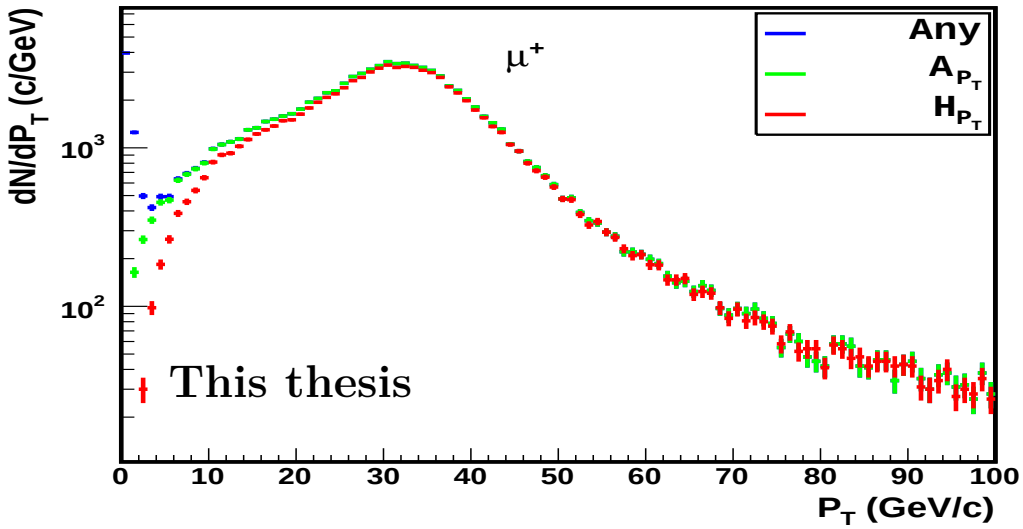

(b)

Figure 5.12: Effect of different transverse momentum cuts on the positive and negative muons. The blue distributions are of muon tracks from the ESD Tree with no cuts applied, in green are distributions of muons from $W^{\pm}$ with the $\mathbf{A_{P_T}}$ and in red are distributions of muons from $W^{\pm}$ with $\mathbf{H_{P_T}}$ applied.

Ratio of positive to negative muons (Charge asymmetry)

In this section we present the ratio of positive and negative muons for $\mathbf{A_{P_T}}$ and $\mathbf{H_{P_T}}$ and compare them to the ratios obtained in the ideal case as well as with the ratio taken from the Performance Study [dVa07].

In Figure 5.13(a) is the ratio obtained from the distributions in Figure 5.8(b), and in Figure 5.13(b) is the ratio obtained from the distributions in Figure 5.9(a). The ratio $(\frac{(dN/dP_T)^{\mu^+}}{(dN/dP_T)^{\mu^-}})$ is plotted against transverse momentum (P_T).

Below $P_T = 4$ GeV/c the ratio in Figure 5.13(a) increases from unity to 1.4, while above $P_T = 4$ GeV/c the ratio goes below unity it rises again at $P_T = 12$ GeV/c. In the region $20 < P_T < 30$ GeV/c the ratio increases above unity but then decrease above $P_T = 30$ GeV/c and reaches unity at $P_T = 44$ GeV/c, above this P_T the ratio goes below unity and then flattens around 0.8 above $P_T = 56$ GeV/c.

In Figure 5.13(b) the entry at $P_T = 1$ GeV/c is removed, again the ratio decreases from $P_T = 1$ GeV/c and goes below unity at $P_T = 4$ GeV/c and follow the same trend as the one in Figure 5.13(a). Not taking into account the region below $P_T = 1$ GeV/c the ratio in this case look similar. Comparing these ratios with the ones in the ideal case as well as the one from the Performance Study [dVa07] it is evident that the detector configuration affects the reconstruction of tracks. According to the ideal case, the charge asymmetry due to direct decays of $W^{\pm}$ is seen above $P_T = 30$ GeV/c, this is not seen this case. Comparing these ratios with the ratio from the Performance Study [dVa07] it is clear that in the three cases the ratio rise beyond unity at $P_T = 20$ GeV/c and reaches the ratio $\sim$1.5 at $P_T = 30$ GeV/c. In the P_T region above 30 GeV/c the ratio does not behave as per expectation from the Performance Study [dVa07] and the ratios obtained in the ideal case thus indicating a issues with the detector especially if one takes into account that above $P_T \geq 40$ more positive muons are expected to dominate due to isospin effects.

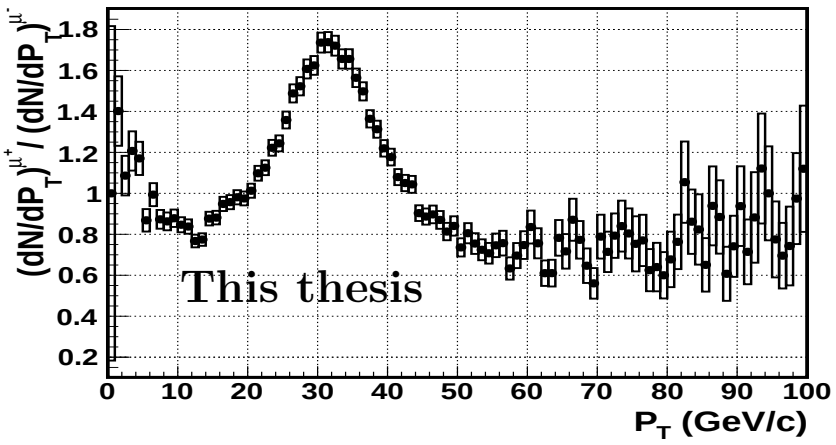

(a)

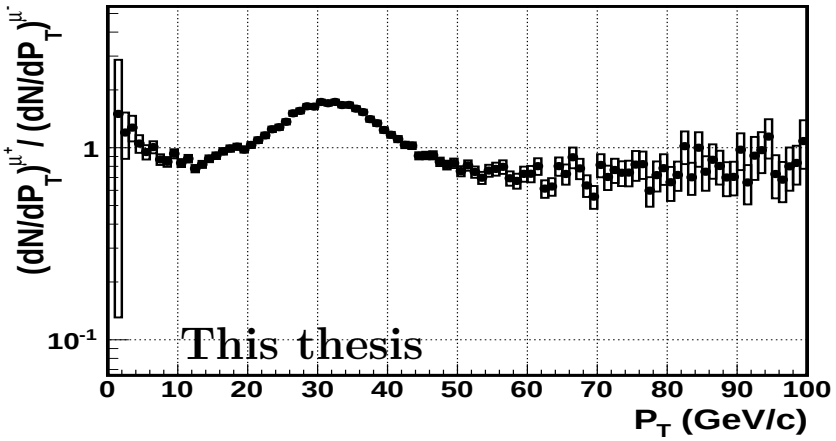

(b)

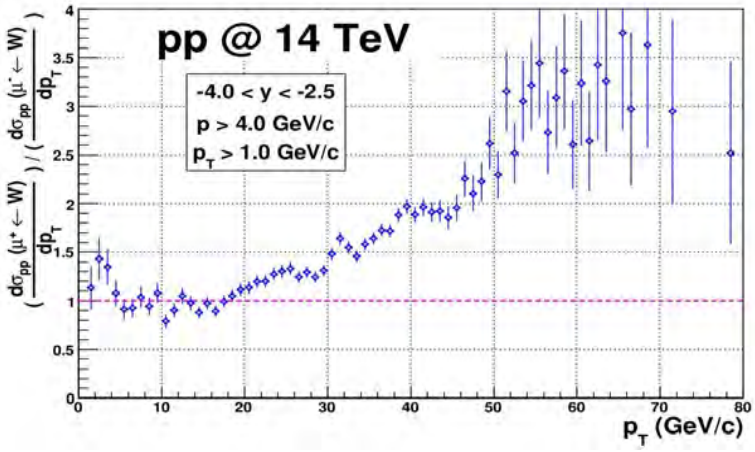

(c)

Figure 5.13: The ratio of positive to negative muon yields (a) with $\mathbf{A_{P_T}}$ and (b) $\mathbf{H_{P_T}}$ compared with the (c) ratio from the Performance Study [dVa07] in the Muon Spectrometer acceptance.

The results presented for the realistic case tell us that there are issues to be investigated about the state of the detector. Comparing the $\mathbf{H_{P_T}}$ plots for ideal and realistic case it is clear that the distributions in the realistic case are shifted to the left and show broader shapes. In the ideal case the positive and negative muon distributions are peaked at $P_T = 38$ GeV/c and $P_T = 36$ GeV/c respectively whereas in the realistic case they are peaked at $P_T = 31$ GeV/c and $P_T = 30$ GeV/c respectively. For example, there are about 6292 events of W^+ with $P_T = 38$ GeV/c in the ideal case whereas in the realistic case about 3327 events of W^+ are seen at the peak of the distribution. Of course these numbers are estimated by just adding up the number of events in these momentum bin with no estimate of the contribution of heavy flavour (charm and beauty) muons which will be a factor in the experimental data. To support the remarks made about the detector problems the acceptance times efficiency ($A \times \epsilon$) is plotted against transverse momentum and shown in Figure 5.14. The acceptance times efficiency plots in Figure 5.14 are compute for the case where the $\mathbf{H_{P_T}}$ and $\mathbf{p \times DCA}$ are used in addition to the standard geometrical cuts. In Figure 5.14(a) for the ideal case the capability to reconstruct positive and negative muons is almost the same and is consistent with 95%. For the realistic case shown in Figure 5.14(b) the capability to reconstruct negative muons at low P_T is underestimated whereas at high P_T is high, this is evident in the P_T distributions of the realistic case where the negative muons tend to dominate. This over-estimation of the capability is clear in Figure 5.14(c) at high P_T. In order to achieve or improve the statistics seen in the realistic case it is important that the detector conditions are investigated so that they can be taken into account in reconstructing the high momentum single muons in the 2012 data of proton-proton collisions at 8 TeV. The simulation suggests that given an ideal detector it is possible to extract $W^{\pm}$ at less than nominal energies (8 TeV) whereas with a realistic detector the configuration is to be better understood and conveniently taken into consideration.

In the following Chapter the summary and conclusion of the study are a presented.

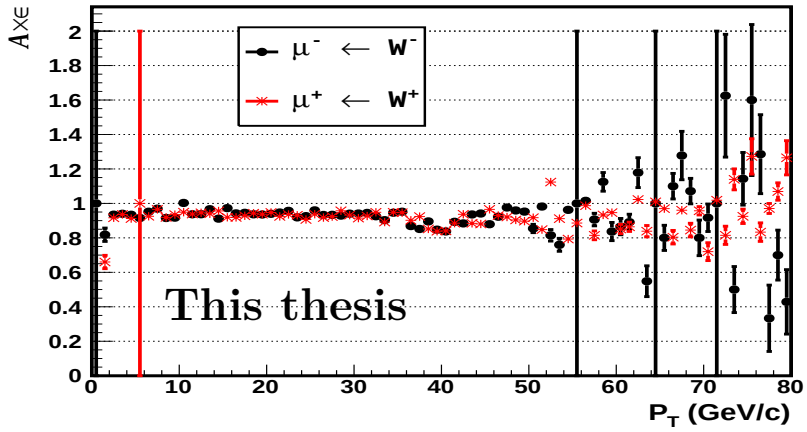

(a)

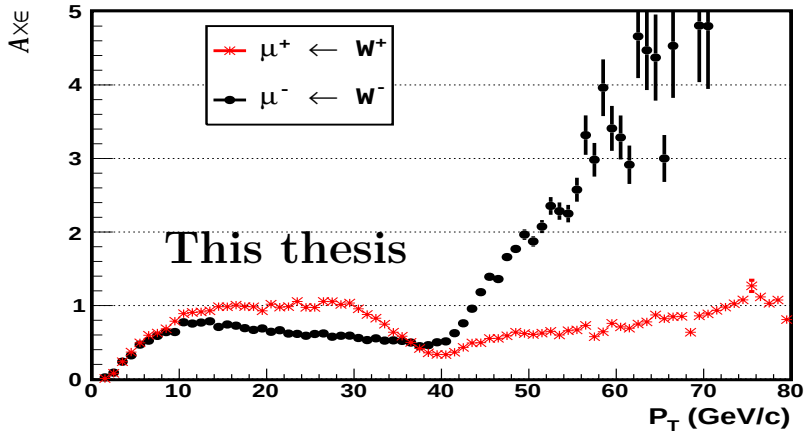

(b)

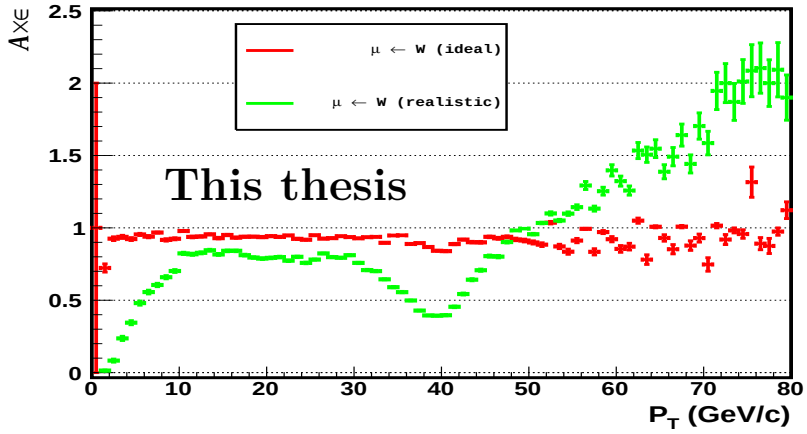

(c)

Figure 5.14: Shown here is the acceptance times efficiency versus transverse momentum per charge, in (a) is the ideal case and in (b) is realistic case whereas in (c) is both cases with no charge distinction.

Chapter 6

Summary and Conclusion

Summary

In Chapter 1 the general introduction which entailed a brief description of the properties of $W^{\pm}$, its role in the study of QGP and also its role in studying the proton structure functions or PDF of quarks. The physics motivations for studying $W^{\pm}$ as well as the aim of the work were outlined. The theoretical and literature overview were presented in two part:

- The formation of the new phase of matter was outlined and different observables and probes were mentioned with a focus on $W^{\pm}$ as initial state probes. The properties of $W^{\pm}$ which set it aside from other probes were described, for example, being medium blind.
- An overview of electroweak interaction with a focus on charged weak currents.

An overview of the LHC and its four large experiments were presented, ALICE was further discussed while putting more emphasis on the Forward Muon Spectrometer. The LHC filling schemes and machine modes with respect to the ALICE experiment, the Run Conditions and the ALICE Online and Offline framework were discussed. In what followed, the experimental conditions of the 2011 proton-proton data taking period were outlined as well as the analysis strategies used in selecting the events and tracks of interest. The runs analyzed from LHC11c, LHC11d and LHC11e are shown in Appendix III. The track selection was aimed at selecting high momentum single muons which correspond to the trigger (`CMUSH7B`) especially those events which passed the physics selection, QA, and track cuts. Presented first were all muon tracks ($all \rightarrow \mu^{\pm}$) without cuts and with no discrimination by charge, the distribution obtained from LHC11d showed reasonable statistics with number of entries 6 549 659 whereas LHC11c and LHC11e have much less statistics 2 940 756 and 924 664, respectively prior to implementing cuts, see Table 4.2. The increasing number of entries from LHC11c to LHC11d is due to the increased luminosity from ($\sim 1.975\,\mathrm{pb}^{-1}$) to ($\sim 2.975\,\mathrm{pb}^{-1}$). Although the luminosity in the case of LHC11e was higher ($\sim 4.155\,\mathrm{pb}^{-1}$) than the other periods it has the lowest number of entries, this is because not all runs in this period passed the physics selection, 20 runs were not reconstructed because there was no V0 flag, 2 runs had problems related to DAQ and CTP issues and 13 runs had CTP timing problems, and also due to beam gas contamination and pile-up the number of runs which passed the QA is smaller. Table 4.2 showed the total number of reconstructed tracks which passed the cuts, about 55.33%, 54.32% and 60.99% were rejected by the cuts for LHC11c, LHC11d and LHC11e respectively. Table 4.3 shows

the total number of entries in the $P_T \sim$ 30 - 50 GeV/c region, LHC11c, LHC11d and LHC11e have 193, 427 and 48 respectively. With an integrated luminosity of 10 pb^{-1} 3500 events of $W^{\pm} \rightarrow \mu^{\pm} + \nu_{\mu^+}(\bar{\nu}_{\mu^-})$ in the 30 - 50 GeV/c region where expected. This number was extracted by fitting the background with a beauty plus charm distribution from Fixed Order plus Next-to-Leading Logarithms [Fon13] calculation at 7 TeV center of mass energy and a template of muons from $W^{\pm}$ at a kinematic level at 8 TeV to a distribution of single muon from a simulation with full reconstruction.

It is the hint of a bump in the high momentum single muon P_T spectrum seen in the $P_T \sim$ 30 - 50 GeV/c region which prompted the simulation study for $W^{\pm} \rightarrow \mu^{\pm} + \nu_{\mu^+}(\bar{\nu}_{\mu^-})$ in pp collisions at $\sqrt{s_{NN}} = 8$ TeV in the Muon Spectrometer. This led to a Monte Carlo production of a pure signal of $W^{\pm}$ boson to investigate whether or not it is possible to achieve enough statistics 3500 $W^{\pm} \rightarrow \mu^{\pm} + \nu_{\mu^+}(\bar{\nu}_{\mu^-})$ events in the $P_T \sim$30 - 50 GeV/c in order to extract the R_{AA} of $W^{\pm}$ in 2012 at $\sqrt{s_{NN}} = 8$ TeV. Also presented in Figures 4.6(a), 4.7(a) and 4.8(a) are the yields of high momentum single muon tracks per unit of pseudorapidity, which show that negative muon tracks dominate the number of entries for LHC11c and LHC11d due to the charge asymmetry in the number of reconstructed tracks whereas the opposite is seen for LHC11e, this is unexpected because the total charge of the colliding system is positive so according to conservation of charge more positive tracks should be reconstructed. The pseudorapidity yield of both positive and negative muon tracks decreases with increasing η because most high momentum tracks will be at high rapidity and as seen from the transverse momentum distribution high P_T tracks have lower statistics. In what followed a general Monte Carlo simulation method was described as well as procedure used in simulating the $W^{\pm}$ pure signal, where reconstruction of tracks was done by considering different detector conditions. The peculiar behavior of μ^+ and μ^- in the high P_T region observed for P_T distributions in Figures 5.8(b) and 5.9(a) as well as the ratios (μ^+/μ^-) in Figures 5.13(a) and 5.13(b) seen in the case of a realistic detector conditions as compared to the ideal case led to the investigation of alignment in a study which was conducted in parallel by Du Toit et al. [DuT13] and thus also testing the detector performance in resolving high momentum tracks. High momentum tracks will leave a weak signal in the detector since they pass faster through the detector thus requiring high rates (large statistics), thus they can also be used to test the detector response. Also studied with this Monte Carlo production was the effect of different momentum cuts ($\mathbf{A_{P_T}}$ and $\mathbf{H_{P_T}}$) in reducing low transverse momentum tracks. The $\mathbf{H_{P_T}}$ cut rejects 0.094% and 7.66% of tracks accepted by $\mathbf{A_{P_T}}$ cut (see Table 5.3) for ideal and realistic case, respectively. The acceptance times efficiency plots of the ideal case in Figure 5.14(a) shows a consistency with a perfect detector conditions whereas in the realistic case the inefficiency of the detector is apparent. In both experimental and Monte Carlo productions the charge asymmetry (μ^+/μ^-) is investigated, and no conclusive remarks can be made about the charge asymmetry in experimental data due to limited statistics in the $P_T \sim$ 30 - 50 GeV/c region.

In the past $W^{\pm}$ was studied in the reactions where the net isospin was zero (e.g. $e^+ + e^- \rightarrow W + X$, $p + \bar{p} \rightarrow W + X$). Charge asymmetry in the production of $W^{\pm}$ is now studied in the $p + p \rightarrow W^{\pm} + X$ reaction. Measurements of $W^{\pm}$ at various energies at different hadron colliders (Tevatron, RHIC and Sp$\bar{p}$S) has been done, where the most recent measurements were carried out at RHIC with the PHENIX detector [Adc05] using proton and polarized-proton reaction at $\sqrt{s_{NN}} = 500$ GeV [Oid12] and at the LHC with the ATLAS [Aad12], CMS [Cha11] and LHCb [Aai12] experiments

with proton-proton collisions at half the LHC nominal energy $\sqrt{s_{NN}} = 7$ TeV in 2011. ALICE in comparison to the other three LHC experiments is a dedicated heavy ion experiment meaning that it is optimized for lead-lead studies as a result in order to undertake proton-proton collisions studies it has to keep pile-up below 2.5%. High rates are required in order to achieve enough statistics for $W^{\pm}$ study, but in the period of interest for this study the instantaneous luminosity delivered at the ALICE interaction point was limited to 0.6 - $1.2{\times}10^{29}\,\mathrm{cm}^{-2}\mathrm{s}^{-1}$ which is not ideal for $W^{\pm}$ extraction.

In ALICE the study is done in the range $-4.0 < \eta < -2.5$, whereas the other experiments like PHENIX, CMS, LHCb and ATLAS the muon acceptance is $1.2 <| \eta |< 2.2$, $| \eta |< 2.1$, $2.0 < \eta < 5.0$ and $2.0 < \eta < 2.7$ respectively. Although the ALICE Muon Spectrometer sits in the comparable acceptance region with LHCb however due to high pile-up in 2011 proton-proton collisions ALICE could not achieve the required statistics since compared to LHCb, ALICE received luminosity ∼2 orders of magnitude lower than LHCb thus the same results could not be achieved in the $W^{\pm}$ study. In addition, the ALICE Muon Spectrometer suffered beam gas interaction which resulted in unwanted contamination in statistics.

Conclusion

The limitation in statistics of LHC11c period can be attributed to low luminosity. As luminosity was increased in the LHC11d period the statistics in the $W^{\pm}$ region improved. Although the luminosity in LHC11e was higher than in both LHC11c and LHC11d there was no improvement in statistics, since most of the runs in this period had large beam gas contamination, and some runs were not reconstructed. The extraction of high momentum single muons in 2011 prompted the simulation of $W^{\pm}$ taking into account the energy and luminosity foreseen by the LHC in 2012. The results obtained in the ideal case show that it is possible to extract $W^{\pm}$ under these conditions, the limitations come from the detector performance and conditions. It is evident that when the detector conditions are correctly taken into consideration in data reconstruction they affect the signal. This can also be seen in the efficiency plots in Figure 5.14, which show the inefficiencies in the realistic detector leading to some of the low momentum positive muon tracks being reconstructed as high momentum tracks and vice versa. As a consequence we observe that the positive muon distribution in the region of $P_T > 40$ GeV/c is moving closer to the negative muon distribution in realistic case Figure 5.9(a) which is not seen in the ideal case Figure 5.3(a). As outlined before, $W^{\pm}$ can be used to test the detector performance, as demonstrated in the simulation of the realistic case. From the simulation results presented in this study it is evident that the increased energy and luminosity in 2012 pp collisions might provide improved statistics for high transverse momentum ($p_T > 20$ GeV/c) single muons as seen in Chapter 5, due to the time frame and the scope of this study these data could not be included.

The distribution of positive and negative muon tracks from the Performance Study [dVa07] is compared to the distributions from the ideal case with tracks imposed to pass standard cuts, $\mathbf{p} \times \mathbf{DCA}$ and $\mathbf{A_{P_T}}$ cut. In both cases the peak is at $p_T \sim 40$ GeV/c but in this case at 8 TeV there is large difference between the negative and positive muons in $P_T \sim 6$ - 30 GeV/c region which might be due to the cuts used, the PDF used in the Performance Study [dVa07] or the energy.

In order to improve the reconstruction of high momentum single muons the detector conditions needs to be studied and included in the data analysis. For example the

alignment is an important aspect of single muon analysis. Furthermore the detector resolution and efficiency ($A \times \epsilon$) also plays a vital role in the detector performance hence a careful correction for the efficiency must be done and taken into account during the analysis. The $A \times \epsilon$ plots are shown in Figure 5.14 to show the realistic detector effects. It is due to this effect that the muon analysis group embarked on studying the effects of the above mentioned detector related issues. This make the 2012 pp data at 8 TeV very interesting. In order to deal with the increased luminosity and energy foreseen after the long shutdown the ALICE trigger rate has to be improved. The next step is to analyze the 2012 data to see if the increased center of mass energy and luminosity has any effect despite the detector problems and await patiently for the next LHC run.

All in all it has been fun looking through the microscope of time.

Part I

Appendix: Electroweak Theory

Historical Background

Electricity and magnetism where once thought of as two separate entities, until 1863 when James Clark Maxwell publication *Treatise on Electricity and Magnetism* in which he showed that negative charge interactions and positive charge interactions are regulated by the same force. From then it has been a mission of the physics community to unite all four forces of nature into one Grand Unified Theory, which governs all interactions. In 1968 Salam, Weinberg and Glashow unified the electromagnetism and weak interaction into electro-weak theory with weak bosons as mediators of this interaction. Weak interaction is a flavor changing phenomenon, this process occurs in nuclear reactions and nuclear decays.

$$n^0 \rightarrow p^+ + e^- \text{ - weak interaction.}$$

The above process seemed to violate the energy conservation laws, the energy spectrum of the beta particle showed a broad distribution whereas a spike was expected. In 1930 Wolfgang Pauli in an open letter to the radio−activity community proposed a particle of vanishing mass which carried the remnant energy. Fermi went on to name this particle a neutrino and constructed his four-fermion theory of weak interaction [Qui02].

$$n^0 \rightarrow p^+ + e^- + \bar{\nu}_e \text{ - weak interaction.}$$

Electromagnetism is mediated by photon exchange between charges. This is an interaction between charged particle at rest and the combined effect of the electric and magnetic forces acting between charge particles moving relative to each other. Weak interaction is a short range interaction which does not produce bound states as do other interactions [Gre10]. In 1963 Sheldon Glasgow proposed the unification of the weak nuclear force and the electromagnetism, followed by independent works of Abdus Salam and Steven Weinberg in 1967 building up on Glasgow's work showing that the masses of the massive gauge bosons arises from spontaneous symmetry breaking with the Higgs mechanism. This work of Glasgow, Weinberg and Salam was further proven by Gerardus t´Hooft to be mathematically consistent in 1974. *Spontaneous symmetry breaking*,that is the Hamiltonian is invariant under certain transformation, either the vacuum state of the Hamiltonian is not invariant, these can also be realized in ferromagnets. This breaking of symmetry which is associated with creation of massive vector fields solves the problem of renormalizabilty [Kak93].

The Glasgow-Weinberg-Salam model is a non-Abelian $SU(2)_L \times U(1)_Y$ which is generated by the isospin operators I_1, I_2 and I_3 and hypercharge Y, it contains three $SU(2)_L$ bosons $W^i_\mu, i = 1, 2, 3$ and one $U(1)_Y$ gauge boson B_μ [Daw98]. In addition to the four gauge bosons of the electroweak theory the Standard Model predicts an existence of at least one heavy spin-0 boson-the Higgs boson in which the mass giving mechanism relies [dVa07]. This mechanism breaks the symmetry of the postulated gauge bosons giving mass to three of them and leaving the photon massless. Electro-weak theory has three parameters the electromagnetic coupling constant e,$\alpha = e^2/\hbar c$, the Fermi coupling constant $G_F/(\hbar c)^3 = 1.166.10^{-5} GeV^{-2}$ and the Weinberg angle which describes the mixing of the gauge fields to make the four observable bosons,$\sin^2\theta_W = 0.23$ [dVa07].

Construction of Electro-weak Theory

The formalism of electroweak theory is constructed in analogy to the quantum electrodynamics (QED) theory, in both cases interaction are expected to be mediated by gauge fields. In case of QED the Lagrangian is

$$\mathcal{L}_{int}^{em} = -iej_{\mu}^{em}A^{\mu} \tag{6.1}$$

Where,e is the $U(1)_{\bar{Q}}$ coupling, $j_{\mu}^{em} = \bar{\psi}\gamma_{\mu}Q_{\mu}\psi$ is the $U(1)_{\bar{Q}}$ current and A^{μ} $U(1)_{\bar{Q}}$ gauge field(photon). The same is done for the $SU(2)_L$ of electro-weak theory for a current triplet and singlet with a vector-axial (V-A) coupling where the chirality operator is included, the V-A coupling - $\gamma_{\mu}(1-\gamma^5)$,

$$\mathcal{L}_{int}^{EW} = -igj_{\mu}^{i}W^{i\mu} - i\frac{g'}{2}j_{\mu}^{Y}B^{\mu} \tag{6.2}$$

This difference in coupling explains that while the weak interaction violates parity (P), the electromagnetic interaction does not. The gauge field triplets $W^{i\mu}$ and j_{μ} and singlets B^{μ} and j^{Y} are associated with the weak isospin and weak hypercharge respectively. Coupled to this gauge fields is a complex scalar $SU(2)_L$

$$\Phi = \begin{pmatrix} \psi^{+} \\ \psi^{0} \end{pmatrix}$$

, with a renormalizable $SU(2)_L$ scalar potential. The minima of this potential do not occur at $\phi^0 = 0$ and hence the scalar field develops a vacuum expectation value. We choose the vacuum expectation value to be

$$\langle\Phi\rangle = \frac{1}{\sqrt{2}}\begin{pmatrix} 0 \\ \upsilon \end{pmatrix}$$

and with this choice of vacuum expectation value (VEV) the scalar doublet $U(1)_Y$ has a charge $Y_{\phi} = 1$ and the electromagnetic charge is $Q = \frac{(\tau_3+Y)}{2}$ Gell-Mann–Nishijima relation therefore $Q\langle\phi\rangle = 0$ and electromagnetism is unbroken by the scalar VEV.

In unitary gauge, the scalar doublet can be written in terms of a physical scalar Higgs field - h, as

$$\langle\phi\rangle = \frac{1}{\sqrt{2}}\begin{pmatrix} 0 \\ \upsilon + h \end{pmatrix}$$

which gives the contribution to the gauge boson masses from the scalar kinetic energy.

The physical gauge fields are massive charged vector bosons

$$W^{\pm\mu} = \frac{1}{\sqrt{2}} \cdot (W^{1\mu} \mp iW^{2\mu}) \tag{6.3}$$

as well as neutral vector bosons as a linear combination of $W^{i\mu}$ and B^{μ},

$$A^{\mu} = B^{\mu}\cos\theta_w + W^{3\mu}\sin\theta_w \qquad massless \rightarrow \gamma \tag{6.4}$$

$$Z^{\mu} = -B^{\mu}\sin\theta_w + W^{3\mu}\sin\theta_w \qquad massive \rightarrow Z^0 \tag{6.5}$$

where, θ_w is the Weinberg angle or the weak mixing angle.

Substituting (6.4), (6.5) and (6.6) into the Lagrangian of neutral electroweak currents (6.3) we get,

$$-igj^i_{\mu}W^{i\mu} - i\frac{g'}{2}j^Y_{\mu}B^{\mu} = -i(g\sin\theta_w j^3_{\mu} + g'\cos\theta_w\frac{j^Y_{\mu}}{2})A^{\mu} - i(g\cos\theta_w j^3_{\mu} + g'\sin\theta_w\frac{j^Y_{\mu}}{2})Z^{\mu}$$

The first term on the right correspond to the electromagnetic current, for which $j^{em}_{\mu} = j^3_{\mu} + \frac{1}{2}\cdot j^Y_{\mu}$ implying that

$$g\sin\theta_w = g'\cos\theta_w = e \tag{6.6}$$

[dVa07][Daw98][Hol06].

Part II

Appendix: Analysis Task & Simulation Macros

The configuration file used in production of the $W^{\pm}$ pure signal. This file is used to set different inputs needed to run the simulation namely to set the event generator, magnetic field, the PDFs, processes, etc.

```
// Config file MUON + ITS (for vertex) for PDC06
// Tuned for p+p min biais and quarkonia production (AliGenMUONCocktailpp)
// Remember to define the directory and option
// gAlice->SetConfigFunction("Config('$HOME','box');");
// april 3rd: added L3 magnet
#if !defined(__CINT__) || defined(__MAKECINT__)
#include <Riostream.h>
#include <TRandom.h>
#include <TDatime.h>
#include <TSystem.h>
#include <TVirtualMC.h>
#include <TGeant3TGeo.h>
#include "STEER/AliRunLoader.h"
#include "STEER/AliRun.h"
#include "STEER/AliConfig.h"
#include "PYTHIA6/AliDecayerPythia.h"
#include "PYTHIA6/AliGenPythia.h"
#include "TDPMjet/AliGenDPMjet.h"
#include "STEER/AliMagFCheb.h"
#include "STRUCT/AliBODY.h"
#include "STRUCT/AliMAG.h"
#include "STRUCT/AliABSOv3.h"
#include "STRUCT/AliDIPOv3.h"
#include "STRUCT/AliHALLv3.h"
#include "STRUCT/AliFRAMEv2.h"
#include "STRUCT/AliSHILv3.h"
#include "STRUCT/AliPIPEv3.h"
#include "ITS/AliITSv11Hybrid.h"
#include "TPC/AliTPCv2.h"
#include "TOF/AliTOFv6T0.h"
#include "HMPID/AliHMPIDv3.h"
#include "ZDC/AliZDCv3.h"
#include "TRD/AliTRDv1.h"
#include "TRD/AliTRDgeometry.h"
#include "FMD/AliFMDv1.h"
#include "MUON/AliMUONv1.h"
#include "PHOS/AliPHOSv1.h"
#include "PHOS/AliPHOSSimParam.h"
#include "PMD/AliPMDv1.h"
#include "T0/AliT0v1.h"
#include "EMCAL/AliEMCALv2.h"
#include "ACORDE/AliACORDEv1.h"
#include "VZERO/AliVZEROv7.h"
#endif

//--- Functions ---
class AliGenPythia;
void ProcessEnvironmentVars();

static Int_t runNumber = 0;
TDatime dt;
static UInt_t seed = dt.Get();

```

```
54 // Comment line
55 static TString comment;
56
57 void Config()
58 {
59
60   // Get settings from environment variables
61     ProcessEnvironmentVars();
62
63     gRandom->SetSeed(seed);
64     cerr<<"Seed for random number generation= "<<seed<<endl;
65
66     //=======================================================
67   //  Libraries required by geant321
68 #if defined(__CINT__)
69     gSystem->Load("liblhapdf");       // Parton density functions
70     gSystem->Load("libEGPythia6");    // TGenerator interface
71     gSystem->Load("libpythia6");      // Pythia
72     gSystem->Load("libAliPythia6");   // ALICE specific implementations
73     gSystem->Load("libgeant321");
74 #endif
75
76     new TGeant3TGeo("C++ Interface to Geant3");
77
78   //  Create the output file
79     AliRunLoader* rl=0x0;
80     cout <<"Config.C: Creating Run Loader ..."<< endl;
81     rl = AliRunLoader::Open(
82   "galice.root", AliConfig::GetDefaultEventFolderName(), "recreate");
83     if (rl == 0x0) {
84     gAlice->Fatal("Config.C","Can not instatiate the Run Loader");
85     return;
86     }
87     rl->SetCompressionLevel(2);
88     rl->SetNumberOfEventsPerFile(10000);
89     gAlice->SetRunLoader(rl);
90
91   //
       ==========================================================


92   // Set External decayer
93     TVirtualMCDecayer *decayer = new AliDecayerPythia();
94     decayer->SetForceDecay(kAll);
95     decayer->Init();
96     gMC->SetExternalDecayer(decayer);
97
98   //
       ==========================================================


99   // ******* GEANT STEERING parameters FOR ALICE SIMULATION *******
100    gMC->SetProcess("DCAY",1);
101    gMC->SetProcess("PAIR",1);
102    gMC->SetProcess("COMP",1);
103    gMC->SetProcess("PHOT",1);
104    gMC->SetProcess("PFIS",0);
105    gMC->SetProcess("DRAY",0);
106    gMC->SetProcess("ANNI",1);
107    gMC->SetProcess("BREM",1);
```

```
108     gMC->SetProcess("MUNU",1);
109     gMC->SetProcess("CKOV",1);
110     gMC->SetProcess("HADR",1);
111     gMC->SetProcess("LOSS",2);
112     gMC->SetProcess("MULS",1);
113     gMC->SetProcess("RAYL",1);
114 
115     Float_t cut = 1.e-3;         // 1MeV cut by default
116     Float_t tofmax = 1.e10;
117 
118     gMC->SetCut("CUTGAM", cut);
119     gMC->SetCut("CUTELE", cut);
120     gMC->SetCut("CUTNEU", cut);
121     gMC->SetCut("CUTHAD", cut);
122     gMC->SetCut("CUTMUO", cut);
123     gMC->SetCut("BCUTE",  cut);
124     gMC->SetCut("BCUTM",  cut);
125     gMC->SetCut("DCUTE",  cut);
126     gMC->SetCut("DCUTM",  cut);
127     gMC->SetCut("PPCUTM", cut);
128     gMC->SetCut("TOFMAX", tofmax);
129 
130 //  W production (Zaida Config.)
131 
132     AliGenPythia *gener = new AliGenPythia(1);
133 
134     gener->SetProcess(kPyW);
135     gener->SetStrucFunc(kCTEQ5L);
136     gener->SetEnergyCMS(8000.);
137     gener->SetPtRange(0,1.e10);
138     gener->SetYRange(-12.0,12.0);
139     gener->SetPhiRange(0., 360.);
140     gener->SetPtHard(0.,-1.0);
141 
142     gener->SetCutOnChild(1);
143     gener->SetChildPtRange(1.0,1000.);
144     gener->SetThetaRange(171.0,178.0);
145     gener->SetNumberOfAcceptedParticles(1); //need a muon inside
146     gener->SetPdgCodeParticleforAcceptanceCut(13); //the muon arm
            acceptance
147     gener->SetOrigin(0.,0., 0.);  //vertex position
148     gener->SetSigma(0.0, 0.0, 0.0);          //Sigma
149     gener->SetForceDecay(kWToMuon);
150     gener->SetTrackingFlag(1);
151     gener->Init();
152 
153 
154 
155   //=============================================================
156   // Field (L3 0.5 T) outside dimuon spectrometer
157   //AliMagF *field = new AliMagF("Maps","Maps", 2, 1., 1., 10., AliMagF::
        k5kG);
158     //    AliMagF *field = new AliMagF("Maps","Maps", -1., -1., AliMagF::
          k5kG,AliMagF::kBeamTypepp, 7000/2.0);
159     //TGeoGlobalMagField::Instance()->SetField(field);
160 
161     rl->CdGAFile();
162 
```

```
163     Int_t iABSO   = 1;
164     Int_t iACORDE= 0;
165     Int_t iDIPO   = 1;
166     Int_t iEMCAL = 0;
167     Int_t iFMD    = 1;
168     Int_t iFRAME = 1;
169     Int_t iHALL   = 1;
170     Int_t iITS    = 0;
171     Int_t iMAG    = 1;
172     Int_t iMUON   = 1;
173     Int_t iPHOS   = 0;
174     Int_t iPIPE   = 1;
175     Int_t iPMD    = 0;
176     Int_t iHMPID = 0;
177     Int_t iSHIL   = 1;
178     Int_t iT0     = 0;
179     Int_t iTOF    = 0;
180     Int_t iTPC    = 0;
181     Int_t iTRD    = 0;
182     Int_t iVZERO = 1;
183     Int_t iZDC    = 0;
184
185    //================== Alice BODY parameters
         ===========================
186     AliBODY *BODY = new AliBODY("BODY", "Alice envelop");
187
188
189     if (iMAG)
190     {
191         //==================== MAG parameters ============================
192         // --- Start with Magnet since detector layouts may be depending
              ---
193         // --- on the selected Magnet dimensions ---
194         AliMAG *MAG = new AliMAG("MAG", "Magnet");
195     }
196
197
198     if (iABSO)
199     {
200         //==================== ABSO parameters
              ============================
201         AliABSO *ABSO = new AliABSOv3("ABSO", "Muon Absorber");
202     }
203
204     if (iDIPO)
205     {
206         //==================== DIPO parameters
              ============================
207
208         AliDIPO *DIPO = new AliDIPOv3("DIPO", "Dipole version 3");
209     }
210
211     if (iHALL)
212     {
213         //==================== HALL parameters
              ============================
214
215         AliHALL *HALL = new AliHALLv3("HALL", "Alice Hall");
```

```
216     }
217
218
219     if (iFRAME)
220     {
221         //=================== FRAME parameters
                ============================
222
223         AliFRAMEv2 *FRAME = new AliFRAMEv2("FRAME", "Space Frame");
224   FRAME->SetHoles(1);
225     }
226
227     if (iSHIL)
228     {
229         //=================== SHIL parameters
                ============================
230
231         AliSHIL *SHIL = new AliSHILv3("SHIL", "Shielding Version 3");
232     }
233
234
235     if (iPIPE)
236     {
237         //=================== PIPE parameters
                ============================
238
239         AliPIPE *PIPE = new AliPIPEv3("PIPE", "Beam Pipe");
240     }
241
242     if (iITS)
243     {
244         //=================== ITS parameters ============================
245
246   //AliITS *ITS  = new AliITSv11Hybrid("ITS","ITS v11Hybrid");
247    AliITS *ITS  = new AliITSv11("ITS","ITS");
248     }
249
250     if (iTPC)
251     {
252       //============================ TPC parameters ====================
253
254         AliTPC *TPC = new AliTPCv2("TPC", "Default");
255     }
256
257
258     if (iTOF) {
259         //=================== TOF parameters ============================
260
261   AliTOF *TOF = new AliTOFv6T0("TOF", "normal TOF");
262     }
263
264
265     if (iHMPID)
266     {
267         //=================== HMPID parameters
                ============================
268
269         AliHMPID *HMPID = new AliHMPIDv3("HMPID", "normal HMPID");
```

```
270
271     }
272
273
274     if (iZDC)
275     {
276         //=================== ZDC parameters ============================
277
278         AliZDC *ZDC = new AliZDCv3("ZDC", "normal ZDC");
279   ZDC->SetSpectatorsTrack();
280         ZDC->SetLumiLength(0.);
281     }
282
283     if (iTRD)
284     {
285         //=================== TRD parameters ============================
286
287         AliTRD *TRD = new AliTRDv1("TRD", "TRD slow simulator");
288         AliTRDgeometry *geoTRD = TRD->GetGeometry();
289   // Partial geometry: modules at 0,1,7,8,9,16,17
290   // starting at 3h in positive direction
291   geoTRD->SetSMstatus(2,0);
292   geoTRD->SetSMstatus(3,0);
293   geoTRD->SetSMstatus(4,0);
294         geoTRD->SetSMstatus(5,0);
295   geoTRD->SetSMstatus(6,0);
296         geoTRD->SetSMstatus(11,0);
297         geoTRD->SetSMstatus(12,0);
298         geoTRD->SetSMstatus(13,0);
299         geoTRD->SetSMstatus(14,0);
300         geoTRD->SetSMstatus(15,0);
301         geoTRD->SetSMstatus(16,0);
302     }
303
304     if (iFMD)
305     {
306         //=================== FMD parameters ============================
307
308   AliFMD *FMD = new AliFMDv1("FMD", "normal FMD");
309    }
310
311     if (iMUON)
312     {
313         //=================== MUON parameters ===========================
314         // New MUONv1 version (geometry defined via builders)
315   AliMUON *MUON = new AliMUONv1("MUON", "default");
316   // activate trigger efficiency by cells
317   MUON->SetTriggerEffCells(1);  // not needed if raw masks
318     }
319
320     if (iPHOS)
321     {
322         //=================== PHOS parameters ===========================
323
324      AliPHOS *PHOS = new AliPHOSv1("PHOS", "noCPV_Modules123");
325
326     }
327
```

```
328
329     if (iPMD)
330     {
331         //=================== PMD parameters ============================
332
333         AliPMD *PMD = new AliPMDv1("PMD", "normal PMD");
334     }
335
336     if (iT0)
337     {
338         //=================== T0 parameters ============================
339         AliT0 *T0 = new AliT0v1("T0", "T0 Detector");
340     }
341
342     if (iEMCAL)
343     {
344         //=================== EMCAL parameters
                ============================
345
346         AliEMCAL *EMCAL = new AliEMCALv2("EMCAL", "EMCAL_COMPLETEV1");
347     }
348
349      if (iACORDE)
350     {
351         //=================== ACORDE parameters
                ============================
352
353         AliACORDE *ACORDE = new AliACORDEv1("ACORDE", "normal ACORDE");
354     }
355
356      if (iVZERO)
357     {
358         //=================== ACORDE parameters
                ============================
359
360         AliVZERO *VZERO = new AliVZEROv7("VZERO", "normal VZERO");
361     }
362 }
363
364 Float_t EtaToTheta(Float_t arg){
365   return (180./TMath::Pi())*2.*atan(exp(-arg));
366 }
367
368 void ProcessEnvironmentVars()
369 {
370
371     // Random Number seed
372     if (gSystem->Getenv("CONFIG_SEED")) {
373   seed = atoi(gSystem->Getenv("CONFIG_SEED"));
374     }
375     // Run number
376     if (gSystem->Getenv("DC_RUN")) {
377       runNumber = atoi(gSystem->Getenv("DC_RUN"));
378     }
379 }
```

The macro below is used to generate events. It calls the event generator interfaced to ROOT and initialized in the Config.C. In this file you can select which detector to create

hits for.

```
void sim(Int_t nev=5000) {

  AliSimulation simulator;

// simu run/run (no RejectList)
//  simulator.SetConfigFile("Config.C");
  simulator.SetTriggerConfig("MUON");
  simulator.SetMakeSDigits("MUON");
  simulator.SetMakeDigits("MUON");
  simulator.SetMakeDigitsFromHits("");
  simulator.SetRunQA("MUON:ALL");
  simulator.SetRunHLT("");
  simulator.SetWriteRawData("ALL","raw.root",kTRUE);
  //Default = Ideal OCDB
  simulator.SetDefaultStorage("alien://folder=/alice/simulation/2008/v4
      -15-Release/Ideal");

 //CTP (muon standalone)
 simulator.SetSpecificStorage("GRP/CTP/Config", "alien://folder=/alice/
     cern.ch/user/b/bogdan/prod2011/cdb");


 //Vertex and Mag.field from OCDB
 simulator.UseVertexFromCDB();
 simulator.SetSpecificStorage("GRP/GRP/Data","alien://folder=/alice/data
     /2011/OCDB");
  simulator.UseMagFieldFromGRP();

  TStopwatch timer;
  timer.Start();
  simulator.Run(nev);
  timer.Stop();
  timer.Print();
}
```

The file below is used in the reconstrution of the hits produced by the above macro, reconstruction can be done for the detectors of interest to reduced the CPU time needed for simulating the whole detector.

```
void rec() {
  AliReconstruction reco;


// run/run (No RejectList)
  reco.SetCleanESD(kFALSE);
  reco.SetWriteAlignmentData();

  reco.SetRunLocalReconstruction("MUON");
  reco.SetRunTracking("MUON");
  reco.SetRunVertexFinder(kFALSE);
  reco.SetFillESD("MUON");
  reco.SetRunQA("MUON:ALL");

// Default = raw OCDB
  reco.SetDefaultStorage("alien://Folder=/alice/data/2011/OCDB");
 reco.SetDefaultStorage("alien://Folder=/alice/simulation/2008/v4-15-
     Release/Ideal");
```

```
//tracking
  reco.SetSpecificStorage("MUON/Align/Data","alien://folder=/alice/
      simulation/2008/v4-15-Release/Ideal");

// CTP
  reco.SetSpecificStorage("GRP/CTP/Config","alien://folder=/alice/cern.ch
      /user/b/bogdan/prod2011/cdb");
//  reco.SetSpecificStorage("GRP/CTP/Config","alien://folder=/alice/cern.
    ch/user/b/bastid/OCDB");  // for test

// GRP from local OCDB
 reco.SetSpecificStorage("GRP/GRP/Data",
                         Form("local://%s",gSystem->pwd()));

  TStopwatch timer;
  timer.Start();
  reco.Run();
  timer.Stop();
  timer.Print();
}
```

Below is the analysis task used in extracting high transverse momentum muons from experimental data.

```
#ifndef AliAnalysisTaskPt_cxx
#define AliAnalysisTaskPt_cxx

// example of an analysis task creating a p_t spectrum
// Authors: Panos Cristakoglou, Jan Fiete Grosse-Oetringhaus, Christian
    Klein-Boesing
//Modified by K.J Senosi to perform the specific high p_{T} single muon
    study.
class TH1F;
class AliESDEvent;
class AliAODEvent;
class AliMuonEventCuts;
class AliMuonTrackCuts;

#include "AliAnalysisTaskSE.h"

class AliAnalysisTaskPt : public AliAnalysisTaskSE {
 public:
  AliAnalysisTaskPt() : AliAnalysisTaskSE(),
  fAOD(0),
  fOutputList(0),
  fHistPtPlus(0),
  fHistPtMinus(0),
  fHistEtaPlus(0),
  fHistEtaMinus(0),
  fHistVzMinus(0),
  fHistVzPlus(0),
  fHistPtAll(0),
  fHistRatio(0),
  fMuonTrackCuts(0)
  AliAnalysisTaskPt(const char *name);
  virtual ~AliAnalysisTaskPt() {}

  virtual void   UserCreateOutputObjects();
  virtual void   NotifyRun();
```

```
34    virtual void    UserExec(Option_t *option);
35    virtual void    Terminate(Option_t *);
36
37  private:
38    AliAODEvent *fAOD;     //! ESD object
39    TList       *fOutputList; //! Output list
40    TH1F        *fHistPtPlus; //! Pt spectrum
41    TH1F        *fHistPtMinus;
42    TH1F        *fHistEtaPlus;
43    TH1F        *fHistEtaMinus;
44    TH1F        *fHistRatio;
45    TH1F        *fHistVzMinus;
46    TH1F        *fHistVzPlus;
47    TH1F        *fHistPtAll;
48    AliMuonTrackCuts* fMuonTrackCuts;
49
50    AliAnalysisTaskPt(const AliAnalysisTaskPt&); // not implemented
51    AliAnalysisTaskPt& operator=(const AliAnalysisTaskPt&); // not
        implemented
52
53    ClassDef(AliAnalysisTaskPt, 1); // example of analysis
54  };
55
56  #endif
```

```
1  #include "TChain.h"
2  #include "TTree.h"
3  #include "TH1F.h"
4  #include "TCanvas.h"
5
6  #include "AliAnalysisTask.h"
7  #include "AliAnalysisManager.h"
8
9
10 #include "AliESDEvent.h"
11 #include "AliESDInputHandler.h"
12
13 #include "AliAODTrack.h"
14 #include "AliAODEvent.h"
15 #include "AliAODInputHandler.h"
16
17
18 #include "AliOADBMuonTrackCutsParam.h"
19 #include "AliAnalysisMuonUtility.h"
20 #include "AliMuonEventCuts.h"
21 #include "AliMuonTrackCuts.h"
22 #include "AliAnalysisTaskPt.h"
23 // example of an analysis task creating a p_t spectrum
24 // Authors: Panos Cristakoglou, Jan Fiete Grosse-Oetringhaus, Christian
     Klein-Boesing
25 // Reviewed: A.Gheata (19/02/10)
26 //Modified by K.J Senosi to perform the specific high p_{T} single muon
     study.
27 ClassImp(AliAnalysisTaskPt)
28
29 //________________________________________________
30 AliAnalysisTaskPt::AliAnalysisTaskPt(const char *name)
31   : AliAnalysisTaskSE(name),
```

```
32    fAOD(0),
33    fOutputList(0),
34    fHistPtPlus(0),
35    fHistPtMinus(0),
36    fHistEtaPlus(0),
37    fHistEtaMinus(0),
38    fHistRatio(0),
39    fHistVzMinus(0),
40    fHistVzPlus(0),
41    fHistPtAll(0),
42    fMuonTrackCuts(0),
43 {
44    // Constructor
45
46    // Define input and output slots here
47    // Input slot #0 works with a TChain
48    DefineInput(0, TChain::Class());
49    // Output slot #0 id reserved by the base class for AOD
50    // Output slot #1 writes into a TH1 container
51    DefineOutput(1, TList::Class());
52 }
53
54 //-----------------------------------------------------
55 void AliAnalysisTaskPt::UserCreateOutputObjects()
56 {
57    // Create histograms
58    // Called once
59    fOutputList = new TList();
60    fOutputList->SetOwner();
61
62    Bool_t useMC = kFALSE;
63    fMuonTrackCuts = new AliMuonTrackCuts("TrackCuts","TrackCuts");
64    fMuonTrackCuts->SetFilterMask (AliMuonTrackCuts::kMuEta |
          AliMuonTrackCuts::kMuThetaAbs | AliMuonTrackCuts::kMuPdca |
          AliMuonTrackCuts::kMuMatchHpt);
65    fMuonTrackCuts->SetIsMC(useMC);
66    fMuonTrackCuts->Print("mask");
67    fMuonTrackCuts->SetPassNumber(1);
68    fMuonTrackCuts->SetAllowDefaultParams(kTRUE);
69
70    fHistPtPlus = new TH1F("fHistPtPlus", "P_{T} distribution", 100, 0.0,
          100.0);
71    fHistPtPlus->GetXaxis()->SetTitle("P_{T} (GeV/c)");
72    fHistPtPlus->GetYaxis()->SetTitle("dN/dP_{T} (c/GeV)");
73    fHistPtPlus->SetMarkerStyle(kFullCircle);
74
75    fHistPtMinus = new TH1F("fHistPtMinus", "P_{T} distribution", 100, 0.0,
          100.0);
76    fHistPtMinus->GetXaxis()->SetTitle("P_{T} (GeV/c)");
77    fHistPtMinus->GetYaxis()->SetTitle("dN/dP_{T} (c/GeV)");
78    fHistPtMinus->SetMarkerStyle(kOpenCircle);
79
80    fHistEtaPlus = new TH1F("fHistEtaPlus", "#eta distribution", 100, -4.0,
          -2.5);
81    fHistEtaPlus->GetXaxis()->SetTitle("P_{T} (GeV/c)");
82    fHistEtaPlus->GetYaxis()->SetTitle("dN/dP_{T} (c/GeV)");
83    fHistEtaPlus->SetMarkerStyle(kFullCircle);
84
```

```
85    fHistEtaMinus = new TH1F("fHistEtaMinus", "#eta distribution", 100,
          -4.0, -2.5);
86    fHistEtaMinus->GetXaxis()->SetTitle("P_{T} (GeV/c)");
87    fHistEtaMinus->GetYaxis()->SetTitle("dN/dP_{T} (c/GeV)");
88    fHistEtaMinus->SetMarkerStyle(kOpenCircle);
89
90    fHistRatio = new TH1F("fHistRatio", "ratio of mu-plus and mu-minus",
          100, 0.0, 100.0);
91    fHistRatio->GetXaxis()->SetTitle("P_{T} (GeV/c)");
92    fHistRatio->GetYaxis()->SetTitle("#frac{(dN/dP_{T})^{#mu^{+}}}{(dN/dP_{
          T})^{#mu^{-}}}");
93    fHistRatio->SetMarkerStyle(kFullCircle);
94    fHistRatio->SetMarkerColor(4);
95
96   fHistVzPlus = new TH1F("fHistVzPlus", "#eta distribution", 60, -15.0,
         15.0);
97   fHistVzPlus->GetXaxis()->SetTitle("P_{T} (GeV/c)");
98   fHistVzPlus->GetYaxis()->SetTitle("dN/dV_{z} (/cm)");
99   fHistVzPlus->SetMarkerStyle(kFullCircle);
100
101  fHistVzMinus = new TH1F("fHistVzMinus", "#eta distribution", 60, -15.0,
         15.0);
102  fHistVzMinus->GetXaxis()->SetTitle("P_{T} (GeV/c)");
103  fHistVzMinus->GetYaxis()->SetTitle("dN/dV_{z} (/cm)");
104  fHistVzMinus->SetMarkerStyle(kOpenCircle);
105
106   fHistPtAll = new TH1F("fHistPtAll", "P_{T} distribution", 100, 0.0,
          100.0);
107   fHistPtAll->GetXaxis()->SetTitle("P_{T} (GeV/c)");
108   fHistPtAll->GetYaxis()->SetTitle("dN/dP_{T} (c/GeV)");
109   fHistPtAll->SetMarkerStyle(kFullCircle);
110
111   fOutputList->Add(fHistPtPlus);
112   fOutputList->Add(fHistPtMinus);
113   fOutputList->Add(fHistEtaPlus);
114   fOutputList->Add(fHistEtaMinus);
115   fOutputList->Add(fHistRatio);
116   fOutputList->Add(fHistVzPlus);
117   fOutputList->Add(fHistVzMinus);
118
119   fOutputList->Add(fHistPtAll);
120
121   PostData(1, fOutputList);
122   }
123
124 //-----------------------------------------------------
125 void AliAnalysisTaskPt::NotifyRun()
126 {
127    /// Set run number for cuts
128  fMuonTrackCuts->SetRun(fInputHandler);
129 }
130 //-----------------------------------------------------
131 void AliAnalysisTaskPt::UserExec(Option_t *)
132 {
133       // Main loop
134       // Called for each event
135       AliAODEvent* aodEvent =  0x0;
136       aodEvent = dynamic_cast<AliAODEvent*>(InputEvent());
```

```
137      if (!aodEvent) {
138      printf("ERROR: aodEvent not available\n");
139      return;
140      }
141 //       printf("There are %d tracks in this event\n", aodEvent->
     GetNTracks());
142      AliVParticle* track = 0x0;
143      // Track loop to fill a pT spectrum
144      for (Int_t iTracks = 0; iTracks < aodEvent->GetNTracks(); iTracks++)
          {
145      //AliAODTrack* track = fAOD->GetTrack(iTracks);
146      track = aodEvent->GetTrack(iTracks);
147      if (!track) {
148       printf("ERROR: Could not receive track %d\n", iTracks);
149       continue;
150      }
151
152         fHistPtAll->Fill(track->Pt());
153
154     if(!fMuonTrackCuts->IsSelected(track))continue;
155      // printf("FOUND: Muon");
156     if(track->Charge()<0){
157      const AliVVertex* primaryVertex =dynamic_cast<const AliAODEvent*>(
          InputEvent())->GetPrimaryVertexSPD(); ///Used to test if it
          fills for speacially selected tracks.
158     if ( primaryVertex->GetNContributors() < 1 ) return;
159     Double_t ipVz = primaryVertex->GetZ();
160
161     fHistPtMinus->Fill(track->Pt());
162     fHistEtaMinus->Fill(track->Eta());
163     fHistVzMinus->Fill(ipVz);
164        }else{
165     const AliVVertex* primaryVertex =dynamic_cast<const AliAODEvent*>(
          InputEvent())->GetPrimaryVertexSPD(); ///Used to test if it fills
          for speacially selected tracks.
166     if( primaryVertex->GetNContributors() < 1 ) return;
167     Double_t ipVz = primaryVertex->GetZ();
168
169     fHistPtPlus->Fill(track->Pt());
170     fHistEtaPlus->Fill(track->Eta());
171     fHistVzPlus->Fill(ipVz);
172          }
173      } //track loop
174
175       PostData(1, fOutputList); // Post output data.
176     }
177 //----------------------------------------------------
178 void AliAnalysisTaskPt::Terminate(Option_t *)
179 {
180   // Draw result to the screen
181   // Called once at the end of the query
182   fOutputList = dynamic_cast<TList*> (GetOutputData(1));
183   if (!fOutputList) {
184     printf("ERROR: Output list not available\n");
185     return;
186   }
187   fHistPtPlus = dynamic_cast<TH1F*> (fOutputList->At(0));
188   if (!fHistPtPlus) {
```

```
189     printf("ERROR: fHistPtMinus not available\n");
190     return;
191   }
192
193   fHistPtMinus = dynamic_cast<TH1F*> (fOutputList->At(1));
194   if (!fHistPtMinus) {
195     printf("ERROR: fHistPtMinus not available\n");
196     return;
197   }
198
199    fHistEtaPlus = dynamic_cast<TH1F*> (fOutputList->At(2));
200   if (!fHistEtaPlus) {
201     printf("ERROR: fHistEtaPlus not available\n");
202     return;
203   }
204
205   fHistEtaMinus = dynamic_cast<TH1F*> (fOutputList->At(3));
206   if (!fHistEtaMinus) {
207     printf("ERROR: fHistEtaMinus not available\n");
208     return;
209 }
210
211    fHistRatio = dynamic_cast<TH1F*> (fOutputList->FindObject("fHistRatio"
       ));
212    if (!fHistRatio) {
213      Printf("ERROR: fHistRatio not available");
214      return;
215    }
216
217   fHistVzMinus = dynamic_cast<TH1F*> (fOutputList->FindObject("
       fHistVzMinus"));
218   if (!fHistVzMinus) {
219     printf("ERROR: fHistVzMinus not available\n");
220     return;
221   }
222
223   fHistVzPlus = dynamic_cast<TH1F*> (fOutputList->FindObject("fHistVzPlus
       "));
224   if (!fHistVzPlus) {
225     printf("ERROR: fHistVzPlus not available\n");
226     return;
227 }
228
229   fHistPtAll = dynamic_cast<TH1F*> (fOutputList->FindObject("fHistPtAll")
       );
230   if (!fHistPtAll) {
231     printf("ERROR: fHistPtMinus not available\n");
232     return;
233   }
234
235   TCanvas *c1 = new TCanvas("AliAnalysisTaskPt","Pt",10,10,510,510);
236   c1->cd(1)->SetLogy();
237
238   fHistPtMinus->DrawCopy("E");
239   c1->cd(1)->SetLogy();
240   fHistPtPlus->DrawCopy("Esames");
241
242   TCanvas *c2 = new TCanvas("AliAnalysisTaskEta","Eta",10,10,510,510);
```

```
243     c2->cd(1)->SetLogy();
244     fHistEtaMinus->DrawCopy("E");
245     c2->cd(1)->SetLogy();
246     fHistEtaPlus->DrawCopy("Esames");
247 
248     TCanvas *c3 = new TCanvas("Ratio","ratio",10,10,510,510);
249     c3->cd(1)->SetLogy();
250     fHistPtPlus->Sumw2();
251     fHistPtMinus->Sumw2();
252     fHistRatio->Divide(fHistPtPlus,fHistPtMinus);
253     fHistRatio->SetName("fHistRatio");
254     fHistRatio->DrawCopy("E");
255 
256     TCanvas *c4 = new TCanvas("Vz","Vz",10,10,510,510);
257     c4->cd(1)->SetLogy();
258     fHistVzMinus->DrawCopy("E");
259     c4->cd(1)->SetLogy();
260     fHistVzPlus->DrawCopy("Esames");
261 
262     TCanvas *c5 = new TCanvas("AllMuonsPlusAddMinus","Pt",10,10,510,510);
263     c5->cd(1)->SetLogy();
264     fHistPtAll->DrawCopy("E");
265 
266 }
```

Part III

Appendix: Run Lists

155256	155257
155257	155387
155258	155388
155259	155389
155260	155390
155261	155391
155262	155392
155263	155393
155264	155394
155265	155395
155266	155396
155267	155397
155268	155398
155269	155399
155270	155400
155271	155401
155272	155402
155273	155403
155274	155404
155275	155405
155276	155406
155277	155407

Table 6.1: Run list of analyzed LHC11c data.

159606	158793	158285	157770
159602	158791	158271	157569
159599	158790	158263	157564
159595	158784	158258	157562
159593	158626	158252	157560
159582	158617	158201	157475
159581	158615	158200	157277
159580	158613	158196	157275
159577	158611	158194	157262
159539	158604	158192	157261
159538	158602	158189	157257
159536	158533	158179	157227
159535	158528	158177	157214
159532	158526	158176	157211
159379	158520	158175	157210
159378	158518	158173	157209
159356	158516	158171	157100
159319	158496	158139	157098
159318	158495	158137	157096
159286	158492	158136	157094
159285	158471	158132	157092
159283	158468	158124	157091
159259	158467	158118	157087
159254	158466	158115	157079
159090	158463	158112	157028
158879	158340	158111	157026
158878	158304	158086	157025
158877	158303	158084	156896
158876	158299	157975	156893
158875	158288	157848	156891
158868	158287	157819	156889

Table 6.2: Run list of analyzed LHC11d data.

162717
162718
162719
162720
162721
162722
162723
162724
162725
162726
162727
162728
162729
162730
162731
162732
162733
162734
162735
162736
162737
162738
162739
162740
162741
162742
162743
162744
162745
162746
162747
162748
162749

Table 6.3: Run list of analyzed LHC11e data.

Bibliography

[Aad12] G. Aad et al. Measurement of the transverse momentum distribution of W bosons in pp collisions pp at $\sqrt{s} = 7$ TeV with the ATLAS detector. *Phys. Rev. D*, 85:012005, Jan 2012.

[Aai12] R Aaij et al. Inclusive W and Z production in the forward region at $\sqrt{s} = 7$ TeV. *JHEP*, 1206:058, 2012.

[Aam10] K. Aamodt et al. Charged-Particle Multiplicity Density at Midrapidity in Central Pb-Pb Collisions at $\sqrt{s} = 2.76$ TeV. *PRL* 105, 252301, 2010.

[Abe12a] Abelev et al. Heavy flavour decay muon production at forward rapidity in proton–proton collisions at $\sqrt{s} = 7$ TeV. *Phys.Lett.*, B708:265–275, 2012.

[Abe12b] B. Abelev et al. Production of Muons from Heavy Flavor Decays at Forward Rapidity in pp and Pb-Pb Collisions at $\sqrt{s_{NN}}$ =2.76 TeV. *PRL*, 109, 2012.

[Adc05] K. Adcox et al. PHENIX Collaboration. *Nucl. Phys. A*, 757, 2005.

[Ale07] R. Alemany et al. Functional specification., lhc modes. LHC-OP-ES-0005 rev 1.0, 2007.

[Ale11] Alemany et al. Lhc –experiments handshake protocol over dip. LHC-OP-ES-0019 rev 4.0, 2011.

[Ali95] ALICE Collaboration. Alice Technical Design Report for A Large Ion Collider Experiment at CERN LHC. Technical report. Technical report, ALICE Collaboration. CERN/LHCC/95-97 LHCC/P3 (1995).

[Ali04] ALICE Collaboration. Alice trigger data-acquisition high-level trigger and control system: Technical design report. Technical report, ALICE Collaboration. CERN, 2004.

[ALIa] ALICE. Alice electronic logbook. `www.alice-logbook.cern.ch/logbook`.

[ALIb] ALICE. Alice run condition table. `http://alimonitor.cern.ch`.

[ALI00] ALICE. `http://aliceinfo.cern.ch/`, 2000.

[ALI07] ALICE. Alice detector control system shifter's tutorial. `http://www.alicedcs.web.cern.ch/`, 2007.

[ALI13] ALICE. Alice offline pages. `http://aliweb.cern.ch/Offline/`, 2013.

[Apo94] J. Apostolakis. Geant., detector description and simulation tool. `http://wwwasdoc.web.cern.ch/wwwasdoc/geant_html3/geantall.html`.

[Atl94] ATLAS: technical proposal for a general-purpose pp experiment at the Large Hadron Collider at CERN. Technical report, Geneva, 1994.

[Ast78] A. Astbury et al. A 4π solid angle detector for the sps used as a proton-antiproton collider at a centre of mass energy of 540 gev. ua1 proposal. Technical report, UA1 Collaboration., 1978. *CERN/SPSC/78-06, SPSC/P 92.*

[Bai01] R. Baier, Yuri L. Dokshitzer, Alfred H. Mueller, and D. Schiff. On the angular dependence of the radiative gluon spectrum. *Phys.Rev.*, C64:057902, 2001.

[Bai03] R. Bailey. Standard filling schemes for various lhc operation modes. *LHC-Project Note 323.*

[Ban78] M. Banner et al. *CERN/SPS/78–08 (1978)* and *CERN/SPS/78–54 (1978).*

[Ber12] J. Beringer et al. Review of Particle Physics, 2012. Review of Particle Properties. *Phy. Rev. D 86, 010001 (2012)* The 2010 edition of Review of Particle Physics is published for the Particle Data Group by IOP Publishing as article number 075021 in volume 37 of Journal of Physics G: Nuclear and Particle Physics. This edition should be cited as: J. Beringer et al. (Particle Data Group) 2012 Phy. Rev. D 86, 010001.

[Bet07] S. Bethke. Experimental tests of asymptotic freedom. *Pog. Part. Nucl. Phys.*, 58:351–386, 2007.

[Bos12] F. Bossù, M. Gagliardi, M. Marchisone, and ALICE Collaboration. Performance of the RPC-based ALICE muon trigger system at the LHC. *ArXiv e-prints*, November 2012.

[Bru95] R. Brun. Root. `http://root.cern.ch/`,1995.

[Bry08] P. Bryant and L. Evans. The CERN Large Hadron Collider: Accelerators and experiments. *Jinst.* 2008

[Cha11] Serguei Chatrchyan et al. Measurement of the lepton charge asymmetry in inclusive W production in pp collisions at $\sqrt{s} = 7$ TeV. *JHEP*, 1104:050, 2011.

[Cam10] T. Camporesi. The operation of the lhc detectors. *LPCC student lectures*, 2010.

[Car04] P Giubellino. A Morsch. G Paic. J-P Revol. K Safarik. Y Schutz F. Carminati., P Foka. and U A Wiedemann. ALICE: Physics Performance Report, Volume I. ALICE Collaboration. *J. Phys. G: Nucl. Part. Phys.*,30,1517-1763,2004.

[Cho74] A. Chodos, R. L. Jaffe, K. Johnson, C. B. Thorn, and V. F. Weisskopf. New extended model of hadrons. *Phys. Rev. D*, 9:3471–3495, Jun 1974.

[Cte96] CTEQ collaboration. The Coordinated Theoretical-Experimental Project on QCD. Online pdf plot generator. `http://hepdata.cedar.ac.uk/pdf/pdf3.html`. `http://users.phys.psu.edu/~cteq/`,1996

[Cms94] The CMS Collaboration. The Compact Muon Solenoid Techinical Proposal Technical report. CERN, 1994.

[Cph00] CPH Theory. reative particles of higgs theory. `http://cph-theory.persiangig.com/2255-daynoend.htm`.

[Cro05] Philippe Crochet. Quarkonia and heavy flavors at the LHC. *Eur.Phys.J.*, C43:437–443, 2005.

[Dai03] A. Dainese. *Charm production and in-medium QCD energy loss in nucleus–nucleus collisions with ALICE. A performance study.* PhD Thesis (universita degli studi di padova), 2003.

[Das13] I. Das. Muon tracking. `https://twiki.cern.ch/twiki/bin/viewauth/ALICE/MuonTracking`.

[Daw98] S. Dawson. Introduction to electroweak symmetry breaking. *arXiv:hep-ph/9901280v1*, 1998.

[DuT13] P. Du Toit. Analysis of $W^{\pm}$ boson production via the semi-muonic channel in pp & PbPb with the ALICE Muon Spectrometer at LHC energies and the effect of alignment. Master's thesis, University of Pretoria, 2013.

[dVa07] Z. C. del Valle. *Performance of the ALICE muon spectrometer. Weak boson production and measurement in heavy-ion collisions at LHC.* PhD thesis, *É*cole des Mines de Nantes, Nantes, France, 2007.

[Esk01] K.J. Eskola, V.J. Kolhinen, and R. Vogt. Obtaining the nuclear gluon distribution from heavy quark decays to lepton pairs in pA collisions. *Nucl.Phys.*, A696:729–746, 2001.

[Eva05] D. Evans et al. The ALICE central trigger processor. CERN 2005-038, 2005

[Fer05] A. Fasso A. Ferrari, P. R. Sala and J. Ranft. Fluka: a multi-particle transport code., 2005. CERN-2005-010.

[Fer08] M. Ferro-Luzzi. Lhc bunch filling schemes for commissioning and initial luminosity optimization., 2008. LHC Project Note 415.

[Fri04] S. Frixione and M.L. Mangano. How accurately can we measure the W cross section? *JHEP*, 0405:056, 2004.

[Fon13] Fixed order plus next-to-leading logarithms. `http://www.lpthe.jussieu.fr/~cacciari/fonll/fonllform.html`,2013.

[Gre10] B. Müller W. Greiner. *Gauge Theory of Weak Interactions.* 3rd Edition.Springer-Verlag Berlin Heidelberg New York, 2010.

[Gla70] R.J. Glauber and G. Matthiae. High-energy scattering of protons by nuclei. *Nucl.Phys.*, B21:135–157, 1970.

[Gre08] O.W. Greenberg. The Parton model. *arXiv:0805.2588v3[hep-ph]*,2008.

[Gro73] David J. Gross and Frank Wilczek. Ultraviolet behavior of non-abelian gauge theories. *Phys. Rev. Lett.*, 30:1343–1346, Jun 1973.

[Gui04] A.Sobol and J. P. Guillaud. Simulation of diffractive and non-diffractive processes at the lhc energy with pythia and phojet mc event generators, 2004. LAPP-EXP 2004-06.

[Hal86] A. D. Martin F. Halzen. *Quarks and Leptones: An Introductory Course in Modern Particle Physics.* Wiley; 1st edition., 1986.

[Han01] Simon Hands. The Phase diagram of QCD. *Contemp.Phys.*, 42:209–225, 2001.

[Hol06] Wolfgang Hollik. Electroweak theory. In *Journal of Physics: Conference Series*, volume 53, page 7. IOP Publishing, 2006.

[Hri00] P. Hristov. Aliroot primer. `http://aliceinfo.cern.ch/Offline/AliRoot/Manual.html`, Version 0.00(Rev.22).

[Kak93] M. Kaku. *Quantum Field Theory. Modern Introduction.* Oxford University Press, 1993.

[Kar00] F. Karsch, E. Laermann, and A. Peikert. The Pressure in two flavor, (2+1)-flavor and three flavor QCD. *Phys.Lett.*, B478:447–455, 2000.

[Lai00] H.L. Lai et al. Global QCD analysis of parton structure of the nucleon: CTEQ5 parton distributions. *Eur.Phys.J.*, C12:375–392, 2000.

[Lhc98] *LHCb : Technical Proposal.* Tech. Proposal. CERN, Geneva, 1998.

[Lpca] Filling schemes. `http://lpc.web.cern.ch/lpc/fillingschemes.htm`.

[Lpcb] Lhc complex. `http://te-epc-lpc.web.cern.ch/te-epc-lpc/machines/lhc/general.stm`.

[Lpcc] The lhc luminosity charts. `http://lpcc.web.cern.ch/lpcc/index.php?page=luminosity_charts`.

[Mal98] Juan Martin Maldacena. The Large N limit of superconformal field theories and supergravity. *Adv.Theor.Math.Phys.*, 2:231–252, 1998.

[Mar00] Alan D. Martin, R.G. Roberts, W. James Stirling, and R.S. Thorne. Parton distributions and the LHC: W and Z production. *Eur.Phys.J.*, C14:133–145, 2000.

[Mar06] B. R. Martin. *Nuclear and Particle Physics.* John Wiley & Sons Ltd., 2006.

[Mat86] T Matsui and Helmut Satz. J-psi-suppression by quark gluon plasma formation. *PHYSICS LETTERS B*, 178(4):416–422, 1986.

[Mat10] N. Matagne. Cold nuclear matter effects on quarkonium production at rhic and the lhc. First ReteQuarkonii Workshop, 2010.

[Moo05] Guy D. Moore and Derek Teaney. How much do heavy quarks thermalize in a heavy ion collision? *Phys.Rev.*, C71:064904, 2005.

[Mre09] S. Mrenna. Monte carlo & event generators. school presentation. CTEQSS09, 2009.

[MuoQA] Muon quality assurance. `https://twiki.cern.ch/twiki/bin/viewauth/ALICE/MuonppQA2011`., `https://twiki.cern.ch/twiki/bin/viewauth/ALICE/QAForTheSelectionOfGoodPhysicsRunsForMuonPhysics`.

[Nav10] Sparsh Navin. Diffraction in Pythia. *arXiv:1005.3894v1 [hep-ph]*, 2010.

[Oid12] H. Oide. *Measurement of longitudinal spin asymmetry in production of muons from W/Z boson decays in polarized p+p collisions at* $\sqrt{s_{NN}}$ *= 500 GeV with the PHENIX detector at RHIC.* PhD thesis.

[Pan84] C Rubbia G. Panduri. *Nucl. Phys.*, page 117, 1984.

[Pil13] P. Pillot. Private conservation.

[Pil12] P. Pillot. Muon tracking performances. ALICE MUON Workshop, `www.itlabs.ac.za/events/`.

[Qui02] Chris Quigg. The Electroweak theory. pages 3–67, 2002.

[Raj06] A. A. Rajabi. Determining the relation between effective coupling constant and quark mass in the parton model using massive nucleonic quarks in hypercentral potential. *Indian Journal of Pure & Applied Physics.*, pages 512–518, 2006.

[Ric09] M. Richter. *Development and Integration of on-line Data Analysis for the ALICE Experiment.* Phd thesis, 2009. CERN-THESIS-2009-189.

[Sai03] P. Saiz et al. AliEn - ALICE environment on the GRID. *Nucl.Instrum.Meth.*, A502:437–440, 2003.

[Sal06] W. Salter. LHC data interchange protocol (dip) definition, 2006. EDMS Reference: 457113.

[Sin00] C. P. Singh. Quark gluon plasma. *Pramana-J. Phys.*, Vol.54, No. 4, 2000.

[Sjo06] Torbjorn Sjostrand, Stephen Mrenna, and Peter Z. Skands. PYTHIA 6.4 Physics and Manual. *JHEP*, 0605:026, 2006.

[Ska10] Peter Zeiler Skands. Tuning Monte Carlo Generators: The Perugia Tunes. *Phys.Rev.*, D82:074018, 2010.

[Smi00] Tim Smith. Models of networked analysis at regional centres for lhc experiments. `http://www.cern.ch/MONARC/`, 2000.

[Sto08] Diego Stocco. *Development of the ALICE Muon Spectrometer: preparation for data taking and heavy flavor measurement.* PhD thesis, Turin U., 2008. Presented on Aug 2008.

[Tap08] J Daniel Tapia Takaki and O Villalobos Baillie. *Physics performance studies for the ALICE experiment at the CERN LHC.* PhD thesis, Birmingham U., Birmingham, UK, 2008. Presented on 27 Jan 2008.

[Tri05a] Alessandro Tricoli, Amanda M. Cooper-Sarkar, and Claire Gwenlan. Uncertainties on W and Z production at the LHC. 2005.

[Tri05b] Alessandro Tricoli, Amanda M. Cooper-Sarkar, and Claire Gwenlan. Uncertainties on W and Z production at the LHC. 2005.

[Won05] C.-Y. Wong. Heavy quarkonia in quark-gluon plasma. *PRC*, 72(3):034906, sep 2005.

[Wu+57] C. S. Wu, E. Ambler, R. W. Hayward, D. D. Hoppes, and R. P. Hudson. Experimental test of parity conservation in beta decay. *Phys. Rev.*, 105:1413–1415, Feb 1957.

[Zha12] X Zhang. *Study of Heavy Flavours from Muons Measured with the ALICE Detector in Proton-Proton and Heavy-Ion Collisions at the CERN-LHC.* PhD thesis, Clermont-Ferrand U., 2012. presented 23 May 2012.